



THE HONG KONG
POLYTECHNIC UNIVERSITY

香港理工大學

Pao Yue-kong Library

包玉剛圖書館

Copyright Undertaking

This thesis is protected by copyright, with all rights reserved.

By reading and using the thesis, the reader understands and agrees to the following terms:

1. The reader will abide by the rules and legal ordinances governing copyright regarding the use of the thesis.
2. The reader will use the thesis for the purpose of research or private study only and not for distribution or further reproduction or any other purpose.
3. The reader agrees to indemnify and hold the University harmless from and against any loss, damage, cost, liability or expenses arising from copyright infringement or unauthorized usage.

IMPORTANT

If you have reasons to believe that any materials in this thesis are deemed not suitable to be distributed in this form, or a copyright owner having difficulty with the material being included in our database, please contact lbsys@polyu.edu.hk providing details. The Library will look into your claim and consider taking remedial action upon receipt of the written requests.

**GRAPHENE BASED ELECTRICAL BIOSENSORS
FOR THE DETECTION OF BIOMOLECULES**

CHAN CHUN YU

Ph.D

The Hong Kong Polytechnic University

2016

The Hong Kong Polytechnic University
Interdisciplinary Division of Biomedical Engineering

**Graphene Based Electrical Biosensors for the
Detection of Biomolecules**

CHAN Chun Yu

A thesis submitted in partial fulfillment of the requirements for
the degree of Doctor of Philosophy

September 2015

Certificate of Originality

I hereby declare that this thesis is my own work and that, to the best of my knowledge and belief, it reproduces no material previously published or written, nor material that has been accepted for the award of any other degree or diploma, except where due acknowledgement has been made in the text.

_____ (Signed)

Mr. CHAN Chun Yu (Name of student)

Abstract

Detection of biomolecules provides analytical information about the component of food, safety of drinking water, quality of environment or even diagnostic information about a patient. It is of great importance to develop biosensors with good reliability, sensitivity, LOD and simple in operation. Through the years of development in nano-materials, most of them have proved themselves to be a great candidate in different areas of biosensing, for example, gold nano-particles in colorimetric biosensing, quantum dots in fluoresce biosensing, silica nano-wire and carbon nano-tube in FET biosensing, etc. Among the list of discovered nano-materials, graphene was only being studied empirically for approximately ten years and its miraculous properties amused scientists and opened a new era of the study in two-dimensional material. In this study, graphene was used as transducer in field-effect transistor biosensor and electrochemical biosensor for detection of various targets.

In the fist project, reduced graphene oxide was fabricated into field-effect transistor and functionalized with long capture probe for detection of H5N1 avian influenza virus gene detection. The long capture probe proposed in this study contains two

sections, one of the recognized and hybridize with target DNA and the other section remained single stranded to π - π stack with graphene. When compared with the conventional DNA immobilization approach on graphene surface (short capture probe and linker involved covalent immobilization), the proposed long capture probe approach was found to be the most sensitive one. It is hypothesized that long capture probe has a better affinity to graphene after DNA hybridization and it brought target DNA closer to graphene surface, which no linker was required.

In the second project, long capture probe similar to the first project was applied in a CVD graphene-based biosensor. Here, a secondary reporter probe with gold nano-particles conjugated with target complementary oligonucleotide was applied. The reporter probe enhanced the sensitivity of the biosensor and the detection limit was as low as 64 fM. More importantly, it has the ability to differentiate single-base mismatch from fully complementary sequence which suggested an excellent specificity.

In the final chapter, a reduced graphene oxide-based electrochemical biosensor was developed for sensing botulinum neurotoxin type A. An artificially synthesized recognition probe (SNAP-25-GFP) with cleavage site for botulinum neurotoxin type A

was immobilized on the surface of reduced graphene oxide. Initially, the electrode surface was covered making it inaccessible to the redox probe in the standard buffer.

When botulinum neurotoxin type A presented in the analyte, the probe on the surface of reduced graphene oxide was removed exposing the electrode, thus recovering the electrochemical signal. This sensing system demonstrated a very good limit of detection against botulinum neurotoxin A with excellent specificity, which only fresh and active botulinum neurotoxin A can be detected. More importantly, this electrochemical-sensing platform was proved to be functioning when botulinum neurotoxin A dispersed in milk, mimicking a real-life sample. The low interference suggested its potential to be applied as an on-site toxin screening platform.

List of Publications

Journal papers:

Chan, C.Y., Li, W.C., Feng, Y., Yang, M., A CVD-grown graphene based field-effect transistor biosensor with gold nanoparticle signal amplification for detection of avian influenza virus H7 subtype (**Manuscript in preparation**)

Chan, C.Y., Feng, Y., Yang, M., Effect of different probe DNA immobilization methods on a reduced graphene oxide (rGO) based transistor (**Manuscript in preparation**)

Chan, C.Y., Tsang, M.K., Hao, J., Yang, M., Energy Transfer from Graphene Quantum Dots to Luminescence Lanthanide Tb³⁺ beyond the Formation of non-Fluorescence Aggregates (**Manuscript in preparation**)

Chan, C.Y., Guo, J., Sun, C., Tsang, M.K., Tian, F., Hao, J., Chen S., Yang, M., 2015. Sens. Actuator B-Chem. 220, 131–137.

Shi, J., **Chan, C.Y.**, Pang, Y., Ye, W., Tian, F., Lyu, J., Zhang, Y., Yang, M., 2015. Biosens. Bioelectron. 67, 595-600.

Shi, J., Guo, J., Bai, G., **Chan, C.Y.**, Liu, X., Ye, W., Hao, J., Chen, S., Yang, M., 2014. Biosens. Bioelectron. 65C, 238-244.

Ye, W., Shi. J., **Chan, C.Y.**, Zhang, Y., Yang, M., 2014. Sens. Actuator B-Chem. 193, 877-882.

Xu, B., Ye, W., Zhang, Y., Shi, J., **Chan, C.Y.**, Yao, X., Yang, M., 2014. Biosens. Bioelectron. 53, 187-192.

Conference paper:

Ye, W., Shi. J., **Chan, C.Y.**, Xiao, L.D., Yang, M., Transducers 2013, Barcelona, Spain, 16-20 June 2013.

Acknowledgements

I would like to take this chance to delivery my gratitude to my supervisor Dr. Mo Yang. Dr. Mo Yang granted me the opportunity to be a research student under his guidance with sincere support. Secondly, I greatly thank Dr. Feng Yen for giving me the chance of using his laboratory equipment otherwise I could never finish this study. Also, I would also like to thank my collaborators Mr. Jiubiao Guo from Applied Biology & Chemical Technology and Mr. Ming Kiu Tsang from Applied Physics for working together all along these years. Besides, there are many important people who helped my experiments, including Dr. Wei Lu and Dr. Hardy Liu, from PolyU Material Research Center, Ms. Winnie Wu from Surface Analysis & Material Characterization Laboratory from Hong Kong Baptist University. Without them, my thesis could never be finished.

Table of Contents

Certificate of Originality	i
Abstract.....	ii
List of Publications	v
Acknowledgements	vi
Table of Contents	vii
List of Figures	xiii
List of Abbreviations.....	xxiii
Chapter 1 Background and Introduction	1
1.1. Graphene.....	1
1.1.1. Discovery	1
1.1.2. Physical properties	3
1.1.3. Graphene counterparts	5
1.1.4. Preparation of graphene	6
1.2. Graphene in electrical biosensors	13
1.2.1. Fundamentals of biosensing	13
1.2.2. Electrochemical biosensors	16
1.2.3. Field-effect transistor (FET) biosensors	26

1.3. Objectives of study	44
 Chapter 2 Reduced Graphene Oxide Transistor with Extended DNA Capture	
Probe for DNA Detection	47
2.1. Introduction	47
2.2. Research methodology	53
2.2.1. Materials	53
2.2.2. Preparation of rGO transistor.....	54
2.2.3. Immobilization of capture probe on rGO channel	55
2.2.4. Hybridization experiment	56
2.2.5. Preparation of rGO transistor.....	57
2.2.6. Instrumentations	58
2.3. Results and discussion.....	59
2.3.1. AFM characterization of the morphology of rGO film	59
2.3.2. Reduction of rGO.....	60
2.3.3. Fluorescence study of different probe stability on rGO	66
2.3.4. Functionalizing rGO FET with long capture probe	71
2.3.5. rGO FET with long capture probe for target detection	74
2.3.6. Real-time detection of cDNA target using long capture probe	77
2.3.7. Comparing rGO FET biosensor performance with different probe immobilization	

strategies	83
2.4. Summary	87
Chapter 3 Chemical Vapor Deposition Grown Graphene DNA Field-Effect Transistor Biosensor with Gold Nanoparticles Signal Amplification	89
3.1. Introduction	89
3.2. Research methodology	92
3.2.1. Materials	92
3.2.2. CVD graphene transistor fabrication	94
3.2.3. Immobilization of capture probes on graphene	95
3.2.4. Conjugation of AuNPs with reporter probes for signal enhancement	96
3.2.5. Electrical measurement	97
3.2.6. Instrumentation	97
3.3. Results and discussion.....	98
3.3.1. AFM image of CVD graphene and TEM images of AuNPs.....	98
3.3.2. Transfer curve of CVD graphene transistor.....	100
3.3.3. Stability of CVD graphene transistor	102
3.3.4. Functionalization and Detection	106
3.3.5. Real-time response.....	111
3.3.6. Signal amplification by reporter probe-AuNPs	113

3.3.7. Effect of the size of reporter probe-AuNPs	116
3.3.8. Specificity of the graphene bioFET	120
3.4. Summary	122
Chapter 4 A rGO-Modified Gold Electrode for Ultrasensitive Electrochemical	
Detection of Botulinum Neurotoxin	123
4.1. Introduction	123
4.2. Research methodology	127
4.2.1. Materials	127
4.2.2. Reduction of rGO.....	127
4.2.3. Preparation of rGO/Au electrode	128
4.2.4. Covalently functionalization of rGO/Au electrode with SNAP-25-GFP	129
4.2.5. BoNT-LcA enzymatic activity biosensing.....	129
4.2.6. Electrochemical measurement	130
4.2.7. Instrumentation	131
4.3. Results and discussion.....	131
4.3.1. Morphology of rGO	132
4.3.2. Characterization of hydrazine reduction	133
4.3.3. Characterization of SNAP-25-GFP immobilization.....	138
4.3.4. C.V. electrochemical behavior of Au/rGO working electrode at different scanning	

rate	140
4.3.5. C.V. and E.I.S. characterization of working electrode modification	142
4.3.6. LcA detection using differential pulse voltammetry (DPV)	147
4.3.7. Limit of detection (LOD) against LcA	152
4.3.8. Stability of the electrochemical LcA biosensor	156
4.3.9. Interference effect of milk sample	159
4.4. Summary	162
Chapter 5 Discussion	164
5.1. Reduced graphene oxide transistor with extended DNA capture probe for DNA Detection	164
5.1.1. Affinity of ssDNA-graphene and ds-DNA-graphene	164
5.1.2. Length of the single-stranded sequence in the long capture probe	166
5.2. Chemical vapor deposition grown graphene DNA field-effect transistor biosensor with gold nanoparticles signal amplification.....	168
5.2.1. Size of AuNPs on the effect of signal amplification	169
5.2.2. FET sensing beyond Debye's length	170
5.2.3. Choosing AuNPs as reporter probe carrier	170
5.3. A rGO-modified gold electrode for ultrasensitive electrochemical detection of botulinum neurotoxin	172

5.3.1. Detection mechanism	172
5.3.2. Using SNAP-25-GFP instead of SNAP-25 as detection probe.....	174
5.3.3. Compare our proposed electrochemical BoNT/A biosensor with gold standard mouse bioassay.....	175
Chapter 6 Conclusion	177
Chapter 7 Future Works.....	179
References	182

List of Figures

Figure 1.1.1. Graphene is the basic building block of different carbon-based materials.

Graphene (top) can be wrapped into zero dimension buckyballs (bottom left), rolled into one dimension carbon nanotubes (bottom middle) and stacked into three-dimensional graphite (bottom right) (Adopted from Geim et al., 2007).....2

Figure 1.1.4. Overview on the existing methods for mass-producing graphene (Adopted from Novoselov et al., 2012).....7

Figure 1.1.4.1. Example of a typical solution phase exfoliation process. Graphite dissociate into single-layered graphene with the aid of surfactants, intercalators and ultrasound (Adopted from Ciesielski et al., 2014).....10

Figure 1.1.4.2. (a) Commercially available 7 cm X 7 cm CVD graphene on a 4 inch SiO₂ wafer (ACS Material). **(b)** 35 inches graphene/PET film transferred by thermal release tape as transparent electrode (Adopted from Seo et al., 2013; Bae et al., 2010).....13

Figure 1.2.1. Schematic illustration of a biosensing process. Sample is introduced into a biosensor with a recognition element and a transducer. Recognition element interacts specifically with the detection target while the transducer translates the recognition event into physical signals.....15

Figure 1.2.2. Schematic of the first commercialized glucose electrochemical

biosensor (Adopted from Wang et al., 2001).....17

Figure 1.2.2.1. Graphical illustration of the edge and basal plane of a graphene flake.

(Adopted from Brownson et al., 2012).....20

Figure 1.2.2.2. (a) Transmission electron microscopy (TEM) image of MGNFs

fabricated by microwave plasma enhanced CVD. **(b)** DPV profile of MGNFs

electrode with 1 mM AA, 0.1 mM UA and various concentrations of DA (Shang et al.,

2008).....22

Figure 1.2.2.3. (a) TiO₂-graphene composite and **(b)** AuNPs decorated graphene

engineered for electrochemical biosensing glucose (Adopted from Shang et al., 2010;

Jang et al., 2012).....23

Figure 1.2.2.4. (a) An impedimetric biosensor with the aid of redox probe for

detection of DNA hybridization event. Hybridization of target DNA with probe DNA

reduced Rct of graphene electrode (Adopted from Bonanni et al., 2011). **(b)** Extended

capturing probe retained target DNA on the surface of graphene modified electrode.

Subsequent AuNPs tags were introduced with silver enhancement and electrochemical

signal of silver oxidation was read by DPV (Adopted from Lin et al.,

2011).....26

Figure 1.2.3. (a) Configuration of a typical FET biosensor. Charged biomolecules

capture to the proximity of the semiconducting channel by recognition element and

gate the semiconductor. **(b)** Transfer curve (blue) of a typical p-type semiconductor.

Binding of negatively charged target biomolecules shift the transfer curve to positive side (red). Change of semiconductor electrical behavior can be interpreted by either monitoring IDS at a fixed VG or study the shift of threshold voltage by scanning transfer curve.....30

Figure 1.2.3.2. Schematic of Graphene FET being used in **(a)** pH sensing with solution gate (Adopted from Ang et al., 2008) **(b)** Pb²⁺ sensing using DNAzyme as recognition element (Adopted from Wen et al., 2013) and **(c)** Hg²⁺ sensing functionalized with Hg²⁺ specific aptamer (Adopted from An et al., 2013).....34

Figure 1.2.3.3. Schematic of **(a)** graphene-amine (GA) FET biosensor which was able to detect negatively charged bacteria and **(b)** DNA, depending on the functionalization approach that was carried out (Adopted from Mohanty et al., 2008). **(c)** AuNPs decorated CVD graphene for DNA detection (Adopted from Dong et al., 2010). **(d)** Graphene FET sensor using PNA as a recognition element (Adopted from Cai et al., 2014).....38

Figure 1.2.3.4. Schematic of **(a)** AuNPs decorated vertically-oriented graphene for sensing IgG (Adopted from Mao et al., 2010) and **(b)** GO coated SiO₂ nanoparticles, which were subsequently deposited on a substrate. **(c)** Scanning electron microscopy (SEM) image of arrays of GO-NPs FET channels formed on a substrate using

photolithography technique (Adopted from Myung et al., 2011).....42

Figure 1.2.3.5. Schematic of (a) PC12 directly cultured on poly-L-lysine-coated rGO FET channel. K^+ induced release of catecholamine containing vesicles induced gating of FET conductivity and (b) displayed peaks on real-time conductance measurement (Adopted from He et al., 2010). (c) Electrogenic embryonic chicken cardiomyocytes cultured on graphene FET and (d) action potential generated from cardiomyocytes gated graphene FET conductance under different biased V_G (Adopted from Cohen-Karni et al., 2010).....44

Figure 2.1. Schematic illustration of long capture probe suggested in this project. Long capture probe composed with two sections: a.) complementary sequence recognize and capture target DNA and b.) extended DNA sequence retains π - π stacking with graphene after target hybridization. Capture of target DNA on rGO surface decreased the conductance of rGO while conductance of rGO channel was monitored in real-time after analyte introduction.....53

Figure 2.2.2. Illustration of rGO FET channel fabrication process.....56

Figure 2.2.3.1. Illustration of long capture probe and short capture probe immobilization via π - π stacking.....56

Figure 2.2.3.2. Illustration of amine-modified short capture probe immobilization process.....57

Figure 2.2.5. Optical image of an **(a)** as fabricated rGO transistor and **(b)** the rGO FET channel incorporated with a PDMS reservoir. **(c)** Illustration of setup in electrical measurement of rGO bioFET..... 59

Figure 2.3.1. **(a)** AFM image of a rGO film and **(b)** enlarged portion of the AFM image **(c)** height profile of rGO film on Si/SiO₂ substrate.....61

Figure. 2.3.2.1. **(a)** Raman spectroscopy of GO film and rGO film after hydrazine reduction and **(b)** time lapsed study of I_D/I_G after different hydrazine reduction time..... 64

Figure. 2.3.2.2. **(a)** XPS wide scan of GO and rGO after hydrazine vapor reduction. **(b)** C 1s scan of GO and **(c)** rGO.....66

Figure 2.3.3 Fluorescence signals of removed samples in the washing environment for four cases of **(a)** fluorescence-labeled short capture probe + cDNA, **(b)** fluorescence-labeled short capture probe + non-cDNA, **(c)** fluorescence-labeled long capture probe + cDNA, and **(d)** fluorescence-labeled long capture probe + non-cDNA. Here, the fluorescence signal obtained from fluorescence-labeled short capture probe + cDNA was used as reference..... 71

Figure 2.3.4. **(a)** I-V curves of bare rGO and rGO functionalized with long capture probe. **(b)** Real-time current measurement of rGO FET when different concentrations of long capture probe (10 nM, 50 nM, 100 nM and 1 μM) were injected into PDMS

reservoir ($V_{DS} = 0.4 \text{ V}$).....	75
Figure 2.3.5. I-V curves of long capture probe functionalized rGO, (a) after exposed to cDNA and (b) after exposure to non-cDNA.....	78
Figure 2.3.6. (a) Real-time measurement of conductance change of rGO FET biosensor functionalized with long capture probe upon exposure to various concentration (10 pM, 100 pM, 1 nM, 10 nM, 100 nM and 1 μM) of cDNA and non-cDNA and (b) sensing signal ($\Delta G/G_0$) plot against concentration of DNA. (c) $\Delta G/G_0$ plot against the logarithmic concentration of cDNA. Noise level was established by introducing blank buffer solution to the rGO FET channel. Statistical data was obtained from three individual devices.....	83
Figure 2.3.7. Histogram comparing rGO FET biosensor response with different probe immobilization methods when exposed to different concentration of cDNA. Probe immobilization methods investigated included covalent immobilization amine-modified short capture probe with PA, π - π stacking with short capture probe or long capture probe.....	88
Figure 3.1.1. Schematic illustration of the proposed graphene bioFET sensing mechanism (a) capture probe captures target H7 DNA and (b) reporter probe-AuNPs amplifies sensing signal by enhancing charge density on the proximity of graphene.....	93

Figure 3.2.4. Illustration of the configuration of CVD graphene-based bioFET during electrical measurement.....98

Figure 3.3.1. (a) AFM image of CVD-grown graphene transferred onto a Si/SiO₂ wafer; (b) TEM image of AuNPs in 15 nm and (c) 30 nm conjugated with reporter probes for signal amplification.....101

Figure 3.3.2. Transfer curve measured from a bare CVD graphene transistor. V_G was applied through a Pt electrode via solution gate.103

Figure 3.3.3. (a) Transfer curves measured from a bare CVD graphene transistor by sweeping for seven times. (b) V_{CNP} of forward sweep and backward sweep during different number of transfer curve sweeping.....106

Figure 3.3.4. (a) GFET transfer curves of bare graphene, capture probes functionalized graphene, after incubation with 1 nM H7 target and (b) 1 nM non-target DNA. (c) Raman spectrum of bare graphene and capture probes functionalized graphene.....111

Figure 3.3.5. Real-time response of graphene bioFET biosensors exposed to 1 pM, 50 pM and 100 pM H7 target.....115

Figure. 3.3.6. (a) Transfer curves of the graphene FET device with capture probes immobilized, exposed to 1 pM H7 target and 15 nm reporter probe-AuNPs. Inset: magnification of the region near V_{CNP} . (b) XPS spectra recorded before and after

reporter probe-AuNPs signal amplification. 118

Figure 3.3.7. Shift of VCNP of graphene bioFET after incubation with various H7 target concentrations, (a) without and with (b) 15 nm or (c) 30 nm reporter probe-AuNPs signal amplification..... 122

Figure 3.3.8. ΔV_{CNP} of CVD graphene bioFET with reporter probe-AuNPs signal amplification after exposing to blank buffer, double-base mismatch target, single-base mismatch target and fully complementary H7 target..... 124

Figure 4.1.1. Detection mechanism of the rGO based biosensors. (a) SNAP-25-GFP immobilized on rGO blocked the electrode surface preventing electron-transfer. (b) LcA cleaved the SNAP-25-GFP, exposing rGO electrode surface thus recovered DPV signal (Adopted from Chan et al., 2015)..... 129

Figure 4.3.1. TEM images of rGO nanoflakes under different magnification (Adopted from Chan et al., 2015)..... 135

Figure 4.3.2. (a) UV-Vis spectrum, (b) Raman spectrum and (c) XPS spectrum of GO and rGO (Adopted from Chan et al., 2015)..... 140

Figure 4.3.3. (a) XPS spectrum and (b) FTIR spectrum of rGO and rGO/PA/SNAP-25-GFP (Adopted from Chan et al., 2015)..... 143

Figure 4.3.4. (a) Cyclic voltammogram of Au/rGO electrode scanning from -0.2 V to 0.6 V with various scanning rate (10 mV/s, 20 mV/s, 40 mV/s, 60 mV/s, 80 mV/s, 100

mV/s) in pH 7.4 1X PBS supplemented with 5 mM $[\text{Fe}(\text{CN})_6]^{3-/4-}$ and 100 mM KCl. (b)

Anodic (I_{pa}) and cathodic current (I_{pc}) plot against the square root of scanning rate

(Adopted from Chan et al., 2015).....144

Figure 4.3.5. (a) Cyclic voltammograms and (b) EIS Nyquist plot with Au, Au/rGO, Au/rGO/PA and Au/rGO/PA/SNAP-25-GFP modified electrodes. Measurement was performed in pH 7.4 1X PBS supplemented with 5 mM $[\text{Fe}(\text{CN})_6]^{3-/4-}$ and 100 mM KCl. Inset: magnified Nyquist plot (Adopted from Chan et al., 2015).....150

Figure 4.3.6. (a) Differential pulse voltammograms of Au/rGO/PA/SNAP-25-GFP treated with blank buffer, LcB (1 ng/mL), heat-treated LcA (1 ng/mL) and fresh LcA (1 ng/mL). DPV measurements were performed in 1X PBS supplemented with 5 mM $[\text{Fe}(\text{CN})_6]^{3-/4-}$ (1:1) and 100 mM KCl (b) Histogram showing the DPV peak current change (ΔI) before and after different sample incubation (n=3) (Adopted from Chan et al., 2015).....155

Figure 4.3.7. (a) Calibration curve for the change in DPV current ($\Delta I\%$) at different LcA concentration. (b) calibration curve plot for $\Delta I\%$ vs. log LcA concentration (in pg/mL). Noise level was established by incubating with blank buffer and calculated by its mean + 3 SD (n = 5).....159

Figure 4.3.8. (a) DPV curves of functionalized working electrode measured after incubated with blank buffer. The same working electrode was repeated with the same

experiment for seven times. **(b)** Relative DPV peak current at different measurements.

All DPV peak current was standardized by the first measurement..162

Figure 4.3.9. Comparison of our electrochemical biosensor response against various concentration of LcA in pure buffer or skimmed milk samples (Adopted from Chan et al., 2015).....166

Figure 5.1.1. The trajectories of **(a)** ssDNA and **(b)** dsDNA absorbing on graphene (Adopted from Zeng et al., 2007).170

List of Abbreviations

AA	Ascorbic acid
AC	Alternative current
AFM	Atomic force microscopy
APTES	3-aminopropyltriethoxysilane
AuNPs	Gold nanoparticles
BioFET	Biological field-effect transistor
BoNT	Botulinum neurotoxins
BoNT/A	BoNT serotype A
cDNA	Complementary DNA
CV	Cyclic voltammetry
CVD	Chemical vapor deposition
DA	Dopamine
dc-PECVD	dc plasma-enhanced chemical vapor deposition
DI water	Deionized water
DMF	N,N-Dimethylformamide
DNA	Deoxyribonucleic acid
DPV	Differential pulse voltammetry
dsDNA	Double-stranded DNA

DTT	DL-dithiothreitol
EDC	N-(3-Dimethylaminopropyl)-N'-ethylcarbodiimide hydrochloride
EGFR	Epidermal growth factor receptor
EIS	Electrochemical impedance spectroscopy
FET	Field-effect transistor
FTIR	Fourier transform infrared spectroscopy
G	Real-time measured conductance
GA	Graphene-amine
GCE	Glassy carbon electrode
GFET	Graphene FET
GO	Graphene oxide
G_0	Original conductance
GOx	Glucose oxidase
GQD	Graphene quantum dots
H_2O_2	Hydrogen peroxide
HATU	1-[Bis(dimethylamino)methylene]-1H-1,2,3-triazolo[4,5-b] pyridinium 3-oxid hexafluorophosphate
HER2	Human Epidermal growth factor Receptor 2
I_{DS}	Source-drain current

IgE	Immunoglobulin E
IGG	Immunoglobulin G
ISFET	Ion-sensitive FET
KCl	Potassium Chloride
LcA	Light chain of BoNT/A
LcB	Light chain of BoNT/B
LOD	Limit of detection
MGNFs	Multilayer graphene nanoflake films
NaCl	Sodium chloride
OLED	Organic light-emitting diode
PA	Pyrenebutyric acid
PB	Phosphate buffer
PBS	Phosphate buffered saline
PC12	Rat pheochromocytoma
PDMS	Polydimethylsiloxane
PGA	Plasma modified graphene-amine
PMMA	Poly-methyl methacrylate
PNA	Peptide nucleic acid
PtNPs	Platinum nanoparticles

qRT-PCR	Reverse-transcriptase polymerase chain reaction
R_{ct}	Charge transfer resistance
rGO	Reduced graphene oxide
SDS	Sodium dodecyl sulfate
SEM	Scanning electron microscopy
SNAP-25	Synaptosomal-associated protein 25
SNP	Single-base nucleotide polymorphism
ssDNA	Single-stranded DNA
Sulfo-NHS	N-hydroxysulfosuccinimide
TEM	Transmission electron microscopy
T_m	Melting temperature
UA	Uric acid
UV-Vis	Ultraviolet–visible
V_{CNP}	Charge neutrality point
V_{DS}	Drain-source voltage
V_G	Gate voltage
XPS	X-ray photoelectron spectroscopy

Chapter 1 Background and Introduction

1.1. Graphene

1.1.1. Discovery

Graphene is a two dimensional allotrope of carbon, which carbon atoms bond covalently in sp^2 hybridization and arranged in a single layer planar sheet, honeycomb shaped crystal lattice. Theoretically, graphene can extend infinitely on a two dimensional plane. Graphene is the basic building block of graphite. When multiple layers of graphene stacked, they are classified as graphite (Novoselov et al., 2005). Speaking the other way round, if a single layer can be isolated from graphite, that layer will be “graphene”. The properties of that single layer are very special and different from its bulk material, graphite. In practical, stacks of graphene with less than ten layers is also considered as two dimension structure, which still processes the properties of graphene (Novoselov et al., 2005, Geim et al., 2007).

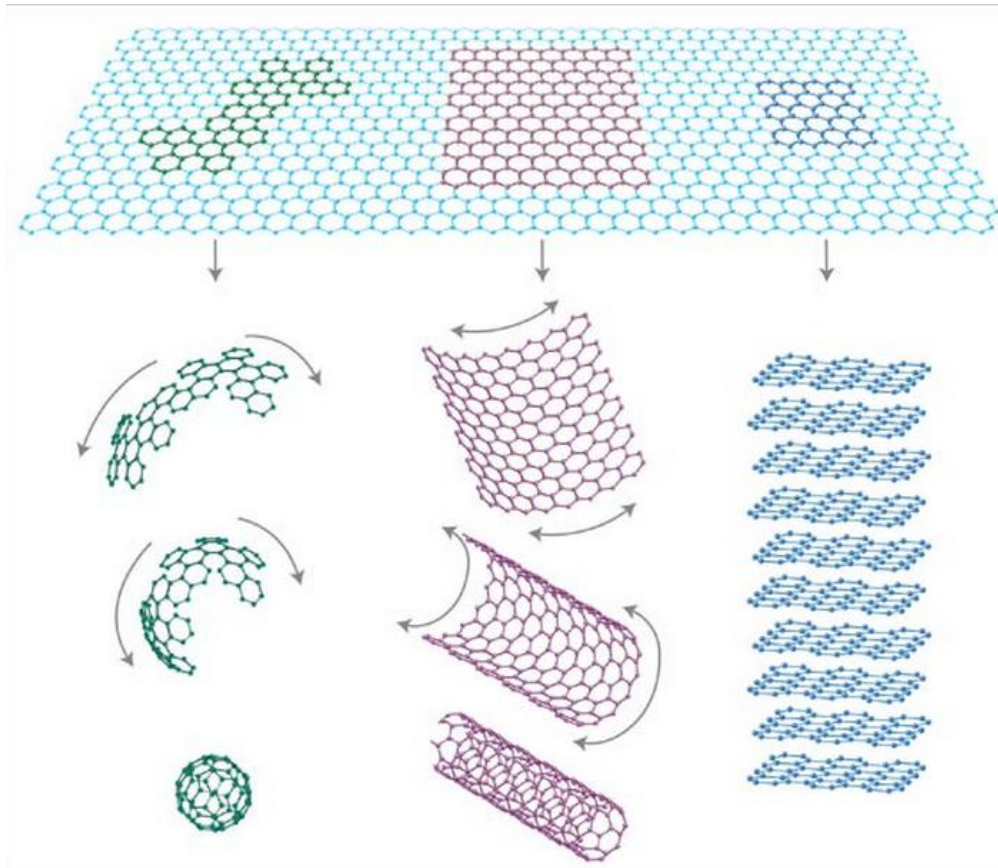


Figure 1.1.1. Graphene is the basic building block of different carbon-based materials. Graphene (top) can be wrapped into zero dimension buckyballs (bottom left), rolled into one dimension carbon nanotubes (bottom middle) and stacked into three-dimensional graphite (bottom right) (Adopted from Geim et al., 2007).

Graphene remained as a mystical material that only appeared in theories until it was successfully isolated in 2004 by Geim and Novoselov (Novoselov et al., 2005, Geim et al., 2007). The concept for its isolation was so simple that it started from graphite in an ordinary pencil (Novoselov et al., 2005).

When writing with a pencil, the trace of pencil mark is composed by graphite. If a

piece of bulk graphite is put onto a plastic adhesive paper, fold and open up again, the graphite flakes will be split into thinner halves (Novoselov et al., 2005). Continuing this process will finally yield a single layer of graphite, which is graphene (Novoselov et al., 2005). The analytical results of the product yielded by this method were found to be amazing. The graphene obtained was in extremely high crystal quality and great chemical stability (Novoselov et al., 2005). This groundbreaking discovery then ignited the exploration in graphene and started the era of two-dimensional materials. More and more efforts have been put into investigating the properties of graphene in the past decade and the era of two-dimensional materials was opened. Many possible applications have been developed and the investigations are still expanding.

1.1.2. Physical properties

As a two dimensional material, surface-area-to-volume ratio of graphene is extraordinary high. Regarding the single atomic layer structure in graphene, theoretically all atoms are exposed on the surface; give rise to an ultra-high surface area. The theoretical specific surface area of graphene reaches $2630 \text{ m}^2\text{g}^{-1}$ as reported in literature (Bonaccorso et al., 2015). This ultra-high

surface-area-to-volume ratio makes graphene a perfect material of a sensor. With larger surface, more targeting molecules can be immobilized on graphene, increasing the sensing performance of a sensor (Shao et al., 2010). With lesser bulk volume, graphene responds quickly and sensitively to subtle changes happens in the surrounding environment or the adherence of molecules (Shao et al., 2010). Besides the great sensing performance granted by the high surface-area-to-volume ratio, graphene also reduces the material cost needed in fabrication. Ideally, only one layer of graphene is needed to perform sensing function, while the carbon element is very abundant and relatively cheap in price. Graphene-based biosensor can be produced with low cost.

In graphene lattice, carbon atoms are bonded with localized σ bonds and delocalized π bonds. Most of materials with giant covalent structure are not conductive, while graphene is the exceptional one. In the outer-electron shell of carbon, there are four electrons. In graphene, only three of the outer-shell electrons are hybridized to form covalent bonds with other carbon atoms. The fourth outer shell electron is left freely available and delocalized on top or underneath the planar structure formed by carbon atoms. Those cloud of delocalized electrons in graphene are called “ π electrons” which greatly

contributed to its exceptional conductivity. Electron mobility measured in graphene at room temperature is $2.5 \times 10^5 \text{ cm}^2\text{V}^{-1} \text{ s}^{-1}$, which even exceeds the theoretical limit ($2 \times 10^5 \text{ cm}^2\text{V}^{-1} \text{ s}^{-1}$) (Novoselov et al., 2012). Besides the ultra-high electron mobility, physical properties of graphene are also superior. For example, Young's modulus measured in graphene is 1 TPa, intrinsic strength is 130 GPa, extremely high thermal conductivity, gas impermeability, etc (Novoselov et al., 2012). Currently, material scientists are keen on developing graphene as the next generation semiconductor in electronic applications (Novoselov et al., 2005, Geim et al., 2007, Bonaccorso et al., 2015). Applications of graphene is not only limited to semiconductor industry but it also demonstrated promising ability to be used in touch screen, organic light-emitting diode (OLED), ultra-fast transistor, super capacitor, contaminant remover, contrast agent, drug carrier, sensing technology, etc.

1.1.3. Graphene counterparts

There are several derivatives of graphene widely used in biosensing apart from the pristine one. Pristine graphene (usually prepared by mechanically exfoliating graphite) is the one with perfect crystal lattice of carbons, which exhibits the best

electronic properties. Although the electronic properties of pristine graphene are excellent, the fabrication process of it is extremely time consuming while mass production is almost impossible. Other types of graphene, for example, graphene oxide (GO), reduced graphene oxide (rGO) and graphene quantum dots (GQD) have various functional groups and size (from ~ 2 nm to ~ 1000 nm). These derivatives are all solution-processable which can be prepared in low cost, large scale with simple fabrication methods (Zhou et al., 2015). Although those derivatives of graphene with smaller lateral size (from a few nm to a few μm) are easier to produce, those oxygen related functional groups, or defects, scatter carriers in graphene that hamper its electronic properties. Detrimented electronic properties may give rise to an unstable and unreliable electronic biosensor.

1.1.4. Preparation of graphene

Similar to most of other nanoparticles, graphene preparation methods can be classified into two categories: a.) top-down and b.) bottom-up fabrication. Top-down fabrication breaks down large bulk precursor materials by the means of chemical or physical ways while bottom-up fabrication builds graphene from small precursor molecules. In this section, some examples of graphene preparation

methods and its development will be introduced.

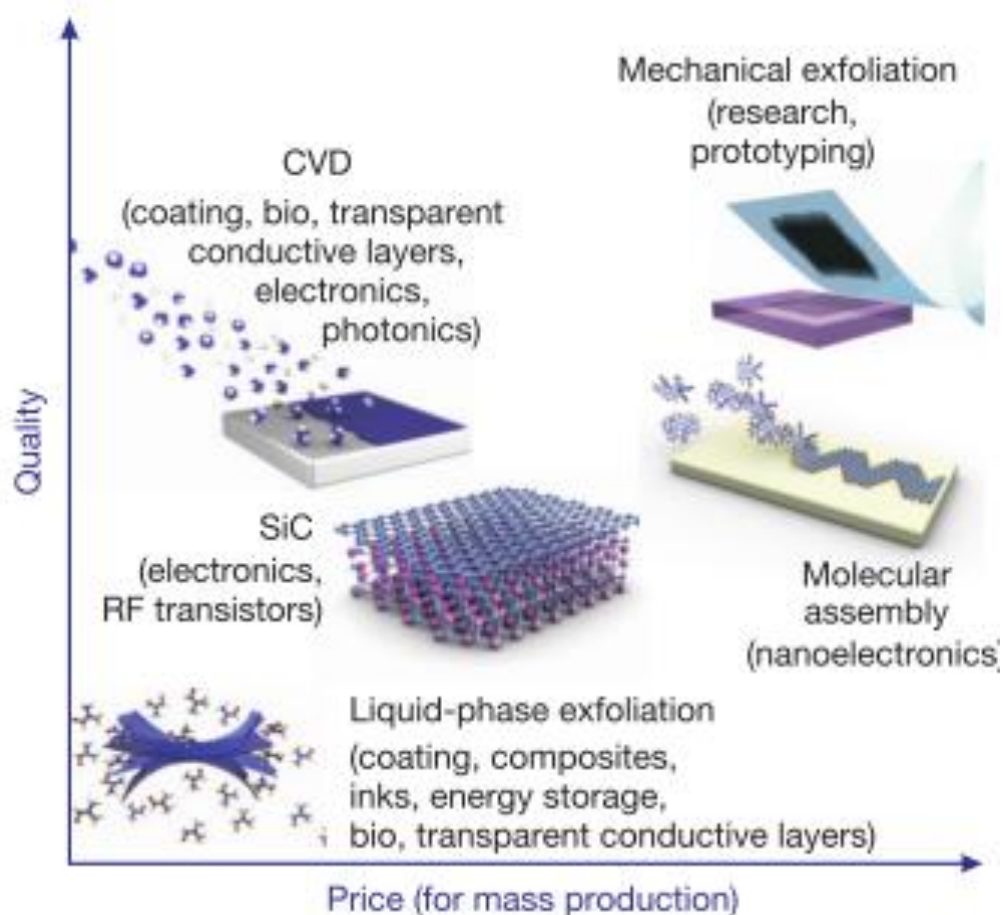


Figure 1.1.4. Overview on the existing methods for mass-producing graphene (Adopted from Novoselov et al., 2012).

1.1.4.1. Top-down fabrication

Among the reported top-down fabrication methods of graphene, the most famous one is the mechanical exfoliation accomplished by Geim and Novoselov, which won them the Nobel Prize in Physics 2010 (Novoselov et al., 2005). Apparatus

requires for mechanical exfoliation are extremely simple. A piece of graphite and a roll of scotch tape are all it needed to isolate pristine graphene. Graphite is merely a stack of graphene bound together by van der Waals bonds. To obtain graphene, the most straightforward thinking is to “peel” it off from the bulk graphite. Mechanical exfoliation is accomplished by putting a piece of graphene into a folded scotch tape. When the tape was opened, graphite in between was separated in half, one half on each side of the scotch tape. After repeating this process, the graphite is trimmed again and again, until there are only single layer of carbon left. The graphene exfoliated by scotch tape was then transferred onto a Si/SiO₂ wafer. Mechanical exfoliation provides extremely high quality graphene, which is very suitable for studying fundamental properties of two-dimensional materials. However, it is very time consuming to extract a single piece of graphene through mechanical exfoliation and the maximum lateral size is limited, making this method unrealistic to be used in electronic device fabrication.

After scotch-tape mechanical exfoliation was proposed, chemical exfoliation became another widely adopted method in preparing graphene. Chemical exfoliation is the way that utilizes chemical method to intercalate chemical groups or molecules in-between graphene layers in bulk graphite. The most famous

chemical exfoliation way is the modified Hummers method, which was reported in 1958 (Hummers et al., 1958). Hummers method oxidizes graphite powder under vigorous oxidation condition with sulfuric acid, sodium nitrate and potassium permanganate, yielding GO. Oxidation process grants GO various oxygen-related functional groups including hydroxyl, epoxy, carbonyl and carboxyl groups, which give GO hydrophilicity. The edges of GO were proposed to be terminated with carboxyl group (Schniepp et al., 2006). Carboxyl groups deprotonate and carry negative charge under relative alkaline environment, which aids the dispersion of GO by electrostatic repulsion force. Although GO can be facily prepared by Hummers method, the carbon crystal lattice is filled with defect and the conductivity of GO is low (Mohanty et al., 2008). To recover the electronic properties from the heavily oxidized GO, reduction is usually carried out after by introducing reducing agent, for example, hydrazine vapor, sodium borohydride and hydroiodic acid (Stankovich et al, 2007, Shin et al., 2009, Pei et al., 2010). Reduction of GO removes oxygen atoms and recovers carbon crystallinity, which both drastically improve the electrical conductivity (Pei et al., 2012). In fact, most of the graphene used in electrochemical biosensor is rGO, which has advantages in low fabrication cost, simple fabrication methods and good electrochemical catalytic ability. Besides the widely adopted chemical exfoliation via graphite

oxidation, electrochemical exfoliation, organic solvent exfoliation and sonication aided exfoliation have also demonstrated promising results in top-down graphene fabrication (Parvez et al., 2014, Khan et al, 2011, Ciesielski et al., 2014).

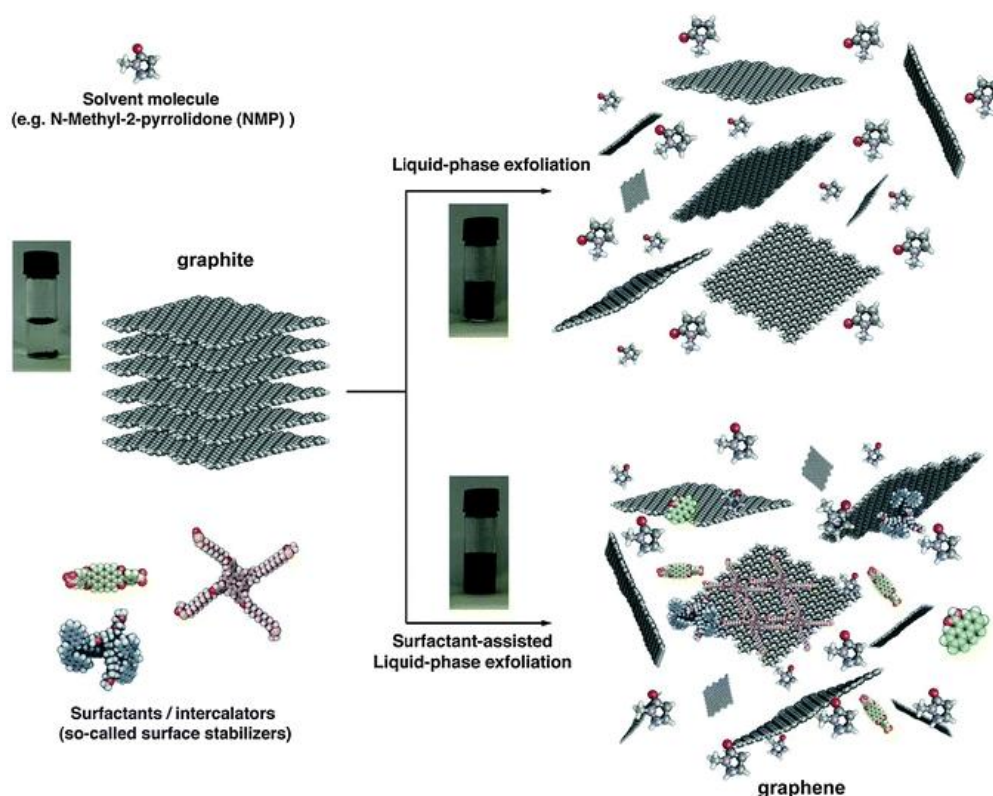


Figure 1.1.4.1. Example of a typical solution phase exfoliation process. graphite dissociate into single-layered graphene with the aid of surfactants, intercalators and ultrasound (Adopted from Ciesielski et al., 2014).

1.1.4.2. Bottom-up fabrication

Bottom-up fabrication approaches intend to build graphene from small precursors

that determine the chemical and physical behavior of the final products. To produce graphene from bottom-up pathway, the most promising approach is epitaxial growth and chemical vapor deposition (CVD). Yet, the CVD grown graphene is the most widely studied one (Berger et al., 2004; Berger et al., 2006, Yu et al., 2008, Li et al., 2009). CVD provides a facile way to fabricate graphene that quality is high enough and size is large enough for the potential application in semiconductor industry. CVD grown graphene also triumphs the epitaxial grown of graphene on SiC by its possibility to be exfoliated and transfer to an arbitrary substrate (Li et al., 2009, Suk et al., 2011).

To grow graphene by CVD, carbon precursor (usually methane) and hydrogen are passed through a metal catalysis at high temperature up to 1000 °C. The carbon atoms diffuse into the metal film at high temperature environment and segregate to form graphene during cooling. Well-controlled cooling rate, suitable metal catalyst with high crystallinity (or large grain) and low solubility of carbon are crucial to the formation of graphene with minimal defects (Yu et al., 2008, Li et al., 2009).

To turn CVD grown graphene into an electronic component, it is necessary to transfer it from the metal film catalyst to another substrate, for example, a Si/SiO₂ wafer. To transfer graphene, in brief, a layer of sacrificial carrier film is deposited

on the graphene in prior to etching process of the metal substrate. After the metal substrate underneath was completely etched away, graphene can be scooped up and transferred to any substrates. The choice of sacrificial carrier film comes in a wide range of options, including polydimethylsiloxane (PDMS), poly-methyl methacrylate (PMMA), thermal release tape and gold (Li et al., 2009, Bae et al., 2010, Chen et al., 2013). To date, CVD graphene growing and transfer technique are quite mature. CVD graphene on Si/SiO₂ wafer is widely commercially available while transfer of 30-inch graphene film onto a flexible substrate has also been demonstrated (Bae et al., 2010). The advancement in graphene production opens the door of mass-producing graphene-based electronic in industry scale.

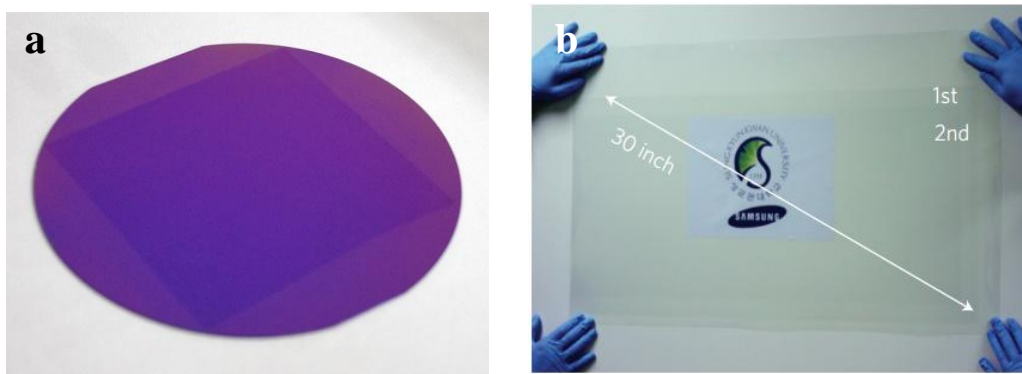


Figure 1.1.4.2. (a) Commercially available 7 cm X 7 cm CVD graphene on a 4 inch SiO₂ wafer (ACS Material). (b) 35 inches graphene/PET film transferred by thermal release tape as transparent electrode (Adopted from Seo et al., 2013; Bae et al., 2010).

1.2. Graphene in electrical biosensors

Through decades of development in biosensing, efficiently transducing a biological recognition event into a measurable physical signal is still challenging (Holzinger et al., 2014). Nanomaterials have proved themselves to be a promising candidate in biosensing which have the ability to increase probe immobilization density, lower detection limit, increase sensitivity, while some of them can also be a very effective transducing element (Holzinger et al., 2014). Graphene, a true two-dimensional nanomaterial, attracted major attentions in biosensing after its successful isolation and fabrication. In this section, fundamentals of biosensors and the development of graphene based electrical biosensors will be reviewed.

1.2.1. Fundamentals of biosensing

Concept of biosensor was initiated by Clark and Lyon (Clark et al., 1962, Park et al., 2014). Biosensor is a device that could provide analytical information against a specific target in a biological sample. The information provided can be used to determine a physiological event, justify the safeness of food or indicate the presence of any biological species. Concept of biosensing is illustrated in figure 1.2.1. A biosensor can generally be separated into two parts: a recognition element

and a transducer (Banica 2012). The recognition element interacts specifically with target species of our interest realizing a target-selective detection. There is a wide variety of recognition elements to be chosen from, including antibody, deoxyribonucleic acid (DNA), aptamer, ion selective membrane etc. These recognition elements all possess a target specific binding site in order to “recognize” the analytical target of our interest. After the target recognition event, that biosensor has to be able to translate such event into a readable physical signal. Considering the types of signal generated, biosensors can be classified into three categories: a.) electrical biosensors b.) optical biosensors and c.) acoustic wave sensors. Details of electrical biosensor will be described later in the chapter 1.2.2.

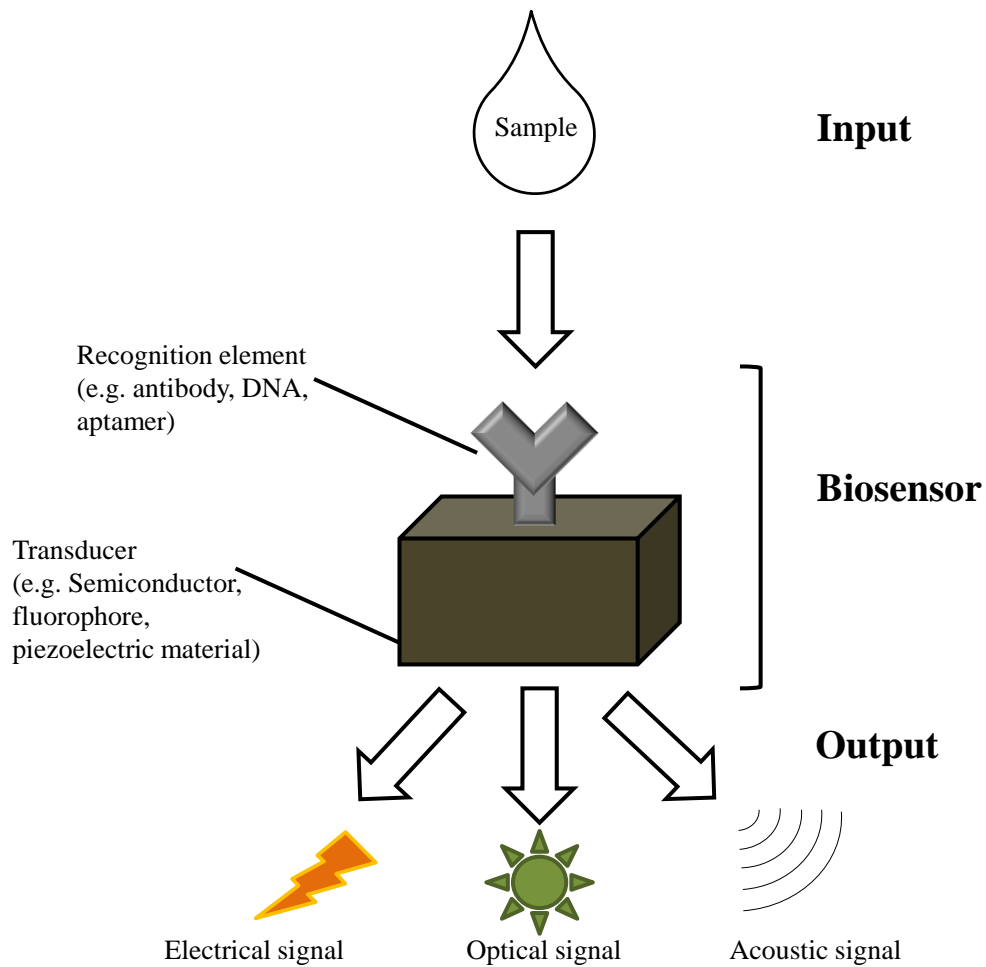


Figure 1.2.1. Schematic illustration of a biosensing process. Sample is introduced into a biosensor with a recognition element and a transducer. Recognition element interacts specifically with the detection target while the transducer translates the recognition event into physical signals.

Physical signals provide by electrical biosensors are mainly current, voltage and impedance, which makes the biosensors being named as amperometric, voltammetric and impedimetric biosensors respectively. Based on the different transducing mechanism, electrical biosensors can further be classified into electrochemical biosensors and field-effect transistor (FET) biosensor.

1.2.2. Electrochemical biosensors

Electrochemical biosensors usually consist of three electrodes: a.) working electrode, b.) counter electrode and c.) reference electrode (Grieshaber et al., 2008). Working electrode is the key transduction element while the counter electrode couples the redox reaction happens on the working electrode As for reference electrode, which usually is Ag/AgCl, aims to maintain a stable and known potential for electrochemical reaction.

Electrochemical biosensors can further be classified into three categories: a.) amperometric b.) potentiometric and c.) impedimetric (Hernandez et al., 2012). In amperometric biosensor, current generates from reduction or oxidation event on the working electrode is recorded when voltage with respect to the reference electrode is applied to an electrochemical cell. The electrochemical current correlates with the concentration or the accessibility of a redox-active species to the working electrode in the electrochemical system. However, target biomolecules of our interest are rarely electrochemically-active. In order to construct an electrochemical biosensor that can detect an electrochemically-inactive analyte, enzyme or redox label is often involved. The

most remarkable example of electrochemical biosensor is the glucose meter. Diabetic patients require a close monitoring on their blood glucose level, which create a huge demand on glucose sensor. Concept of glucose enzyme electrodes was first proposed in 1962 and Yellow Spring Instrument Company launched the first commercial product in 1975 (Wang et al., 2001).

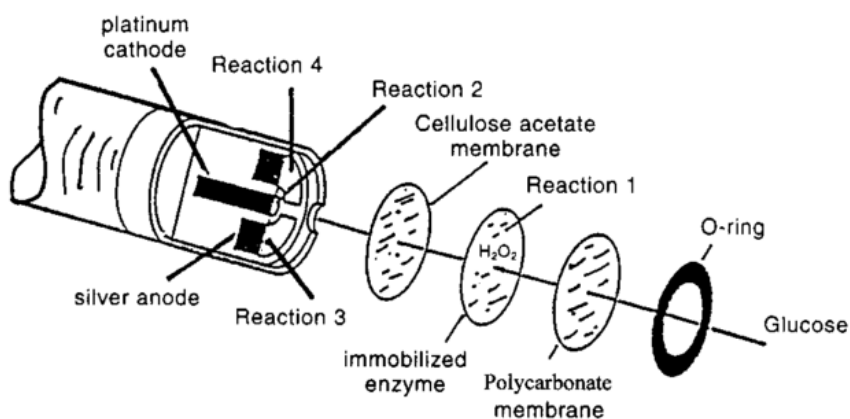
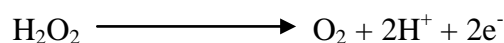


Figure 1.2.2. Schematic of the first commercialized glucose electrochemical biosensor (Adopted from Wang et al., 2001).

In the first glucose sensor, detection was achieved by incorporating glucose oxidase (GOx) in the sensor. GOx liberates hydrogen peroxide (H_2O_2) during the oxidation of glucose. H_2O_2 is electrochemically-active and the presence of it can be monitored by an electrochemical system. The reaction can be described by the following equation:



Benefiting from the specificity and catalytic ability of enzyme, enzyme is still a

very important element in most of the electrochemical biosensors. Although enzyme is a very good recognition element, it is very expensive to manufacture, unstable and difficult to preserve. Finding substitutes of enzyme and developing alternative enzyme-free detection schemes are also one of the most important research directions.

Different from amperometric measurement, potentiometric measurement adopts a different transduction approach. Potentiometric biosensor measures the potential difference created during ion exchange of two adjacent solutions when an ion-selective membrane is placed in-between. In these two solutions, one of them is the sample that needs to be analyzed and the other one is a standard solution with known concentration of target ion (Banica, 2012). The classic example of potentiometric sensor is pH-meter, which is also the very first chemical sensor commercially available in 1936 (Banica, 2012).

Electrochemical impedance spectroscopy (EIS) scans the impedance of a system with a range of alternative current (AC) frequencies and records the current response (Guan et al., 2004). With the aid of equivalent circuit models, different physical properties, including charge transfer resistance (R_{ct}) of the working

electrode, Faradaic current, non-Faradaic current, etc., of the electrochemical system can be studied. Impedimetric biosensor has lots of advantages including low fabrication cost, simple instrument setup and short analyzing time, however, detection accuracy and limit of detection is usually compromised (Daniels et al., 2007).

1.2.2.1. Graphene-based electrochemical biosensor

Even before the discovery of graphene, carbon-based materials have been playing an important role in electrochemical biosensing since glassy carbon electrode (GCE). The suitability of graphene in electrochemical biosensor depends on its superior electrocatalytic ability (Alwarappan et al., 2009). In a flake of graphene, there are two regions that possess different electrochemical behaviors: the basal plane and the edge plane (Yuan et al., 2013). Basal plane consists of carbon atoms in sp^2 hybridization forming honeycomb shaped lattice while the edge plane composes of high density of defective sites which have dangling bonds and different capping moieties (Casiraghi et al., 2009). Electrochemistry of the edge and basal plane in graphene was separately studied by Yuan et al. through selectively coating the basal/edge by non-conducting polymer and the results

suggested that graphene edge has higher electron-transfer rate and stronger electrocatalytic activity while the basal plane has a higher conductivity (Yuan et al., 2013). To modify an electrochemical electrode with graphene, it would be desirable to use graphene nanoflake with small lateral size rather than large, high quality, little defect pristine graphene.

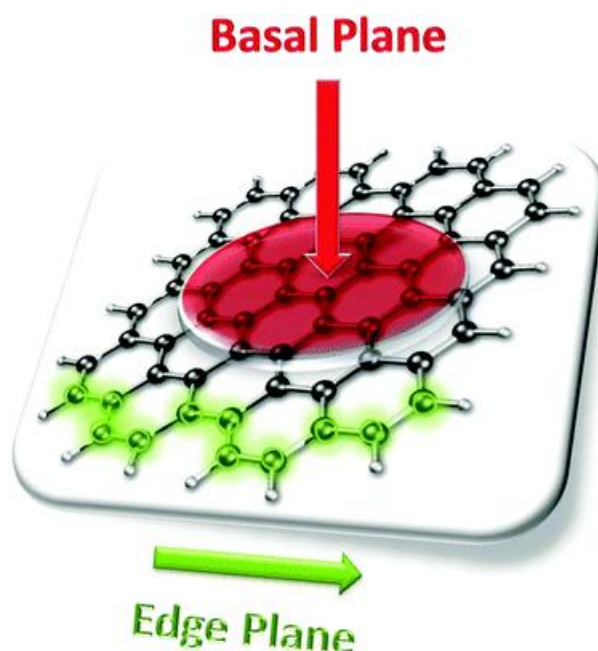


Figure 1.2.2.1. Graphical illustration of the edge and basal plane of a graphene flake. (Adopted from Brownson et al., 2012).

To determine the capability of a material in electrochemistry, several parameters have to be addressed, including but not limited to electron transfer rate and electrochemical potential window (Shao et al., 2009). Heterogeneous electron transfer of graphene based electrode with common redox couple, for example $[\text{Fe}(\text{CN})_6]^{3-/4-}$ and $[\text{Ru}(\text{NH}_3)_6]^{2+/3+}$ was found to be very rapid. Cathodic and anodic

currents in cyclic voltammetry (CV) were linear with square root of scan rate, suggesting the redox reaction is not limited by charge transfer but by the diffusion of redox probe (Lin et al., 2009, Tang et al., 2009). Besides the low R_{ct} , graphene also demonstrated a wide electrochemical potential window in 0.1 M phosphate buffer saline (PBS) (Zhou et al., 2009). The superior electrochemical performance of graphene established a solid ground for its application in biosensing.

1.2.2.2. Direct electrochemical detection using graphene-based electrodes

First attempt of using graphene in electrochemical biosensing was reported by Shang et al. in 2008 (Shang et al., 2008). In this study, multilayer graphene nanoflake films (MGNFs) was grown by microwave plasma enhanced CVD method and the MGNFs catalyzed rapid electron-transfer event between redox probe $[\text{Fe}(\text{CN})_6]^{3-/4-}$ and MGNPs while the direct electrocatalytic activity of dopamine (DA), ascorbic acid (AA) and uric acid (UA) was also found to be excellent. Besides of the enhanced electrochemical catalytic ability of MGNFs comparing with traditional GCE, three well-defined differential pulse voltammetry (DPV) peaks can be observed in a complex environment where AA, DA and UA coexist. The peak separation allows the simultaneous determination of

AA, DA and UA in a pot of mixture.

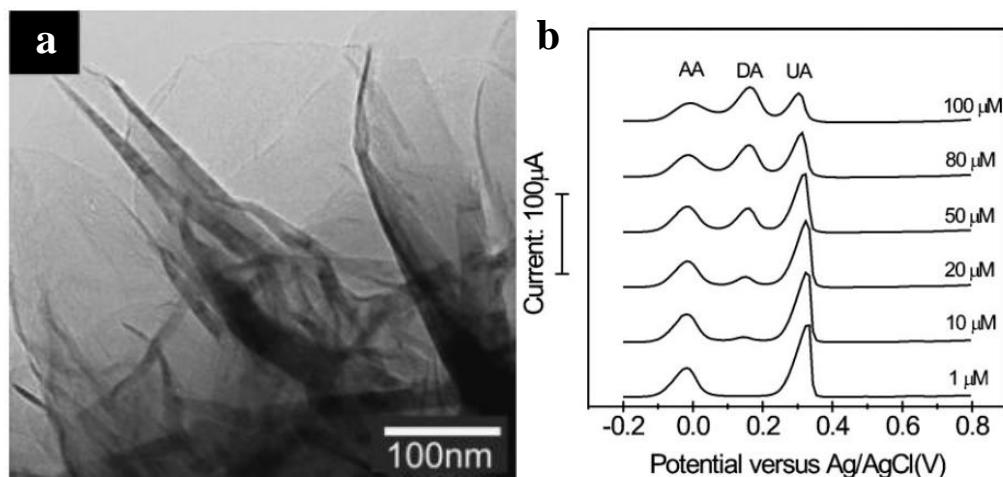


Figure 1.2.2.2. (a) Transmission electron microscopy (TEM) image of MGNFs fabricated by microwave plasma enhanced CVD. (b) DPV profile of MGNFs electrode with 1 mM AA, 0.1 mM UA and various concentrations of DA (Shang et al., 2008).

1.2.2.3. Enzyme decorated graphene-based electrochemical biosensor

After the direct electrochemical detection of AA, DA and UA using graphene-based electrode was reported, enzyme was incorporated with graphene in order to perform sensing with electrochemically-inactive target, for example, glucose. When immobilizing an enzyme to a working electrode, it would be desirable that the electrode is able to “communicate” with the enzyme through direct electron transfer. In 2009, Kang et al. and Shan et al. were able to achieve direct electron transfer between GOx and graphene based electrodes (Kang et al.,

2009, Shan et al., 2009). The glucose oxidation event on a GOx decorated graphene-modified electrode was found to be reversible, surface-confined process with high electron-transfer rate. Besides incorporate with GOx alone, metal nanoparticles, for example TiO₂ nanoparticles and gold nanoparticles (AuNPs), were incorporated with graphene-based electrodes. The nanoparticles modified electrodes shown an increased electrocatalytic activity (Shang et al., 2010, Jang et al., 2012). The synergistic effect between graphene and other nanoparticles further increased the sensitivity and stability of glucose biosensor.

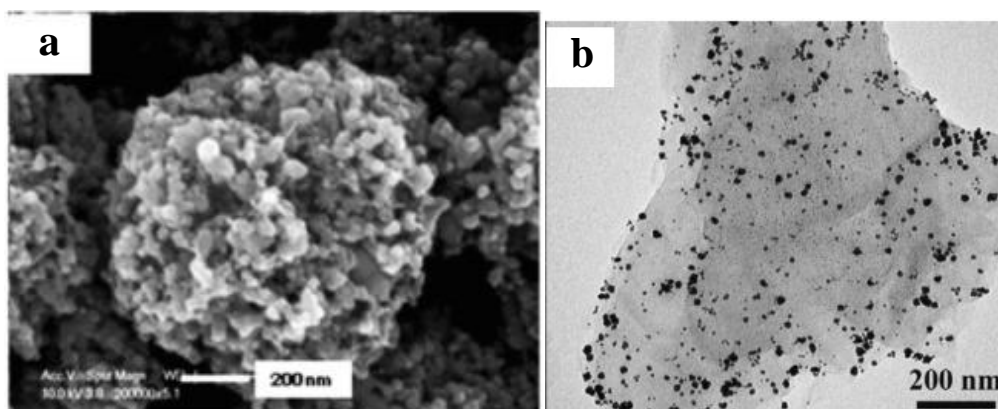
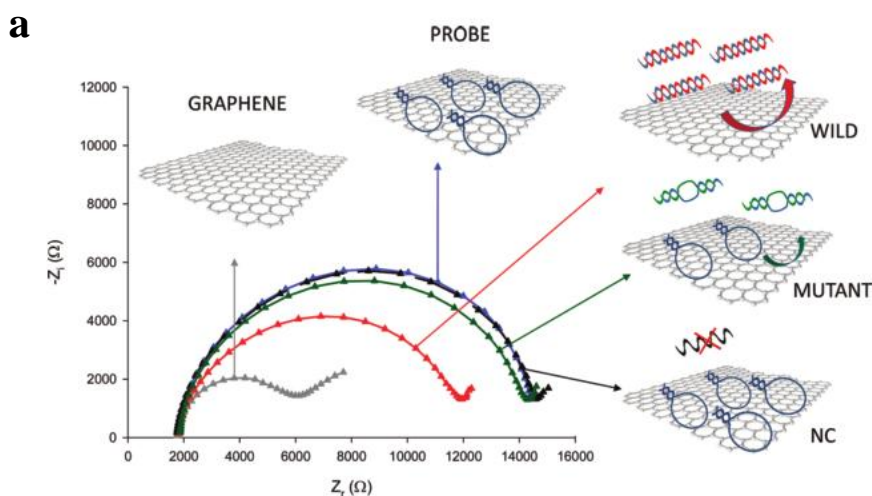


Figure 1.2.2.3. (a) TiO₂-graphene composite and (b) AuNPs decorated graphene engineered for electrochemical biosensing glucose (Adopted from Shang et al., 2010; Jang et al., 2012).

1.2.2.4. DNA detection using graphene-based electrochemical sensor

Graphene-based electrode for detection of electrochemically-active biomolecules or perform direct electron transfer with enzymes demonstrated promising results. Other complex electrochemical biosensing systems for detection of other biomolecules were also proposed afterwards, for example, DNA. DNA is the information carrier in any eukaryotic cells. Detecting the presence of certain sequence of DNA provides us abundant information of biological events including diagnosing disease or identifying of a pathogen. Although individual DNA bases could be discriminated and electrochemically detect by rGO modified electrode, it is difficult to oxidize nucleobases in a double-stranded DNA (dsDNA) and the sequence of it can hardly be justified by direct electrochemical oxidation (Zhou et al., 2009). In order to detect the presence of a strand of specific oligonucleotide, its complementary strand that can hybridize with the target sequence is usually used as a recognition element. In order to detect a DNA hybridization event, a graphene-based impedimetric biosensor was proposed (Bonanni et al., 2011). Target-complementary DNA probe in hair-pin conformation was first immobilized on a graphene electrode by π - π stacking. The immobilization of DNA probe blocked the redox probe ($[\text{Fe}(\text{CN})_6]^{3-/4-}$) from approaching the electrode thus increased its R_{ct} . Hybridization of probe DNA with target DNA folded the resulted dsDNA complex into a double-helix structure that destroyed the π - π stacking

attraction force between nucleobases and graphene. The hybridized dsDNA was then liberated from graphene surface thus reduced the R_{ct} of the graphene electrode. This sensing platform was sensitive enough to detect 3 pM DNA and discriminate wild type and mutant type DNA. Further attempt of using graphene-based electrode to electrochemically detect DNA was performed by Lin et al. (Lin et al., 2011). Instead of a fully complementary probe, an extended DNA capturing probe was utilized in order to capture target DNA onto the surface of graphene. Reporter probes with AuNPs conjugated on it was subsequently applied to perform another hybridization, forming a sandwich structure. Finally, silver enhancement was introduced and DPV signal of silver oxidation was recorder as the indicator for DNA detection. Limit of detection (LOD) of this setup was as low as 72 pM while it was able to distinguish single-base mismatch sequence.



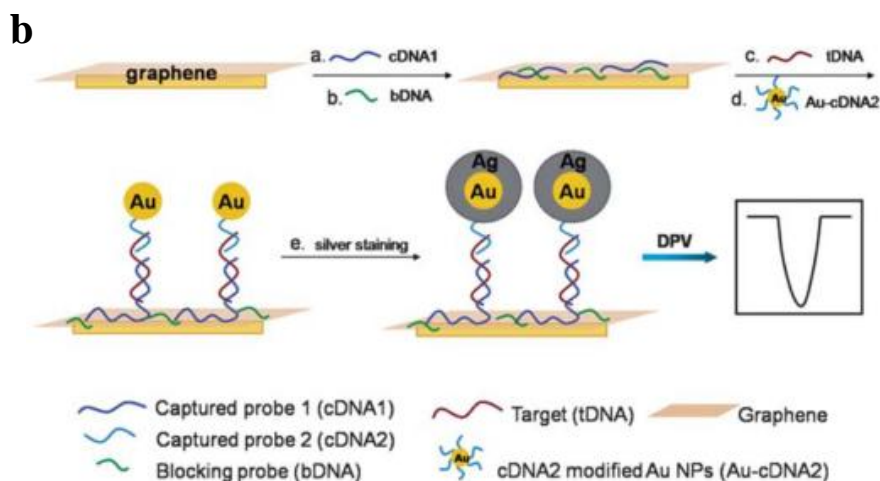


Figure 1.2.2.4. (a) An impedimetric biosensor with the aid of redox probe for detection of DNA hybridization event. Hybridization of target DNA with probe DNA reduced R_{ct} of graphene electrode (Adopted from Bonanni et al., 2011). (b) Extended capturing probe retained target DNA on the surface of graphene modified electrode. Subsequent AuNPs tags were introduced with silver enhancement and electrochemical signal of silver oxidation was read by DPV (Adopted from Lin et al., 2011).

1.2.3. Field-effect transistor (FET) biosensors

Development of FET biosensors can be dated back to late 70s' and early 80s' (Bergveld, 1970, Janata et al., 1976, Caras et al., 1980). FET attracted great attentions in biosensing. The nature of FET allows it to be miniaturized easily by well-developed photolithography technique. The intrinsic charge of biomolecules gate the conductance of FET thus giving it the advantage of label-free detection. Besides the aforementioned advantages, FET biosensors are usually able to provide real-time quantitative and ultra-sensitive measurement.

In a FET biosensor, the sensing element mainly consists of three components: a.) a semiconductor channel, b.) a pair of source/drain electrodes and c.) a gate dielectric. A standard FET device applies voltage to the semiconductor through the pair of source/drain electrodes while conductivity of the semiconductor channel is switched on/off by the application of gate voltage (V_G) across the dielectric layer. Classical semiconductor can be separated into two types: p-type and n-type. In a p-type semiconductor, hole concentration exceeds electron concentration where hole acts as the major carrier. Opposite to p-type semiconductor, n-type semiconductor has electron as major carrier. To explain the working mechanism of FET, p-type semiconductor is used as an example for illustration. When a positive voltage is applied on the gate electrode, an electrical double layer is formed in the dielectric where positive charge is repelled from the gate electrode and negative charge is attracted to it. The charged gate dielectric further depletes hole and attract electron in the p-type semiconductor, which decreases hole (major carrier) concentration. In the p-type semiconductor, the reduction of major carrier concentration increases its resistivity. Opposite event happens when negative voltage is applied via the gate electrode. In short, a p-type semiconductor is turned “off” while a positive V_G is applied and it is turned “on” while a negative V_G is applied. n-type semiconductor works vice versa. This electric-field-tunable

conductivity behavior allows semiconductor to be used in biosensing.

Traditional FET devices usually bury the semiconducting channel beneath a passivation layer and gates through a dielectric layer underneath. However, such configuration is not suitable in biosensing since it is necessary for the semiconductor channel to interact with target molecules. FET biosensor usually exposes the semiconducting channel to analyte, as illustrates in figure 1.5. a. By functionalizing the channel with recognition molecules (e.g. DNA, antibody), target biomolecules of our interest can be selectively captured to the proximity of the semiconductor channel. Usually, biomolecules are charged in analyte, either negative or positive. Those charges in biomolecules mimic the application of V_G when it is captured on the proximity of semiconductor channel. Electric field generated from the biomolecules alters the conductivity of the semiconductor channel, giving a readable physical signal. Figure 1.5. b illustrates the transfer curve of a p-type semiconductor before and after binding of negatively charged target. They negative charge carried by target biomolecules canceled out the application of positive V_G , which shifted the transfer curve to positive side. To study the binding event through electrical signal, two indicators can be used: a.) monitors source-drain current (I_{DS}) at a constant V_G and b.) calculates the shift of

threshold voltage by scanning transfer curve before and after addition of analyte.

The former approach enables real-time detection while the later one provides

detailed information on the semiconductor electrical property.

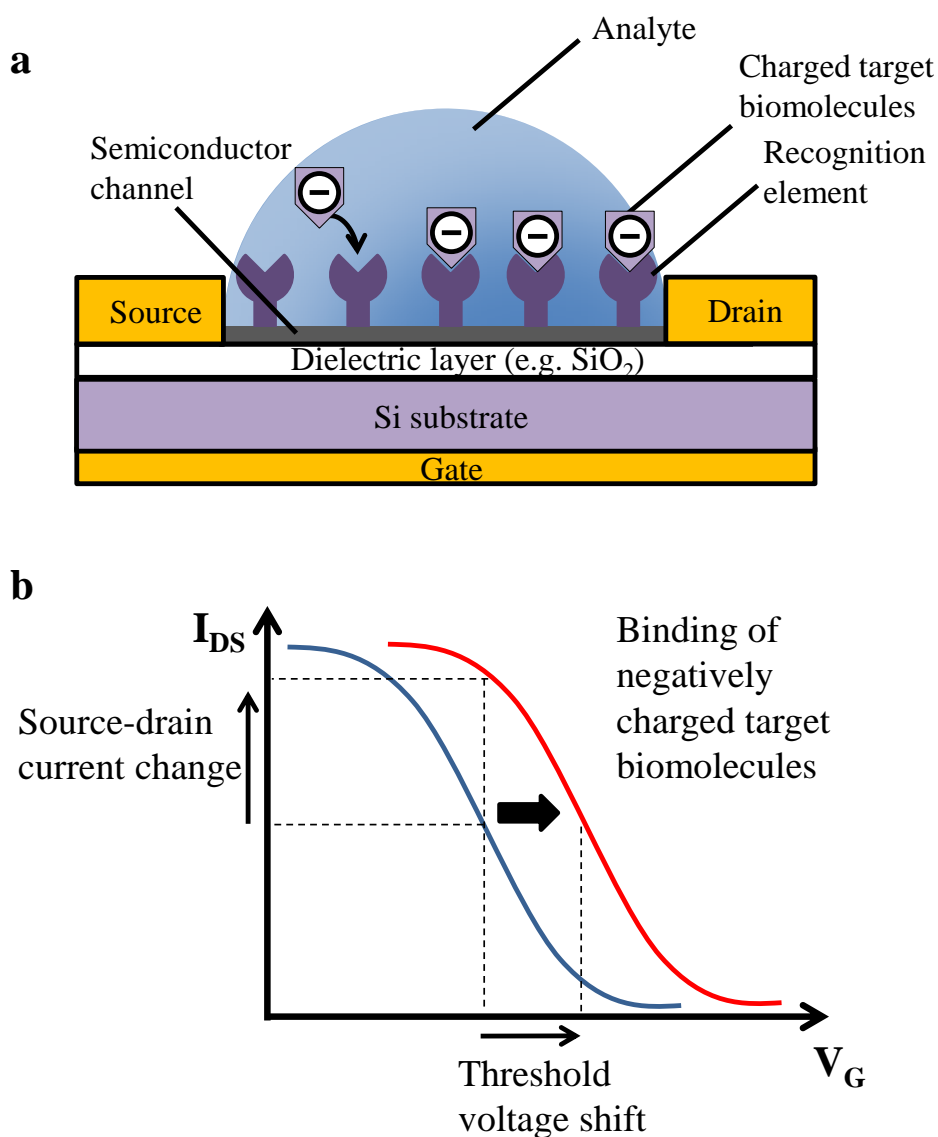


Figure 1.2.3. (a) Configuration of a typical FET biosensor. Charged biomolecules capture to the proximity of the semiconducting channel by recognition element and gate the semiconductor. (b) Transfer curve (blue) of a typical p-type

semiconductor. Binding of negatively charged target biomolecules shift the transfer curve to positive side (red). Change of semiconductor electrical behavior can be interpreted by either monitoring I_{DS} at a fixed V_G or study the shift of threshold voltage by scanning transfer curve.

1.2.3.1. Graphene-based FET biosensor

Graphene is a semi-metal, which intrinsically has semiconductor property, making it suitable for being the transduction element in a FET biosensor. Electronic behavior of graphene is very different from the conventional p-type or n-type semiconductor materials. Graphene is a zero band-gap material that behaves like a metal, which do not have any literal “off state” (Novoselov et al., 2012). Application of either negative or positive V_G increases carrier concentration and this phenomenon is described as “ambipolar electric field effect” (Geim et al., 2007). When $V_G = 0$ V, both carrier concentration (electron and hole) are close to each other giving a minimum conductivity of graphene. As V_G rises, electron concentration increases and become the major carrier. When a negative V_G is applied, hole then becomes the major carrier. Increasing V_G in either negative or positive direction both increases the major carrier concentration in graphene and increases its conductivity. This transition gives graphene a V-shaped transfer

curve.

1.2.3.2. Ion sensing by graphene-based FET

With the experience of the development in traditional ion-sensitive FET (ISFET), graphene FET based device was soon being used in pH sensing using solution gate.

The pioneering study reported a super-Nernstian sensitivity using graphene FET of 99 mV/pH (Ang et al., 2008). Solution gate is a setup that applies V_G from the buffer solution on top of the channel area rather than a solid gate dielectric. In this case, the gate dielectric is not a conventional solid-layer. Instead, the ion flow in buffer solution during the application of V_G generates a localized ions concentration on the proximity of graphene, which gate its conductivity. Solution gate is not only beneficial for detecting targets dissolve in aqueous solution, but also increases trans-conductance by 30 folds (Zhan et al., 2014). Although graphene-based pH FET sensor seems to be attractive, the mechanism behind is still controversial and a later report suggested that graphene transistors are actually insensitive to pH (Fu et al., 2011). Instead, the defect site and oxygenated-functional groups on graphene should be responsible for the Dirac

voltage shift under different pH values. Graphene FET has demonstrated its great potential in pH sensing. Soon after that, platforms using graphene transistors to detect other harmful small ions including heavy metal Pb^{2+} and Hg^{2+} were reported. Selective detection of Pb^{2+} can be achieved by immobilizing Pb^{2+} specific DNzyme on AuNPs decorated graphene FET channel (Wen et al., 2013). DNzyme is a Pb^{2+} specific DNA sequence consisted of an enzymatic strand and a substrate strand. In the presence of Pb^{2+} , the enzymatic strand cleaved the substrate strand, removing them from the proximity of graphene. With a lesser number of nucleobases on graphene surface, doping effect poses by nucleobases was reduced and shifted the Dirac voltage of graphene to positive side. Using the DNzyme system, detection limit of AuNPs decorated graphene FET device against Pb^{2+} reached as low as 20 pM.

In order to detect Hg^{2+} , DNA strands were also demonstrated to be a successful recognition element (An et al., 2013). In DNA hybridization, T-A and C-G pairs are the common and natural combination. Hg^{2+} is known to be able to induce T-T mismatch hybridization by forming T- Hg^{2+} -T. Using this Hg^{2+} induced hybridization, An et al., designed an aptamer which was able to selectively capture Hg^{2+} in the analyte by forming the aforementioned T- Hg^{2+} -T complex (An et al.,

2013). The Hg^{2+} specific aptamer was immobilized on graphene transistor surface by Schiff-base reaction and the detection limit reaches 10 pM. Besides the low detection limit, this graphene transistor was also able to detect Hg^{2+} in mussels extract prepared from real-world sample suggested the biosensor was able to take the role in real world application.

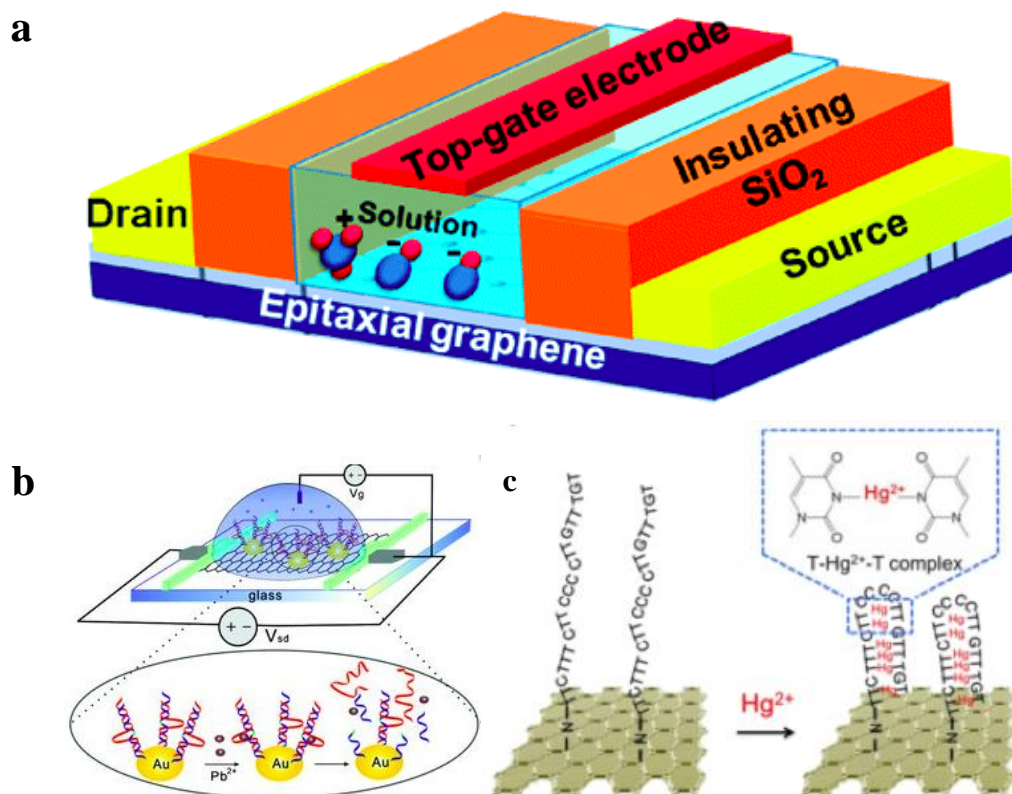


Figure 1.2.3.2. Schematic of Graphene FET being used in (a) pH sensing with solution gate (Adopted from Ang et al., 2008) (b) Pb^{2+} sensing using DNAzyme as recognition element (Adopted from Wen et al., 2013) and (c) Hg^{2+} sensing functionalized with Hg^{2+} specific aptamer (Adopted from An et al., 2013).

1.2.3.3. DNA and bacterial sensing using graphene-based FET

The first attempt of using graphene-based FET to detect biomolecules was reported in 2008 (Mohanty et al., 2008). Mohanty et al. used GO as the semiconductor channel. Electrical property of GO was found to be similar to a p-type semiconductor and it was used as a transducing element to detect *Geobacter* and DNA. *Geobacter* is a bacteria carries negative charge on the cell wall. To detect bacteria using GO, the GO surface was exposed to ammonia plasma in order to change the surface charge of GO to positive. Positively charged surface of GO attracts bacteria by electrostatic interaction. The negative charge on bacteria cell wall increased the conductivity of GO and increased the slope of I-V curve of GO. This graphene FET device was able to detect bacteria down to a single bacterium level while the bacteria adhered on PGA (plasma modified graphene-amine) were still alive. After the work of Mohanty et al., Mannor et al. further expanded the graphene FET-based sensor into a bio-transplantable device by printing graphene onto water soluble-silk (Mannoor et al., 2011). The sensor can be transferred to other biomaterials including tooth enamel while providing real-time monitoring of bacteria down to single-cell level. More importantly, the sensing signal can be read by a resonant coil, which eliminated the need of on board power and wiring.

DNA is a very attractive biomolecules that can provide precise analytical information of the target species. In order to recognize a fragment of DNA (target DNA), the common approach is to immobilize the complementary strand (capturing) onto the sensing surface. By forming T-A and C-G bases pairing between target and capturing probe, the target is captured onto the sensing surface. DNA is a very effective recognizing tool since it can recognize target in a very specific way with good stability and low cost.

The first report of detecting DNA using graphene based FET device was achieved by Mohanty et al. (Mohanty et al., 2008). Target complementary amine modified capturing probe (the recognition element) was covalently immobilized onto the surface of GO semiconductor channel using 1-[Bis(dimethylamino)methylene]-1H-1,2,3-triazolo[4,5-b]pyridinium 3-oxid hexafluorophosphate (HATU). Attachment of DNA caused a conductivity increase in GO. The change was explained by their negative potential gating effect, which increased hole concentration in GO. Since GO was found to be a p-type semi-conductor, increase in hole concentration increased the conductivity of GO. After hybridization, dehybridization of target DNA using urea was found to be able to almost fully recover the electrical property of GO, suggesting their sensor

was very robust and re-use of a single FET biosensor is possible.

Apart from using graphene alone as transduction element, there are some following reports synergistically combining metal nanoparticles with graphene to achieve a better DNA sensing result (Dong et al., 2010; Yin et al., 2011). Dong et al. decorated CVD graphene with AuNPs allowing thiol-modified probe DNA to be covalently immobilized on the FET channel (Dong et al., 2010). Adding AuNPs improved the upper detection limit of the suggested graphene FET DNA biosensor from 10 nM to 500 nM, which was explained by the increment of probe density on graphene surface. Later, Yun et al. directly synthesized Platinum nanoparticles (PtNPs) on rGO by photochemical reduction (Yin et al., 2011). Interestingly, the introduction of PtNPs did not alter the electronic properties of graphene obviously but it greatly enhanced the detection sensitivity. More recently, Cai et al. reported a graphene FET DNA biosensor using peptide nucleic acid (PNA) as recognition element. PNA is a DNA mimicking molecule that can hybridize with DNA but carries no charge. The uncharged PNA probe enhanced performance of the biosensor by reducing the electrostatic repulsion force between target DNA and capturing probe. With a neutral probe, doping and electrostatic gating posed by the probe molecules are minimal thus reduced the background interference. By using

PNA, the suggested graphene-based FET DNA biosensor achieved a yet lowest detection limit of 100 fM comparing with previous reports.

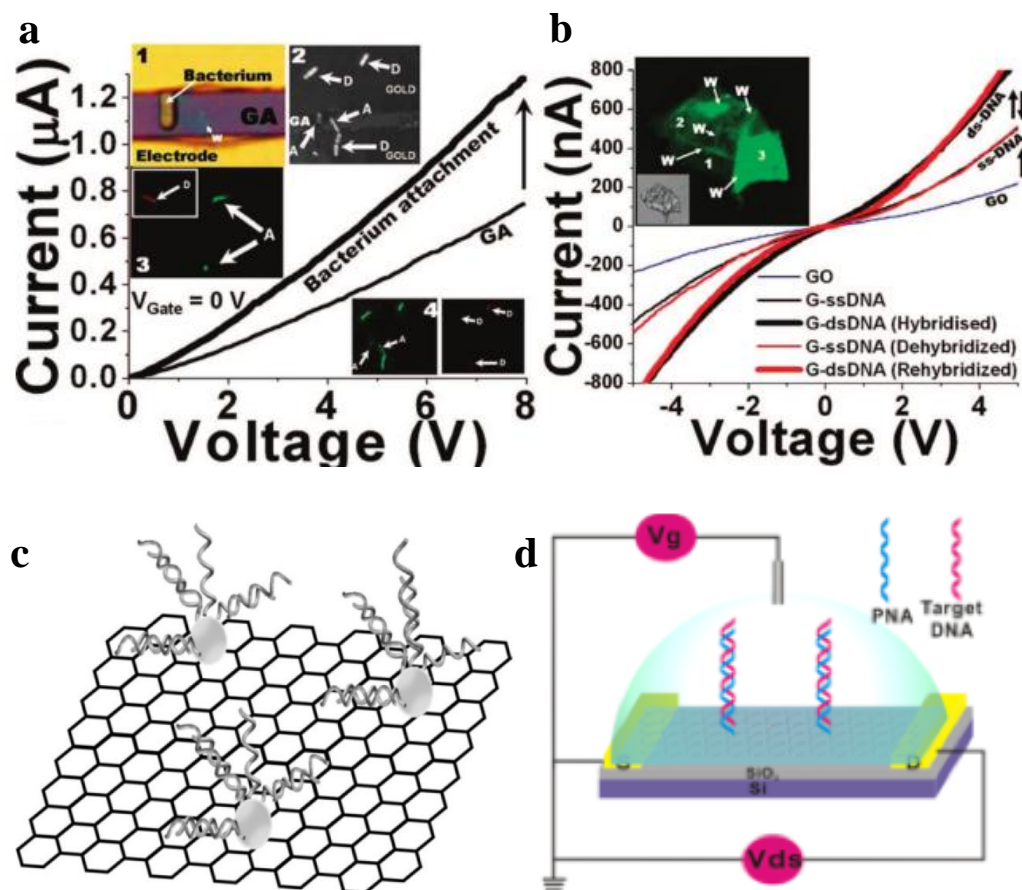


Figure 1.2.3.3. Schematic of (a) graphene-amine (GA) FET biosensor which was able to detect negatively charged bacteria and (b) DNA, depending on the functionalization approach that was carried out (Adopted from Mohanty et al., 2008). (c) AuNPs decorated CVD graphene for DNA detection (Adopted from Dong et al., 2010). (d) Graphene FET sensor using PNA as a recognition element (Adopted from Cai et al., 2014).

1.2.3.4. Protein detection

Protein detection provides precious and direct physiological and diagnostic

information of a patient. Diseased patients usually have a change of biomarker level in body fluid. By measuring the level of certain biomarker, which is usually a protein, early diagnostic can be performed in order to save life. To recognize target protein in an analyte, immunoassay utilizing specific antibody-antigen binding interaction is very effective. The first demonstration using graphene FET to detect protein-binding event was reported by Mao et al. (Mao et al., 2010). Mao et al. applied an AuNPs decorated rGO channel to detect the capturing of Immunoglobulin G (IgG) by anti-IgG while the anti-IgG was immobilized on AuNPs as capturing probe. Later, the same research group developed dc plasma-enhanced chemical vapor deposition (dc-PECVD) to grow vertically-oriented graphene as FET channel to detect IgG (Mao et al., 2013). This novel design allowed protein in analyte to access the FET channel more easily while the fabrication procedure was simpler with better physical stability. More importantly, this report provided new insights in modifying the graphene FET channel for a better biosensing performance by changing the conformation of FET channel. Besides the vertically-oriented graphene, Myung et al. developed another fascinating way to fabricate graphene based FET channel (Myung et al., 2011). Instead of the conventionally two-dimension structure, they encapsulated positively charged SiO₂ nanoparticles with GO by electrostatic attraction force.

Afterward, the GO-NPs were deposited onto a substrate by centrifugation and photolithography technique. After removing photoresist and reduction of GO, a FET channel composed with spherical-shaped rGO coated nanoparticles was formed. This fabrication method allows arrays of FET detection channel to be fabricated in a high density, low-cost and facile way. Finally, the graphene channels was covalently functionalized with two types of monoclonal antibody, which specifically target Human Epidermal growth factor Receptor 2 (HER2) or epidermal growth factor receptor (EGFR). HER2 and EGFR are well-known breast cancer biomarkers that can provide early diagnostic information. The spherical structure of graphene in the FET channel greatly increased the surface-to-volume ratio therefore improved detection limit. This setup was demonstrated to be able to detect down to 1 pM HER2 and 100 pM EGFR and seems to be a good candidate in clinical diagnosis.

Although antibody is a versatile tool for capturing target, it still suffers from several disadvantages such as high manufacturing cost and low stability. Recently, aptamer seems to be taking up the role of which antibody has been playing for the past decades. Aptamer is a strand of nucleic acid that can be folded into certain conformation and possess high affinity to a specific target molecule (Hernandez et

al., 2012). Comparing with antibody, aptamer can be synthesized in vitro with low cost and high stability in extreme environment. When being used in FET biosensor as molecular receptor, aptamer can greatly decrease the distance between target molecule and FET channel benefited from the relatively small size of it. When the distance between FET channel and target is reduced, doping or gating effect posed by target can be enhanced and there is a lesser chance that the biomolecule will be captured beyond the Debye's length. Ohno et al. used Immunoglobulin E (IgE) aptamer to modify graphene FET in order to detect Human IgE (Ohno et al., 2010). The height of IgE aptamer was reported to be roughly 3 nm and the protein-aptamer interactions are expected to be happening inside Debye's length. In this experiment, IgE can be detected in real-time by monitoring I_{DS} . Binding of positively charged IgE decreased the conductance of graphene that could be attributed to the electrostatic gating effect.

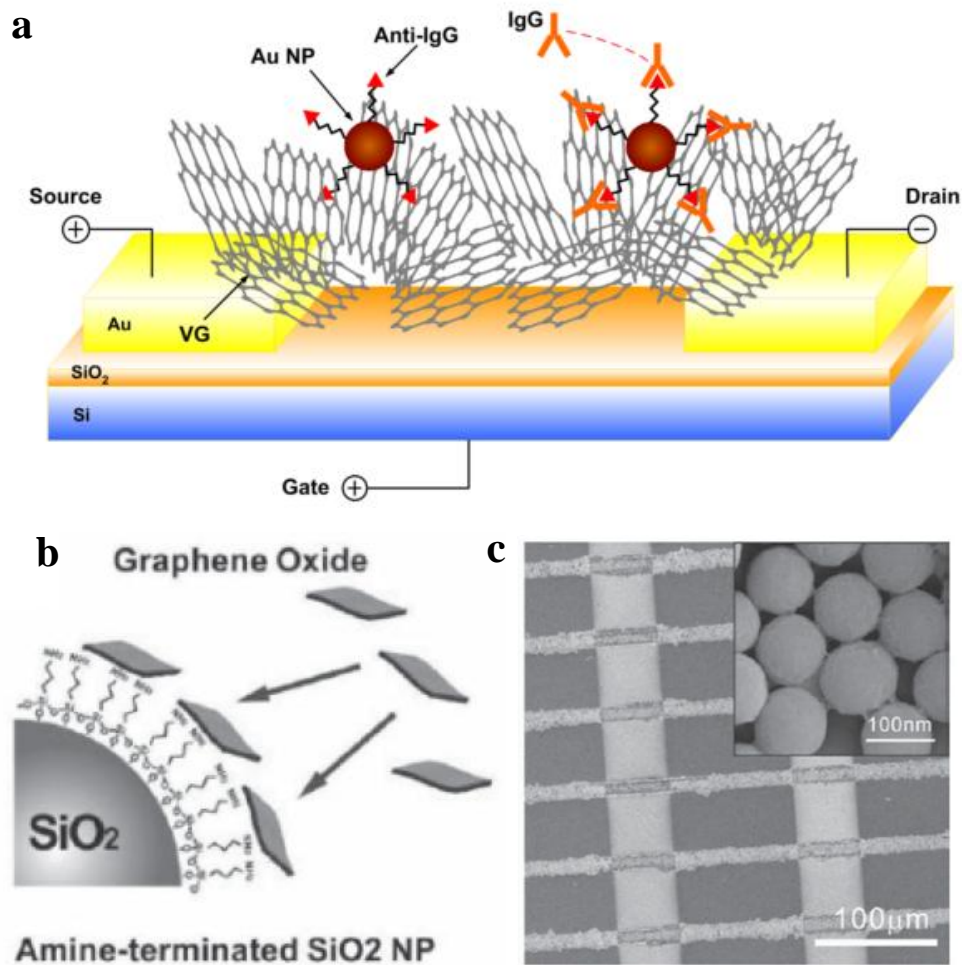


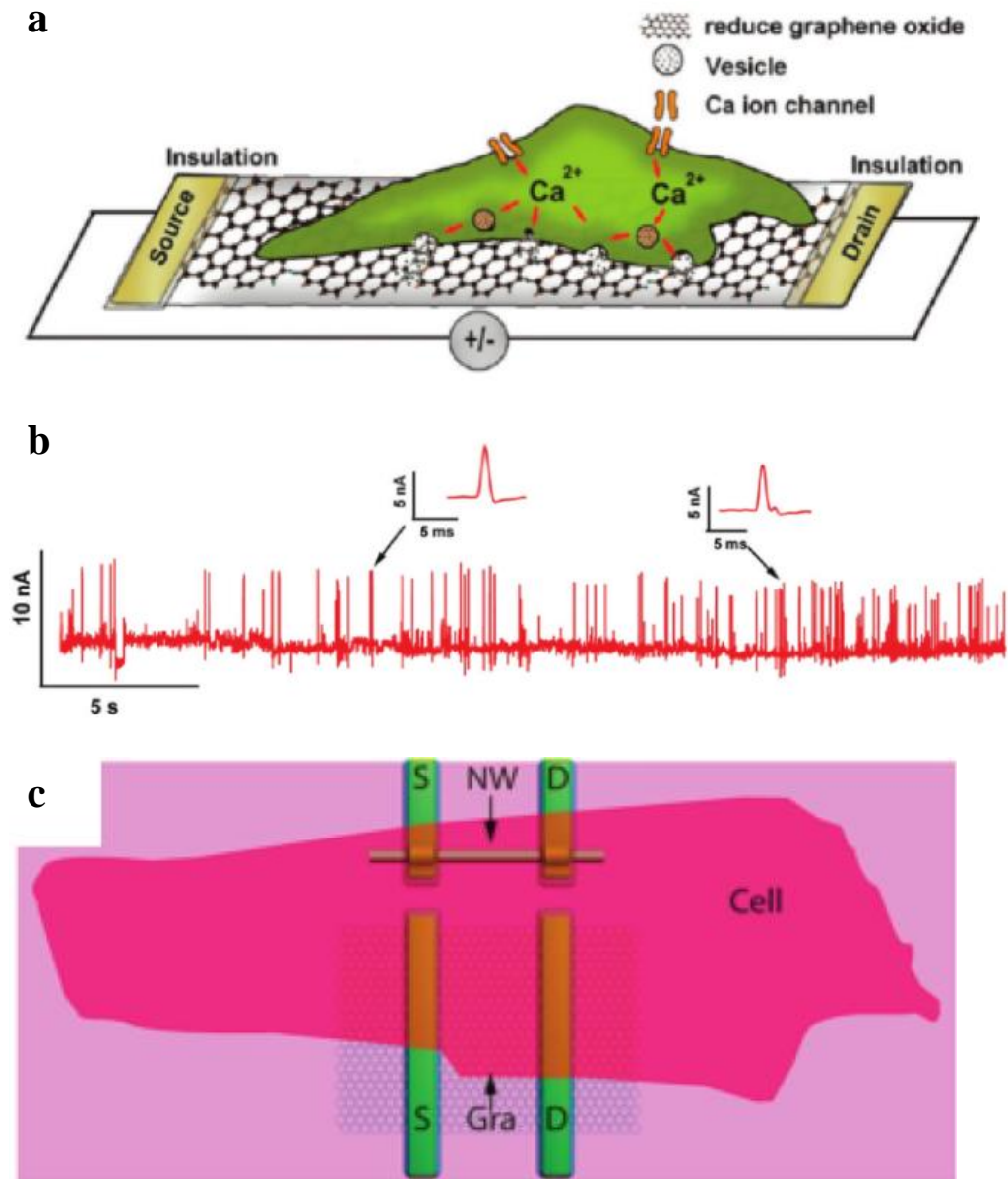
Figure 1.2.3.4. Schematic of (a) AuNPs decorated vertically-oriented graphene for sensing IgG (Adopted from Mao et al., 2010) and (b) GO coated SiO₂ nanoparticles, which were subsequently deposited on a substrate. (c) Scanning electron microscopy (SEM) image of arrays of GO-NPs FET channels formed on a substrate using photolithography technique (Adopted from Myung et al., 2011).

1.2.3.5. Cell based graphene FET device

Except for functionalizing graphene FET with conventional recognition molecules, several researches applied graphene FET to interfere with living cells in order to monitor their metabolic activities or even use the living cells as a recognition

element. In 2010, He et al. and Cohen-Karni et al. both presented graphene FET device for monitoring biological activity of living cells (He et al., 2010, Cohen-Karni et al.). In the research of He et al., parallel arrays of rGO channel were fabricated by micromolding in capillary method (He et al., 2010). The as-fabricated rGO FET channels were first proven to be able to detect DA. Soon after that, they pushed forward to detect cellular activity in rat pheochromocytoma (PC12) by directly culturing PC12 on top of poly-L-lysine-coated rGO. Under high K^+ environment, cell membrane of PC12 depolarized and opened the voltage-gated Ca^{2+} channel leading to an influx of Ca^{2+} and release of catecholamine containing vesicles. This series of events generated spikes of current response in the real-time monitoring of rGO conductivity. Each spike in the I-t measurement can be attributed to a vesicle release event. In the work of Cohen-Karni et al., graphene FET was directly interfered with embryonic chicken cardiomyocytes, which are electrogenic cells (Cohen-Karni et al., 2010). The embryonic chicken cardiomyocytes is a layer of cells that beat and create action potential constantly. Action potential of cardiomyocytes on the proximity of graphene provides electric field and gated the graphene FET channel. In the real-time conductance monitoring, well-defined peaks were observed with high signal-to-noise ratio. When tuning the operating regime of graphene from p-type

to n-type by the application of positive V_G , a flip of signal phase was observed, clearly demonstrated that the signal recorded was due to field-effect.



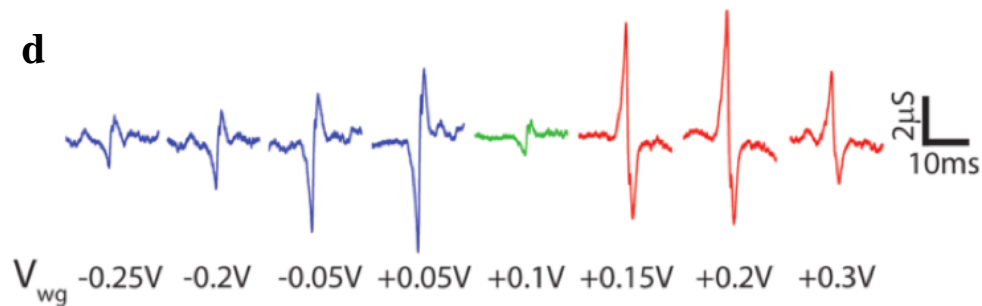


Figure 1.2.3.5. Schematic of (a) PC12 directly cultured on poly-L-lysine-coated rGO FET channel. K^+ induced release of catecholamine containing vesicles induced gating of FET conductivity and (b) displayed peaks on real-time conductance measurement (Adopted from He et al., 2010). (c) Electrogenic embryonic chicken cardiomyocytes cultured on graphene FET and (d) action potential generated from cardiomyocytes gated graphene FET conductance under different biased V_G (Adopted from Cohen-Karni et al., 2010).

1.3. Objectives of study

In this thesis, three original studies were performed and present in chapter 2, chapter 3 and chapter 4 respectively. Chapter 2 used rGO to fabricate bioFET in order to study the effect of different probe immobilization strategies on the performance of biosensing. Chapter 3 followed the work in chapter 2 and developed a CVD graphene-based bioFET for DNA detection with the aid of reporter probe-AuNPs composite for signal amplification, yielding a much more sensitive bioFET. Chapter 4 developed a rGO electrochemical biosensing system for the detection of neurotoxin. Details of objectives of those studies are as follows:

Objectives of study in chapter 2:

- a.) Construct a rGO-based bioFET for real-time H5N1 avian influenza virus gene sequence detection.
- b.) Immobilize long capture probe on rGO FET via π - π stacking for bioFET DNA detection.
- c.) Compare the effect of different capture probe immobilization approaches (long capture probe, short capture probe and covalent immobilization of amine-modified capture probe on bioFET performance in DNA detection.

Objectives of study in chapter 3:

- a.) Fabricate a CVD graphene-based solution-gated bioFET for detection of H7 virus genome.
- b.) Apply reporter probe conjugated AuNPs to enhance bioFET biosensing performance.

Objectives of study in chapter 4:

- a.) Construct a rGO based working electrode for electrochemical biosensing.
- b.) Functionalize rGO electrode with SNAP-25 for sensing enzymatic activity of

BoNT-LcA.

c.) Evaluate the detection limit, dynamic range and interference effect of real-life sample of the fabricated rGO/Au based electrochemical biosensor against

BoNT-LcA.

Chapter 2 Reduced Graphene Oxide Transistor with Extended DNA Capture Probe for DNA Detection

2.1. Introduction

Biological field-effect transistor (bioFET) is a promising platform for biosensing.

A bioFET measures change of semiconductor electrical properties induced by electric potential generated from binding event of biological targets on the gate surface (Brand et al., 1991). BioFET has numerous advantages including label-free, quick responding, low-cost and sensitive detection of biological targets.

Traditional silicon based semiconductor technology has been widely used in bioFET devices; however, they have relatively low sensitivities, which hampers its applications in biosensing (Kergoat et al., 2012, Lee et al., 2009). Recently, advancements in the application of nanomaterials improved the performance of bioFET greatly. Nanomaterials having semiconductor property for example, silicon nanowire, carbon-nanotube and graphene were proved to be promising candidates in biosensing.

Graphene, a novel two-dimensional single atomic planar sheet, has attracted

tremendous attentions in biosensing application due to its high carrier mobility, large surface area and highly tunable chemical and physical behaviour (Geim et al., 2007, Geim et al., 2009). In theory, all carbon atoms in graphene are exposed to surrounding environment, electrical properties of graphene film are extremely sensitive to the binding events of chemical or biological molecules on its surface, which favors graphene to be a potential candidate in bioFET device for ultrasensitive detection (Cohen-Karni et al., 2010, Kuila et al., 2011).

During the fabrication process of a biosensing system, a common procedure namely biofunctionalization is necessary. Biofunctionalization allows capture probes, or recognition elements, to be immobilized on a transducer for recognition of target biomolecule of interest, giving a target specific biosensing system. The key challenge of a graphene bioFET is to realize a stable and reliable immobilization of recognition element on graphene surface while preserving the extraordinary electronic property of graphene simultaneously. Covalent immobilization such as silane-based modification is a very reliable approach for immobilizing a recognition probe. However, forming covalent bond on graphene disrupts the crystal lattice of graphene and thus detracts carrier mobility and scatters electrons traveling through it (Georgakilas et al., 2012). Besides covalent

immobilization, utilizing π - π stacking interaction force is an effective way to achieve biofunctionalization on graphene-based material. π - π stacking is a kind of van der Waals bonding that bind molecules with rich π electrons to graphene (Karimi et al., 2014). Bifunctional linker molecules with pyrene-terminated groups such as pyrenebutyric acid (PA) are an example of molecules having rich π electrons. The pyrene-end in the linker molecule strongly bind with the basal plane of graphene via π - π stacking interaction, integrity of graphene crystal structure and the electronic property can hence be preserved (Georgakilas et al., 2012, Pembroke et al., 2013). The carboxyl terminus in PA is then available for further covalent conjugation of biomolecules on graphene surface. Despite the advantages, using bifunctional linker increases the distance between target molecules and graphene FET channel, which may greatly decrease the sensitivity of a FET biosensor.

In nature, there are certain biomolecules that possess rich π electrons and can be self-assembled on graphene. Nucleobases in DNA are one of the examples of biomolecules that has very rich π electrons. Self-assembling capture probe DNA on graphene surface via π - π stacking interaction is one of the widely adopted methods for graphene-based bioFET targeting DNA. Affinity between DNA and

graphene is very high and the binding is very reliable while the immobilization process is simple and facile (Zhang et al., 2013, Stine et al., 2010).

In most of the previous reports on graphene bioFET targeting DNA, capture probes are sometimes immobilized on graphene via purely π - π stacking interaction force (Dong et al., 2010, Chen et al., 2013, Lin et al., 2013). Among those examples, capture probes and target DNA have exactly the same length and matching sequence. When complimentary targets hybridize with capture probes, the resulted fully hybridized dsDNA has poor affinity to graphene surface. The formation of dsDNA generates a helical structure, which shields the nucleobases inside while exposes the negatively charged phosphate backbone outward. Hybridizing with fully complementary target tends to detach capture probes from graphene surface and such mechanism was even developed into various optical sensing platforms (Huang et al., 2012, Lu et al., 2009 and Liu et al., 2011). This phenomenon may be helpful in optical biosensing, but when this happens in a graphene-based bioFET, it may severely hamper the reliability of the sensor since the effect of hybridized probe detachment counters the effect of target capturing. This issue may become even more noticeable when washing step is employed on a bioFET, which is commonly used to remove non-specific adsorption of non-target

molecules.

In order to overcome the probe detachment problem in graphene-based bioFET when capture probe was immobilized via π - π stacking, an extended capture probe was suggested in this project. Then extended long capture probe used in this project has an extended oligonucleotide sequence beyond the one fully complementary to target DNA. After hybridization, the complementary portion hybridizes with target while the extended sequence remains single-stranded. Although the dsDNA portion loses the ability to π - π stack with graphene, the extended ssDNA portion retains the ability of forming π - π stacking with graphene, holding the whole complex on graphene tightly.

As a demonstration, this rGO transistor with long capture probe was used for H5N1 avian influenza virus gene sequence detection. Here, we compared different DNA capture probe immobilization approaches and their effect on rGO transistor. In total, three probe immobilizing approaches were testified in this project: a.) fully complementary “short capture probe” b.) extended “long capture probe” we proposed and c.) PA “covalent bifunctional linker” involved covalent immobilization of capture probe. The long capture probe we proposed was

composed of two sections: one section with sequence complementary to target DNA and an extended region was designed for maintaining π - π stacking interaction force between DNA and graphene, allowing the capture probe-target dsDNA complex to be retained on rGO surface. After examining the three capture probe immobilization approaches, long capture probe setup was found to be providing the best bioFET DNA sensing performance with highest sensitivity and good stability after target hybridization event.

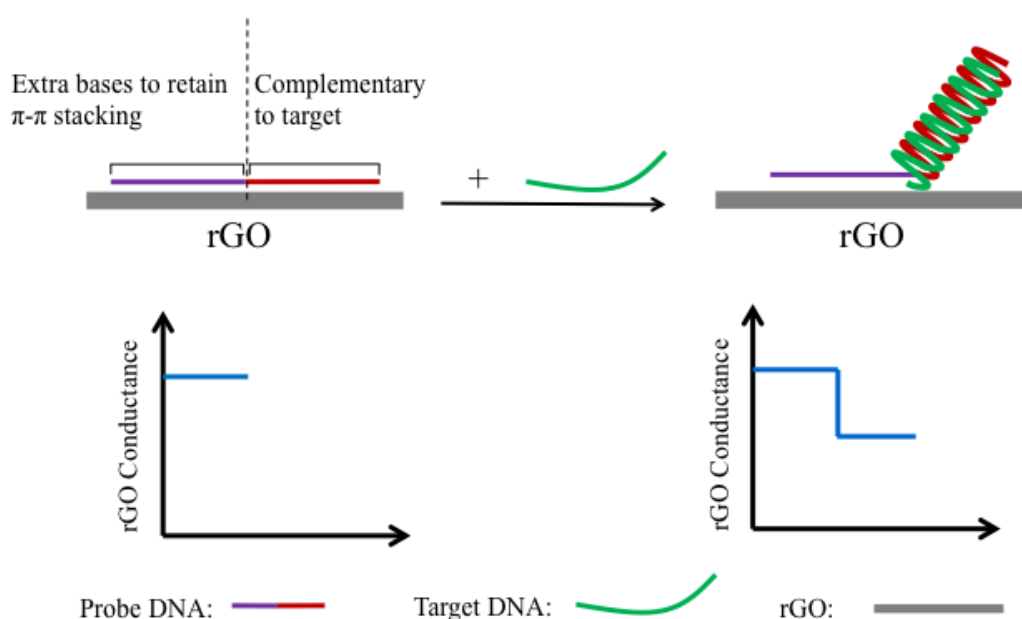


Figure 2.1. Schematic illustration of long capture probe suggested in this project. Long capture probe composed with two sections: a.) complementary sequence recognize and capture target DNA and b.) extended DNA sequence retains π - π stacking with graphene after target hybridization. Capture of target DNA on rGO surface decreased the conductance of rGO while conductance of rGO channel was monitored in real-time after analyte introduction.

2.2. Research methodology

2.2.1. Materials

GO (5 mg/mL) was purchased from Graphene Supermarket. Phosphate buffered saline (PBS), sodium dodecyl sulfate (SDS), 1-pyrenebutyric Acid (PA), 3-aminopropyltriethoxysilane (APTES), sulfuric acid, hydrogen peroxide (H₂O₂), N-hydroxysulfosuccinimide (Sulfo-NHS) and hydrazine monohydrate were purchased from Sigma-Aldrich. N,N-Dimethylformamide (DMF) was purchased from Acros Silicon wafer (300 nm SiO₂ layer on Si) was purchased from MTI Corporation. N-(3-Dimethylaminopropyl)-N'-ethylcarbodiimide hydrochloride (EDC) was purchased from Fluka. Oligonucleotides were synthesized by Integrated DNA Technologies (IDT) Inc. (Coralville, IA, US). The oligonucleotides used in this experiment include:

Short capture probe: 5'-TTT GAG TCT GTT GCT TGG-3'

Fluorescent-labeled short capture probe: 5'-TTT GAG TCT GTT GCT TGG-Cy3-3'

Long capture probe: 5'-GTG TGT GTG TGT GTG TGT GTG TGT GTG TGT TTT GAG TCT GTT GCT TGG-3'

Fluorescent-labeled long capture probe: 5'-GTG TGT GTG TGT GTG TGT GTG
TGT GTG TGT TTT GAG TCT GTT GCT TGG-Cy3-3'

Amine modified short capture probe: 5'-NH₂-TTT GAG TCT GTT GCT TGG-3'

H5N1 Target (cDNA): 5'-CCA AGC AAC AGA CTC AAA-3'

Non-Complementary DNA (non-cDNA): 5'-TTA TTC CCT GAA AAA TTG-3'

2.2.2. Preparation of rGO transistor

Preparation of rGO film on a Si/SiO₂ wafer followed a previous report (Ou et al., 2010). Briefly, Si/SiO₂ wafer was treated by piranha solution for 30 minutes to generate hydroxyl groups on SiO₂. Afterward, Si/SiO₂ was salinized by immersing it in acetone with 1% for APTES for one hour. Then, GO (5 mg/mL) was spin-coated on the substrate and air-dried afterwards. Finally, hydrazine vapor reduction was performed overnight at 85 °C. The obtained rGO film was shielded by a hard mask and etched to a 1 mm width band by plasma treatment. Subsequently, Ti/Au contact pads were sputtered and patterned as contact electrodes with 4 mm separation. The patterned rGO channel has dimension of 4 mm x 1 mm. A PDMS block with a 4 mm diameter cylindrically-shaped reservoir was attached on the chip in order to passivate the contact pads.

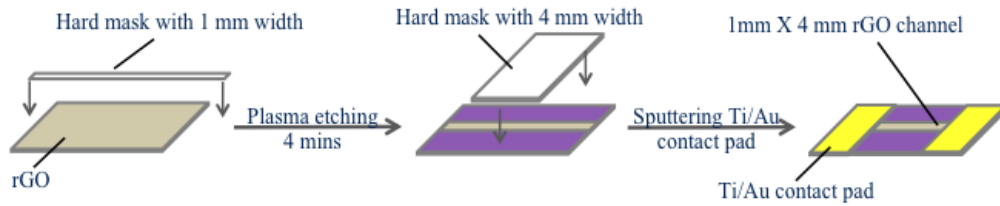


Figure 2.2.2. Illustration of rGO FET channel fabrication process.

2.2.3. Immobilization of capture probe on rGO channel

Long capture probe and short capture probe were immobilized on rGO FET by π - π stacking after the transistor chip was fabricated. Briefly, a 20 μ L PBS (1X PBS, pH 7.4) solution of 10 μ M capture probe (either long capture probe or short capture probe) was incubated on the rGO channel overnight at room temperature. Afterwards, the loosely bonded DNA was removed by rinsing with 0.2 % SDS in PBS solution, PBS solution and deionized water (DI water) sequentially.

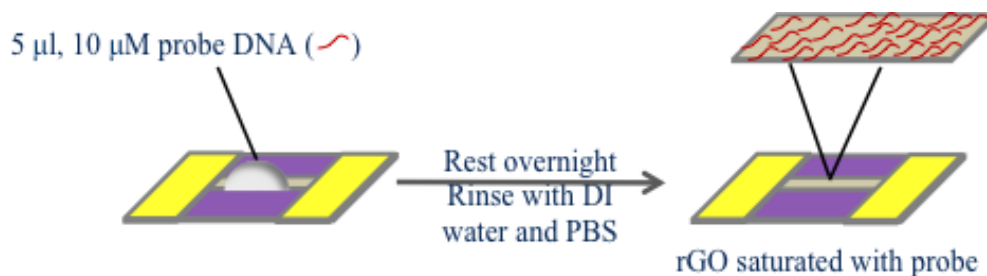


Figure 2.2.3.1. Illustration of long capture probe and short capture probe immobilization via π - π stacking.

In order to achieve covalent functionalization of capture probe, rGO was firstly functionalized with PA. Firstly, 20 μL of PA solution (10 mM) in DMF was dropped on the rGO channel and incubated overnight. Afterwards, the rGO channel was rinsed with DMF and DI water in sequence. After air-dried, EDC/NHS in 1X MES buffer was then applied to activate the carboxyl groups on rGO channel for 30 min. Afterwards, a 20 μL amine-modified short capture probe in 10 μM was added for covalently bonding to PA. After resting overnight, the rGO channel was rinsed by PBS and DI water to remove other loosely attached probes.

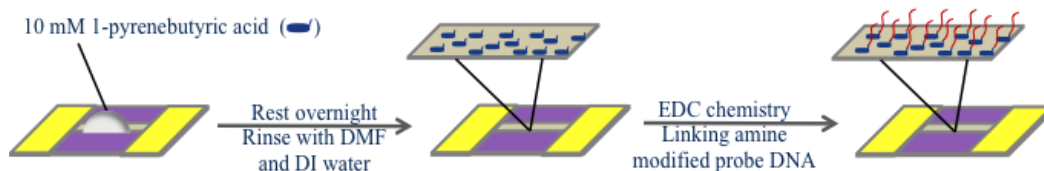


Figure 2.2.3.2. Illustration of amine-modified short capture probe immobilization process.

2.2.4. Hybridization experiment

Hybridization was performed by incubating 20 μL of cDNA or non-cDNA in 1X PBS buffer to the rGO channel. The hybridization time for each experiment was

set as 2 hr. After hybridization was completed, the rGO channel was washed by 1X PBS containing 0.2% SDS, 1X PBS, and DI water in sequence or three times.

2.2.5. Preparation of rGO transistor

rGO transistor bioFET was measured with a semiconductor parameter analyzer (Keithley 4200). During the measurement, a blank 1X PBS was used as reference measurement electrolyte. Original conductance (G_o) was defined as the channel conductance when 1X PBS was added into the sample chamber. Real-time measured conductance was defined as (G) Device response was calculated as the relative conductance change $\Delta G/G_o$. Different concentration of cDNA and non-cDNA was injected into the analyte at different time interval for real-time measurement.

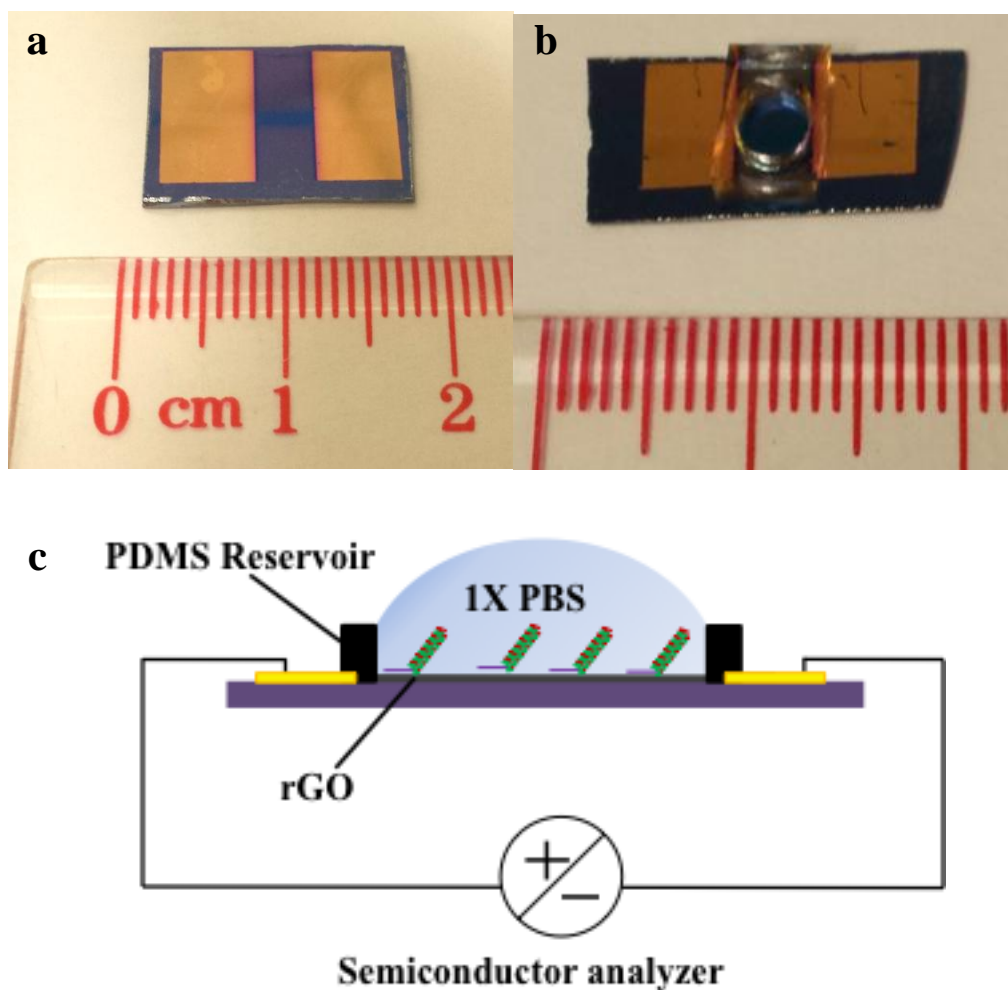


Figure 2.2.5. Optical image of an (a) as fabricated rGO transistor and (b) the rGO FET channel incorporated with a PDMS reservoir. (c) Illustration of setup in electrical measurement of rGO bioFET.

2.2.6. Instrumentations

Atomic force microscopy (AFM) experiment of rGO morphology was performed with a multifunctional Scanning Probe Microscopy (Digital Instruments NanoScope IV). Raman spectra of GO and rGO were measured by a Horiba

Jobin-Yvon Raman system (LabRam HR800) equipped with a 488 nm laser excitation source. X-ray photoelectron spectroscopy (XPS) spectra were characterized by SKL-12 spectrometer modified with VG CLAM 4 multichannel hemispherical analyzer. Electrical signal of rGO bioFET was recorded by Keithley 4200. Fluorescent experiment was performed with a Tecan Infinite F200 microplate reader.

2.3. Results and discussion

2.3.1. AFM characterization of the morphology of rGO film

After the rGO film was fabricated on Si/SiO₂ substrate, AFM was utilized to study the film morphology and result presents in figure 2.3.1. In general, a large area and continuous rGO film with few layers of rGO staked together was obtained on a Si/SiO₂ substrate by spin-coating method. The size of single rGO flakes was roughly 500 nm. This continuous rGO film is composed of single layer of rGO sheets and two to three overlapping layers of rGO sheets. Thickness of a single rGO film was roughly 1.5 nm and certain area in the rGO channel reached approximately 5 nm, suggesting there were three to four layers of rGO staked

together.

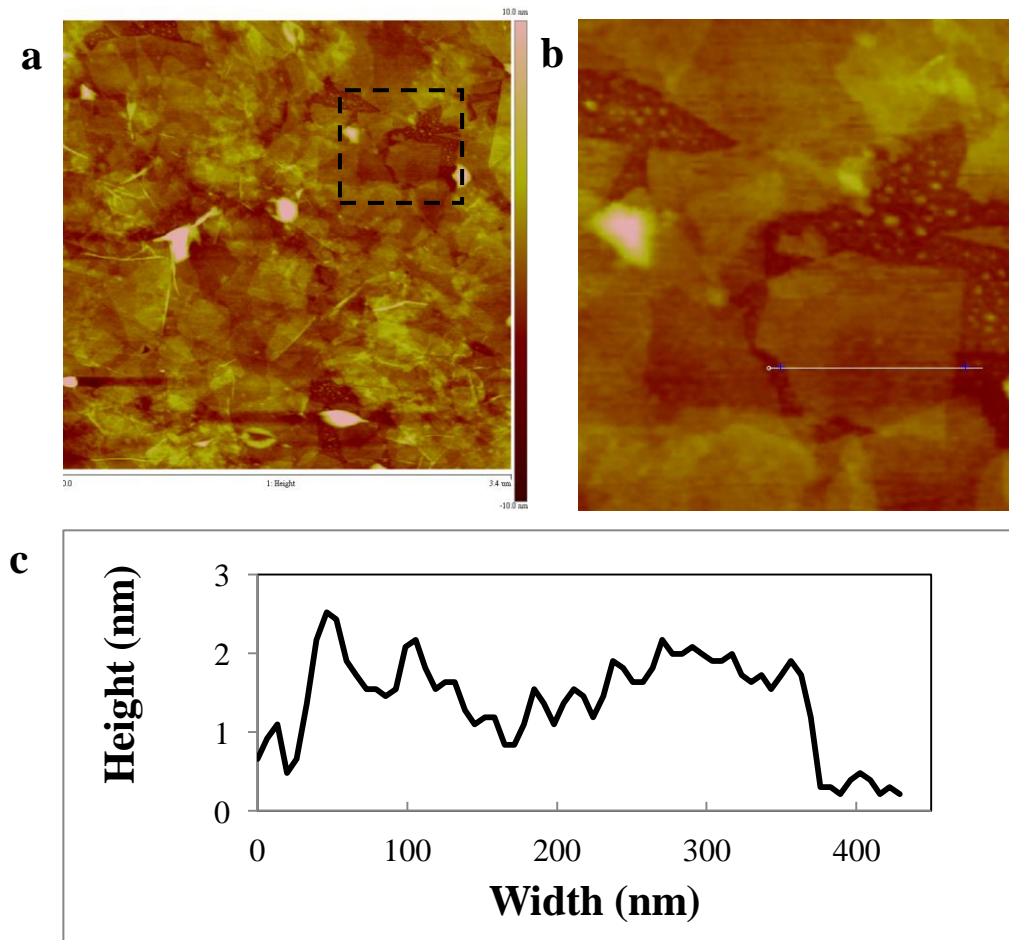


Figure 2.3.1. (a) AFM image of a rGO film and (b) enlarged portion of the AFM image (c) height profile of rGO film on Si/SiO₂ substrate.

2.3.2. Reduction of rGO

Conductivity of GO is quite low and it is not suitable to be directly applied as a FET channel. A high resistance FET channel decreases signal (current) and the signal-to-noise ratio is relatively low (Dong et al., 2011). To improve the

conductivity of a GO film, GO is usually reduced to rGO before being used as a semiconductor channel. A successful reduction process greatly enhances the conductivity of GO. The conductivity of rGO reported in literatures was about 5 orders of magnitude higher than GO (Stankovich et al., 2007).

In order to characterize the successfulness of hydrazine reduction of GO, GO and rGO reduced by hydrazine was investigated by Raman spectroscopy. Raman spectroscopy is a very handy approach for investigating oxidation degree of graphene. In the Raman spectrum of GO and rGO, two peaks are usually studied: a.) G band at approximately 1575 cm^{-1} and b.) D band at approximately 1355 cm^{-1} (Kudin et al., 2008). Intensity of G band corresponds to the intact carbon lattice in graphene while D band corresponds to the edge and defect in carbon lattice.

In Raman spectrum of GO and rGO presents in figure 2.3.2.1. a, a typical pair of well defined D and G bands can be observed. In order to quantitatively study the Raman spectrum, I_D/I_G was used as the indicator. I_D/I_G was calculated by dividing intensity of D band with the intensity of G band. I_D/I_G of GO film was calculated to be 0.89 and the I_D/I_G of rGO increased to 1.20. After hydrazine reduction, relative intensity of D band increased and the one of G band decreased. After the

reduction process, carbon edge atoms in the honeycomb structure restored. Increase of graphene edge increased the relative intensity of D band. This observation preliminarily proved the reduction process was successful.

In order to optimize the reduction process, time lapsed study of hydrazine reduction was preformed. In figure 2.3.2.1. b, rGO film reduced for different time (0 hr, 0.25 hr, 0.5 hr, 1 hr, 2 hr and 4 hr) was studied under Raman spectroscopy and the corresponding I_D/I_G was calculated. As presents in figure 2.3.2.2. b, I_D/I_G gradually increased with the time of rGO spent in hydrazine vapor reduction. The increment was large at first 0.5 hr and the trend finally stabilized after 2 hr. After 4 hr of reduction, I_D/I_G of rGO did not varied from the previous sample (2 hr) very much. It is possible that the reduction process was completed at around 2 hr and further incubate rGO in hydrazine vapor did not lead to any increase of I_D/I_G . Although it was found that 2 hr is long enough to reduce rGO in hydrazine vapor, in order to ensure rGO was fully reduced, hydrazine reduction of GO carried out in the rest of this project was performed overnight.

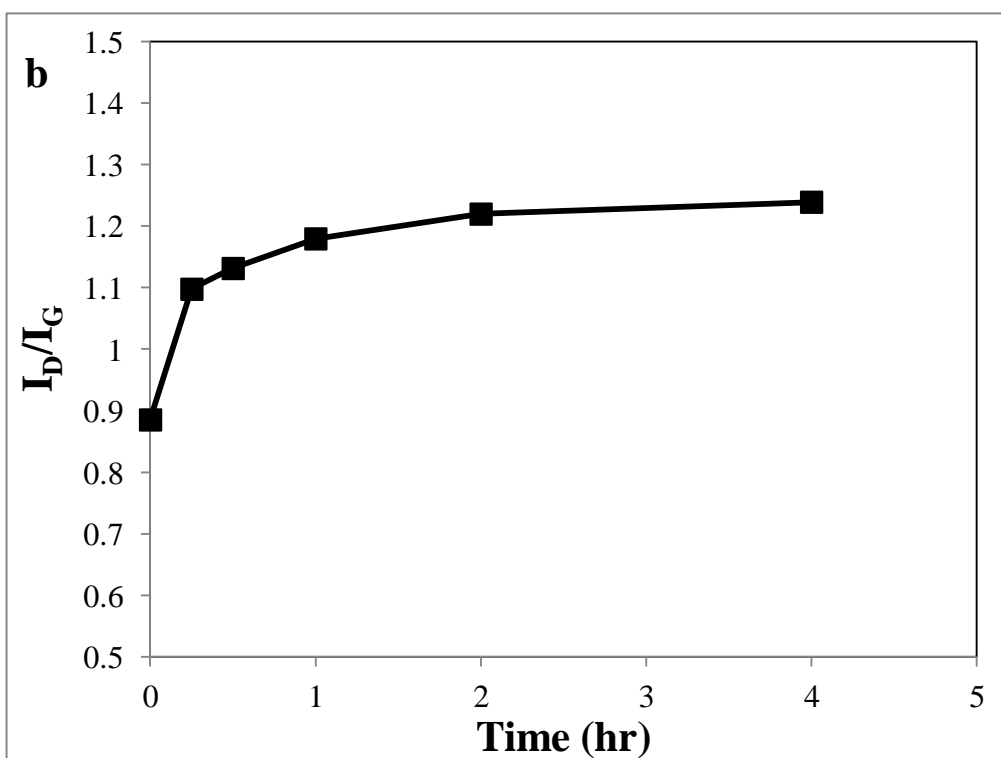
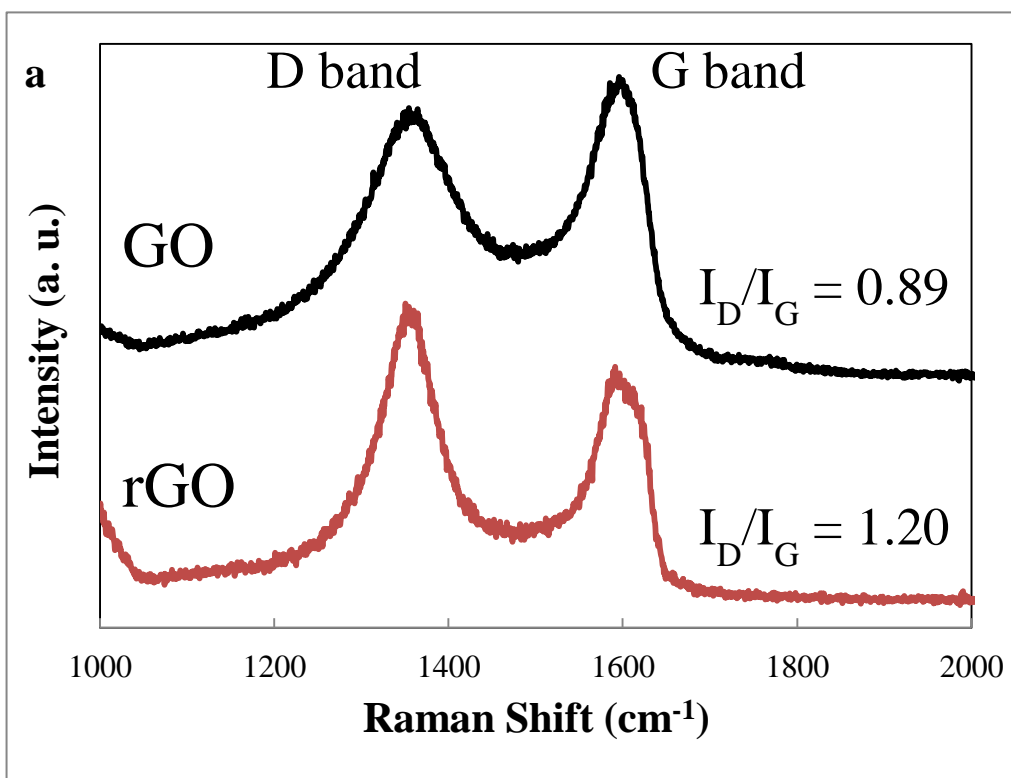
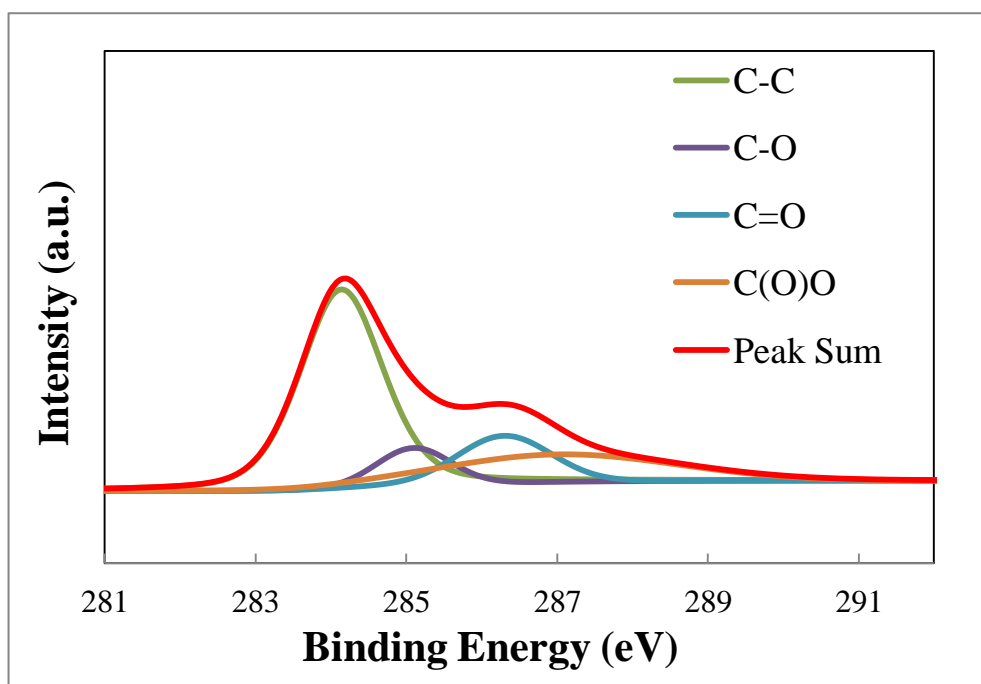
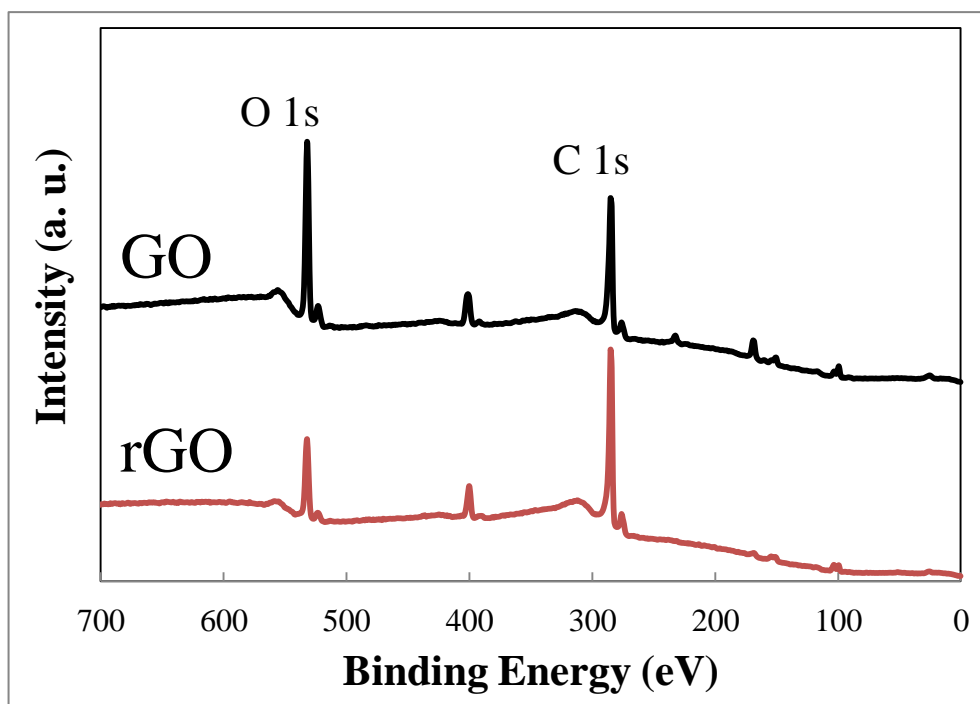


Figure. 2.3.2.1. (a) Raman spectroscopy of GO film and rGO film after hydrazine reduction and (b) time lapsed study of I_D/I_G after different hydrazine reduction time.

Raman spectroscopy presented previously provided an overview of the reduction process. In order to further investigate the chemical composition of rGO along the reduction process, XPS was performed. Figure 2.3.2.2. a shows XPS wide scan of GO and rGO. In GO, oxygen content was found to be very abundant. After reduction, the relative intensity of oxygen recorded by XPS spectrometer decreased drastically. The removal of oxygen during reduction of hydrazine should be the major reason corresponded to the O 1s decrement in XPS spectrum. Details chemical composition of GO and rGO were elaborated by studying their C 1s spectrum. As shows in figure 2.3.2.2. b, C 1s scan of GO composed of various components including C-C, C-O, C=O and C(O)O. These bonding represented various functional groups and bonding in GO, including graphene lattice, hydroxyl and epoxy group, aldehyde group and carboxyl group correspondingly. After reduction, relative intensity of C-C and C-O increased while the others decreased. It may be due to the fact that carboxyl group and aldehyde group are reduced in higher priority, which finally transformed into hydroxyl group or even recovered to C-C bonding. The recovery of C-C bonding indicated the defect in rGO was being removed and the carbon lattice was “healed” after hydrazine reduction. The recovery of carbon lattice and removal of defect enhanced the conductivity of rGO, making it a better candidate in FET biosensing.



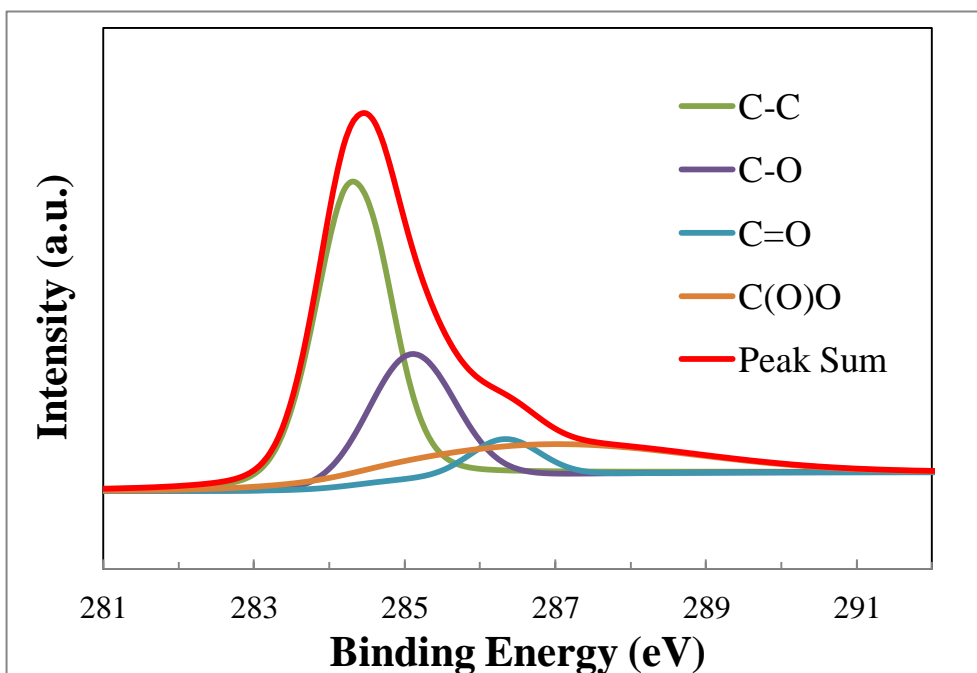


Figure. 2.3.2.2. (a) XPS wide scan of GO and rGO after hydrazine vapor reduction. (b) C 1s scan of GO and (c) rGO.

2.3.3. Fluorescence study of different probe stability on rGO

To study stability of DNA capture probe on rGO assembled by π - π stacking with different length, fluorescence-labeled long capture probe and fluorescence-labeled short capture probe were used. Both probes were modified with Cy3 fluorescence tags at 3' end. Detachment of capture probe generate fluorescence signal in the analyte that can be observed by a fluorescence plate reader.

Firstly, fluorescence-labeled long capture probe and fluorescence-labeled short

capture probe were self-assembled on rGO via π - π stacking by incubating the corresponding capture probe containing solution with rGO film. Afterward, the rGO film was washed thoroughly to remove excess probe. Thereafter, rGO functionalized with fluorescence-labeled long capture probe and fluorescence-labeled short capture probe were further incubated with cDNA or non-cDNA. In short, there are four combinations of samples, which are: fluorescence-labeled short capture probe + cDNA, fluorescence-labeled short capture probe + non-cDNA, fluorescence-labeled long capture probe + cDNA and fluorescence-labeled long capture probe + non-cDNA. After incubation with rGO substrate, analyte were collected and the fluorescence intensity of analyte in each condition was studied off-chip by a fluorescence plate reader. Any fluorescence signal measured could be an indicator of probe detachment. Higher fluorescence intensity could be interpreted as lower probe stability.

Empirical result of the captioned experiment presents in figure 2.3.3. In figure 2.3.3., it can be observed that when non-cDNA was introduced, there were limited fluorescence signal obtained from both the fluorescence-labeled long capture probe and fluorescence-labeled short capture probe-modified samples. Non-cDNA was not complementary with any capture probes thus the addition of

it did not hybridization with any of the capture probe. Capture probe remained single-stranded and the π - π stacking interaction was not interrupted. Moreover, the limited fluorescence signal suggested the addition of non-cDNA did not result in observable non-specific displacement of capture probe. It is very important for the pre-adsorbed capture probe to stay tightly bond to rGO substrate when non-target oligonucleotide exist in analyte in order to maintain the sensor's reliability.

In the case of fluorescence-labeled long capture probe + cDNA, a low fluorescence signal was also observed. cDNA only hybridized with half of the fluorescence-labeled long capture probe and the extended part in capture probe remained as single-strand. Although the hybridized portion formed double-helix structure disrupted π - π stacking attraction force with graphene, the extended single-strand structure of fluorescence-labeled long capture probe maintained the π - π interaction between fluorescence-labeled long capture probe-cDNA complex and rGO substrate. The partially hybridized fluorescence-labeled long capture probe-cDNA complex was thus confined on the surface of rGO firmly even after hybridization. The extended long capture probe provided good affinity with rGO and the probe immobilization was merely affected after target hybridization.

When the fluorescence-labeled short capture probe functionalized rGO was incubated with cDNA, the highest fluorescence signal was recorded among all conditions. Introduction of fully complementary cDNA turned fluorescence-labeled short capture probe into dsDNA after hybridization. Nucleobases were shielded in the double-helix structure of dsDNA and the π - π stacking force was weakened. Weakening of π - π interaction force liberated the dsDNA from rGO surface and increased fluorescence signal observed in the analyte. The relatively high fluorescence signal observed in this experiment suggested that the fully hybridized fluorescence-labeled short capture probe-cDNA dsDNA complex is not tightly adhered on rGO and gentle washing liberated it from immobilized state into the solution phase. This observation generally concurred with previous findings when a similar condition was conducted in aqueous phase experiment (Lu et al., 2009).

This fluorescence study has proven long capture probe to be a relatively stable capture probe for capturing cDNA on rGO surface when probes were assembled on rGO via π - π interaction. A stable immobilization scheme is critical for developing a reliable FET biosensor. Detachment of fluorescence-labeled short

capture probe-cDNA dsDNA decreased the cDNA capturing ability of short capture probe. When cDNA was captured on the proximity of rGO, charge density on rGO surface was increased, however, detachment of dsDNA complex countered this effect. If short capture probe is used as capturing probe in a graphene-based bioFET, its instability may hamper the sensing performance.

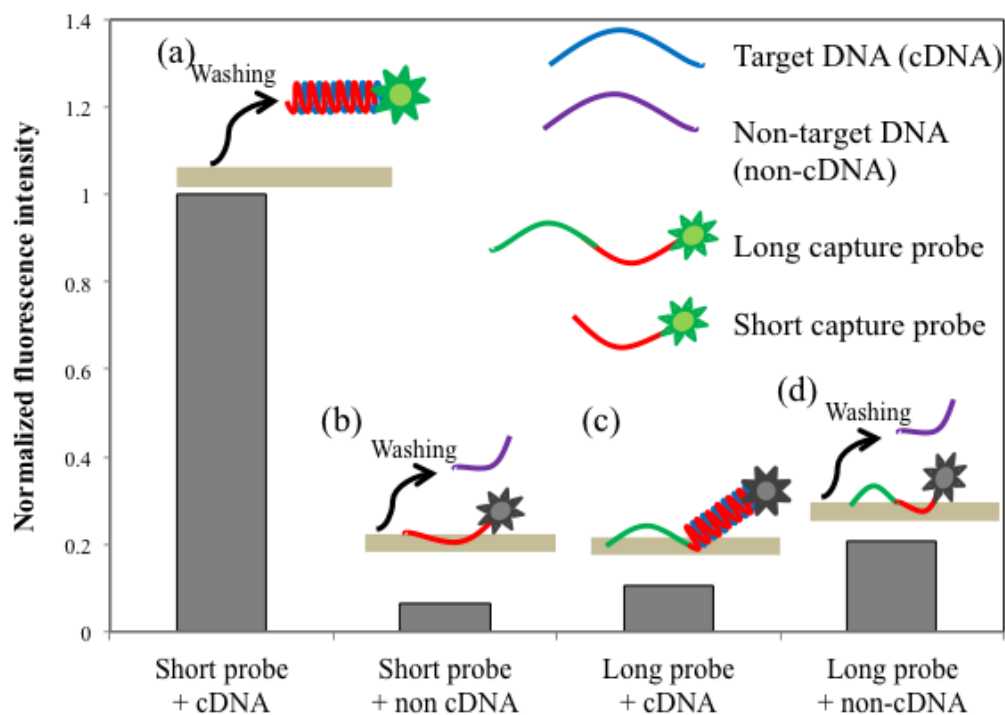


Figure 2.3.3 Fluorescence signals of removed samples in the washing environment for four cases of (a) fluorescence-labeled short capture probe + cDNA, (b) fluorescence-labeled short capture probe + non-cDNA, (c) fluorescence-labeled long capture probe + cDNA, and (d) fluorescence-labeled long capture probe + non-cDNA. Here, the fluorescence signal obtained from fluorescence-labeled short capture probe + cDNA was used as reference.

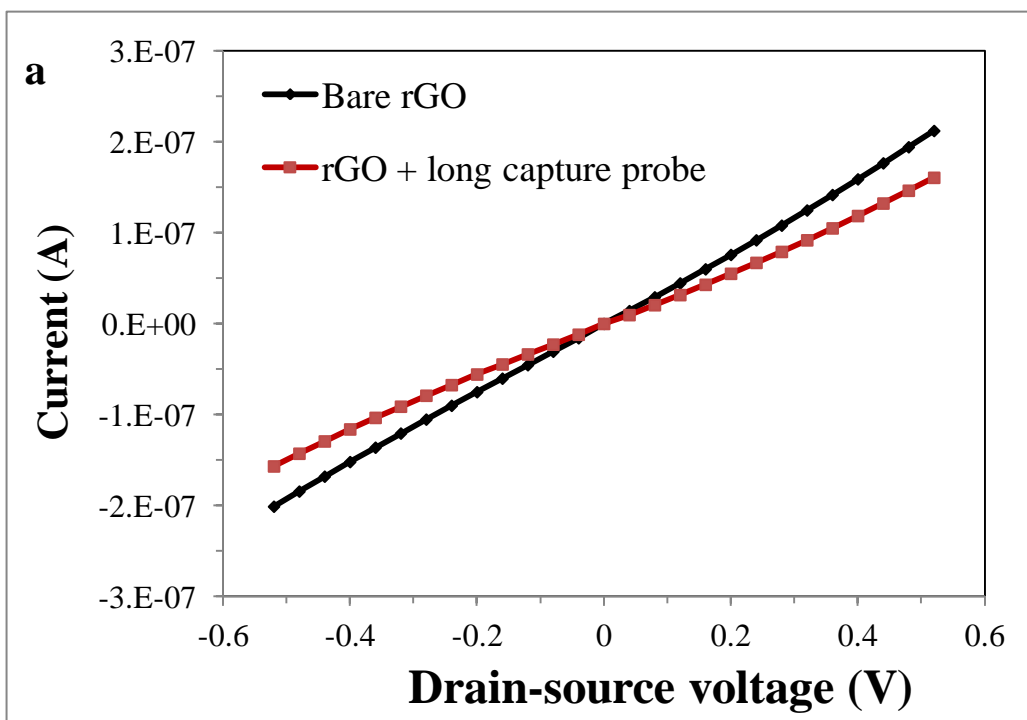
2.3.4. Functionalizing rGO FET with long capture probe

To investigate the effect of DNA capture probe adsorption on the electrical property of rGO FET channel, current response under the application of various drain-source voltage (V_{DS}) were recorded and the results were plotted into I-V curves. Firstly, I-V curve of bare rGO channel was obtained by scanning from -0.5 V to 0.5 V. As shows in figure 2.3.4. a, Ohmic region, or linear region, was observed when the bare rGO FET channel was scanned in the range of -0.5 V to 0.5 V V_{DS} . When rGO was functionalized with long capture probe, slope of the I-V curve decreased when compared with the one of bare rGO. Slope decrement in I-V plot indicated a conductance decrease of the FET channel after long capture probe immobilization. This observation agreed with previous studies in literature that DNA adsorption on rGO thin film led to n-doping effect to decrease rGO conductance (Dong et al., 2010, stine et al., 2010). When rGO was operated with no V_G applied, it is well known that rGO should be working in p-type region. When DNA was attached on the surface of rGO, it was hypothesized that DNA induced n-doping effect to rGO, which decreased the major carrier (hole) concentration and hence the conductance of rGO decreased (Karimi et al., 2014). The decrease of conductance also suggested that long capture probe was

immobilized and brought to the proximity on rGO surface.

After I-V curve of bare rGO and long capture probe functionalized rGO was measured, real-time current measurement of a bare rGO incubated with different concentration of long capture probe was performed. The goal of this experiment was to explore the concentration of long capture probe needed to saturate the surface of rGO. In order to fabricate a reliable rGO-based DNA biosensor, it is important to ensure rGO surface is saturated with capture probe. A saturated surface can prevent non-specific adsorption of other non-specific DNA on rGO surface since the pre-adsorbed probe provides electrostatic repulsion force to repel them. In figure 2.3.4. b, bare rGO channel had a quite stable conductivity before long capture probe was injected. After 10 nM of long capture probe was injected into PDMS reservoir, relative conductance of rGO dropped drastically. Similar events happened when concentration of long capture probe increased to 50 nM and 100 nM. This observation in real-time current measurement concurred with the results obtained from I-V curves measurement. Conductance decrement of rGO should be attributed to the adsorption of long capture probe onto rGO surface. When the concentration of long capture probe increased to 1 μ M, relative conductance of rGO was barely changed. 100 nM long capture probe should be

enough to saturate the surface of rGO channel while further increasing long capture probe concentration did not lead to any more adsorption of long capture probe onto rGO surface. Long capture probe density on the saturated rGO reached maximum and further adding long capture probe in the analyte cannot change the conductivity of rGO. A short conclusion can be drawn from this experiment that 1 μM of long capture probe was enough to fully functionalize the rGO device fabricated in this project. In order to ensure the rGO FET channel surface was fully saturated, they were incubated with 10 μM long capture probe for four hours.



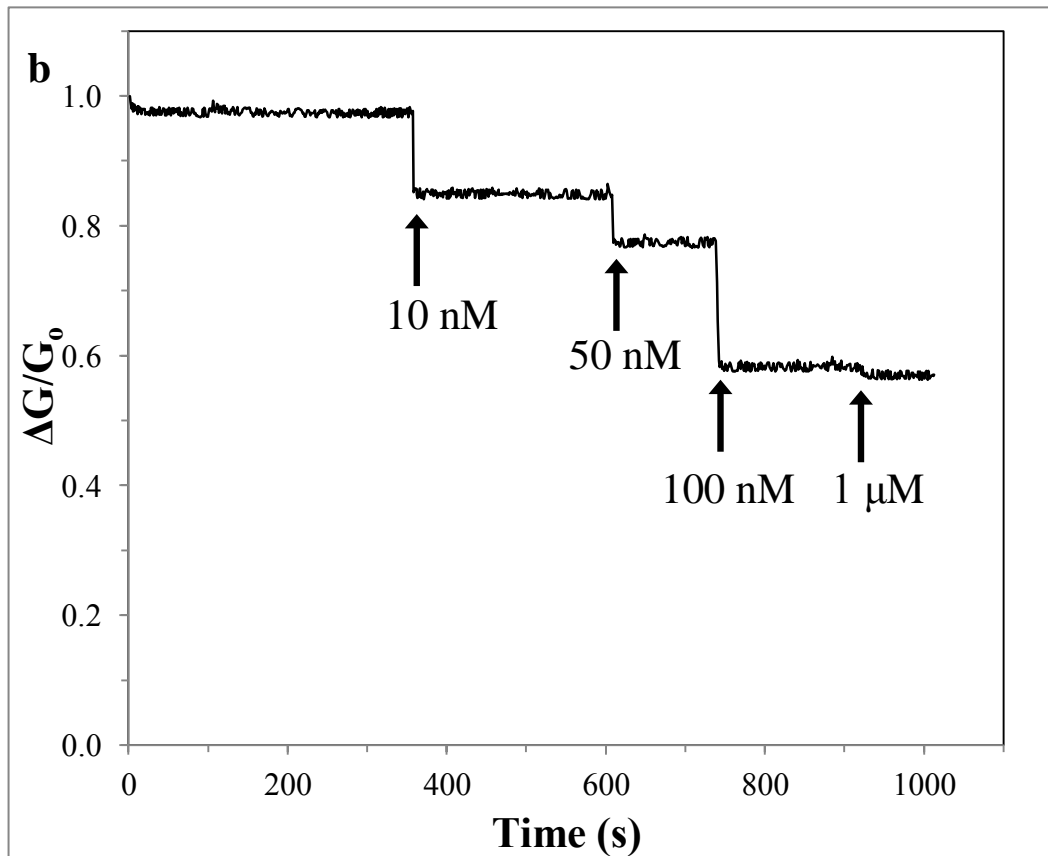


Figure 2.3.4. (a) I-V curves of bare rGO and rGO functionalized with long capture probe. (b) Real-time current measurement of rGO FET when different concentrations of long capture probe (10 nM, 50 nM, 100 nM and 1 μ M) were injected into PDMS reservoir ($V_{DS} = 0.4$ V).

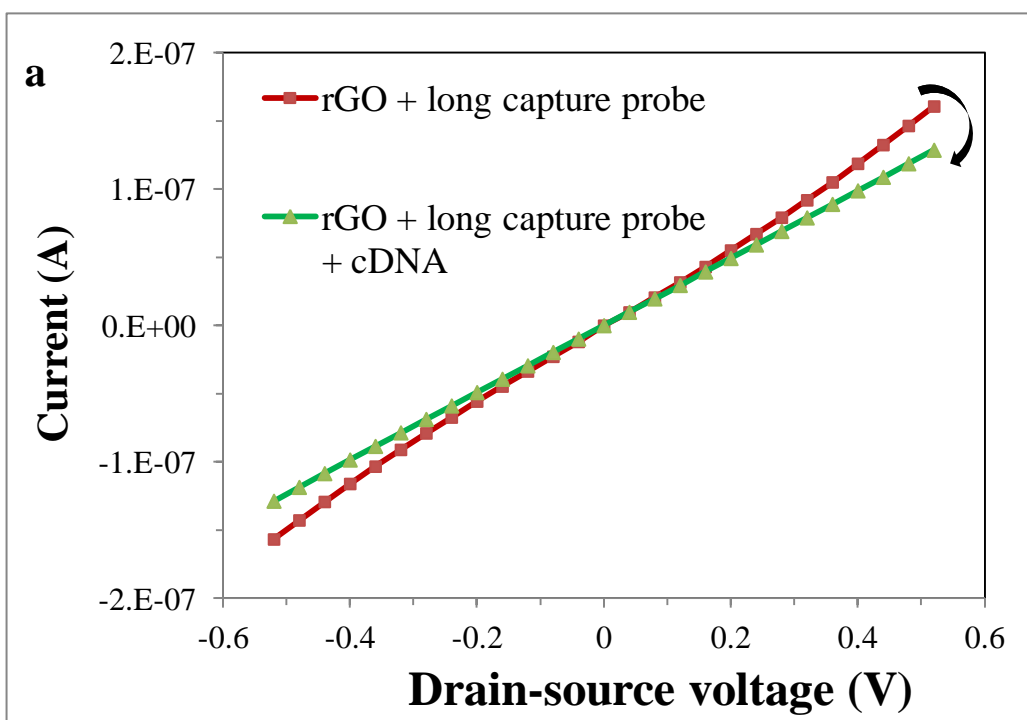
2.3.5. rGO FET with long capture probe for target detection

After saturate rGO FET channel surface with long capture probe, the FET device was ready to be used as a bioFET in identifying target DNA. Long capture probe functionalized rGO bioFET was incubated with cDNA and non-cDNA respectively. Their I-V curves were measured before and after sample incubation.

In figure 2.3.5. a, slope of I-V curve of the rGO biosensor decreased obviously after cDNA incubation. The slope decrement of I-V curve indicated the resistance of rGO biosensor increased after exposing to cDNA. This phenomenon was similar to the one when bare rGO was functionalized with long capture probe. When cDNA was introduced to the rGO biosensor, it hybridized with the complementary sequence of long capture probe. After hybridization, half of the long capture probe hybridized with cDNA and turned into a double-stranded structure, while the other half remained single-stranded and π - π stacked with rGO. Presence of cDNA eventually increased the total number of DNA on the surface of rGO and hence increased charge density on the proximity of rGO. N-doping effect posed by DNA was further increased when DNA density increased, which decreased the conductance of rGO.

When non-cDNA was introduced, conductance of rGO decreased slightly only. Unlike cDNA, non-cDNA did not have any sequence complementary to long capture probe. Non-cDNA could not be captured by long capture probe nor be non-specifically adsorbed on rGO, which the electrostatic repulsion force of long capture probe repelled non-cDNA from rGO surface. Non-cDNA cannot be captured on the rGO and it was removed in washing step. The slight decrement

of rGO conductance suggested that non-specific adsorption of non-cDNA was minimal. All in all, the rGO FET biosensor functionalized with long capture probe was demonstrated to be able to discriminate target cDNA from non-target non-cDNA by monitoring conductance of rGO.



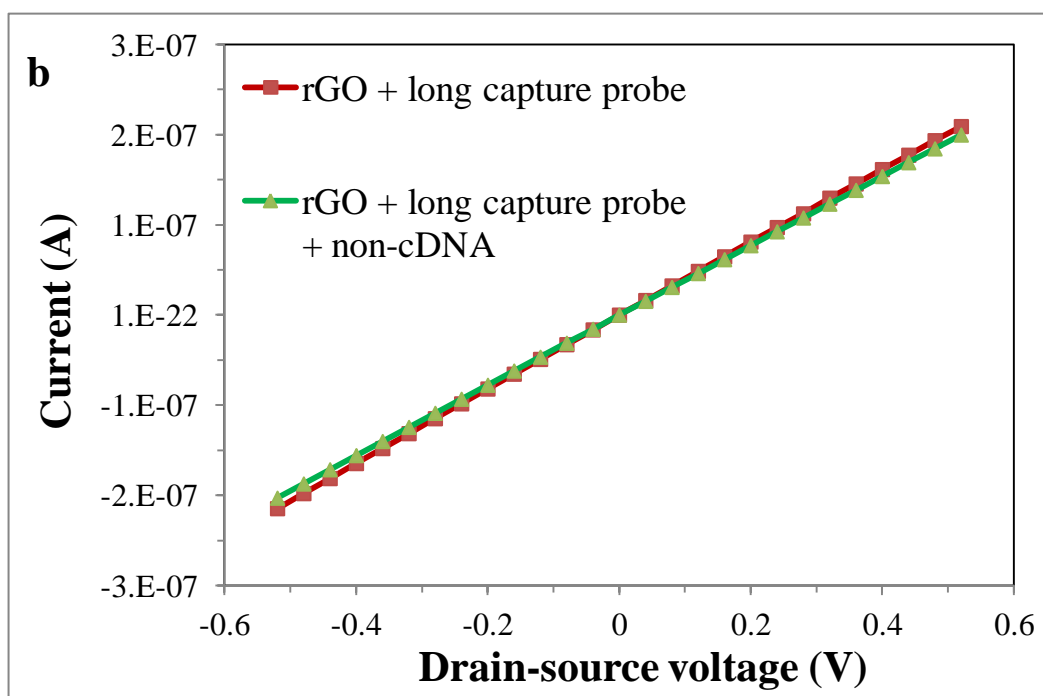


Figure 2.3.5. I-V curves of long capture probe functionalized rGO, (a) after exposed to cDNA and (b) after exposure to non-cDNA.

2.3.6. Real-time detection of cDNA target using long capture probe

Although this rGO FET biosensor was demonstrated to be able to discriminate between cDNA and non-cDNA, it was also important to provide quantitative analysis on the biosensor's performance. To further study the sensor's performance, conductance of rGO FET was continuously monitored along a period of time when difference concentration of cDNA and non-cDNA was injected to the PDMS reservoir in order to study the response time, sensitivity,

LOD and specificity of the long capture probe functionalized rGO FET biosensor.

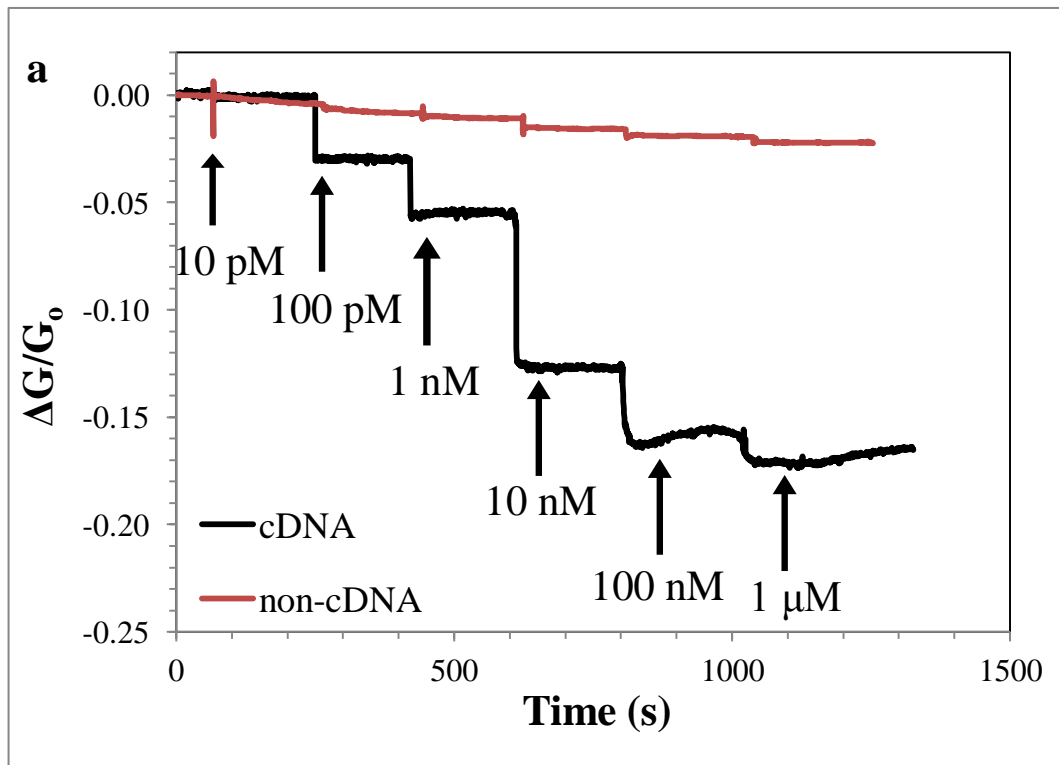
Figure 2.3.6. a shows the real-time measurement of rGO relative conductance ($\Delta G/G_0$) when different concentration (from 10 pM to 1 μ M) of cDNA or non-cDNA was introduced to the rGO FET. When cDNA was introduced to rGO FET, a rapid drop of $\Delta G/G_0$ was observed. The rGO FET biosensor responded almost immediately to the addition of target containing analyte, which suggested the long capture probe functionalized rGO-based bioFET has a short responding time (tens of seconds). When the concentration of cDNA was down to 10 pM, the change in $\Delta G/G_0$ was almost un-noticeable. However, when the concentration increased from 10 pM to 100 pM, the $\Delta G/G_0$ became noticeable and the $\Delta G/G_0$ further decreased until concentration of cDNA increased to 1 μ M. When 1 μ M cDNA was introduced to the rGO FET biosensor, an immediate drop of $\Delta G/G_0$ was also recorded, however, after the signal was stabilized, the $\Delta G/G_0$ did not vary from the signal obtained when the rGO FET was exposed to 100 nM cDNA. It was possible that long capture probe immobilized on the surface of rGO was already saturated by 100 nM cDNA. Further increasing cDNA concentration did not lead to more cDNA to be captured on the proximity of rGO, which did not result in any

increment of sensing signal. The saturation of detection signal is probably caused by the saturation of capture probe immobilized on the proximity of graphene. In figure 2.3.4. b, the rGO FET channel was found to be saturated by approximately 100 nM long capture probe. It is reasonable to deduce that by having slightly more than 100 nM cDNA, all of the long capture probes on graphene were saturated and further increasing cDNA concentration did not increase the number of cDNA being captured on rGO surface, leading to a $\Delta G/G_0$ saturation. Besides the rapid detection of cDNA by our rGO FET, our rGO FET biosensor also has the ability to discriminate non-cDNA from cDNA. When non-cDNA was introduced, there were very limited changes in $\Delta G/G_0$ even the concentration of non-cDNA was as high as 1 μM . The maximum response when cDNA was introduced -0.18 while the maximum response recorded from addition of non-cDNA was -0.02 (figure 2.3.6. b). Non-cDNA did not have the ability to hybridize with long capture probe and the only way of non-cDNA to interfere with the rGO FET platform is passive adsorption. Long capture probe has a relative long oligonucleotide sequence (48 base pairs) while the length of non-cDNA was relatively short (18 base pairs). It is possible that long capture probe was not able to saturate the surface of rGO, leaving certain vacancy after long capture probe functionalization that only short DNA sequence may fit in. The relatively short non-cDNA stands could fill-up

those vacancy leading to passive adsorption and a slight decrease of $\Delta G/G_0$. After all, the signal recorded from the addition of non-cDNA was minimal even the concentration of it was extremely high (up to 1 μM). Such changes were so small that it fell in the noise regime and did not affect the overall sensing performance. Although single base mismatch target was not experimented in this chapter, the CVD graphene bioFET presents in the next chapter was found to be able to distinguish fully complementary target from the single base mismatched one. It is reasonable to generalize that result and to believe that our rGO bioFET presents in this chapter is able to perform single base mismatch differentiation, suggesting good specificity of graphene-based bioFET DNA sensor.

LOD of our rGO FET biosensor functionalized with long capture probe shows in figure 2.3.6. c by plotting $\Delta G/G_0$ against cDNA concentration. The sensor response correlated linearly with the logarithmic of cDNA concentration, which was similar to other reports studying graphene-based DNA bioFET (Stine et al., 2010, Dong et al., 2010, Yin et al., 2012, Chen et al., 2013, Lin et al., 2013, Cai et al., 2014). Linear regression of the relationship between sensing signal and target concentration was $\Delta G/G_0 = -0.0258\ln[\text{cDNA}] - 0.6021$. The correlation between $\Delta G/G_0$ and cDNA concentration was good with $R^2 = 0.97$. Dynamic range of this long capture probe-functionalized rGO FET biosensor was wide and it ranged

from 250 pM to 100 nM. Noise of the biosensor was recorded by calculating $\Delta G/G_0$ after injection of blank buffer into sample reservoir. This experiment was repeated for five times and the final noise level was calculated by summing the mean of those trials and three times of the standard deviation, which was -0.04. Detection limit of this long capture probe functionalized rGO-based bioFET was calculated to be approximately 300 pM.



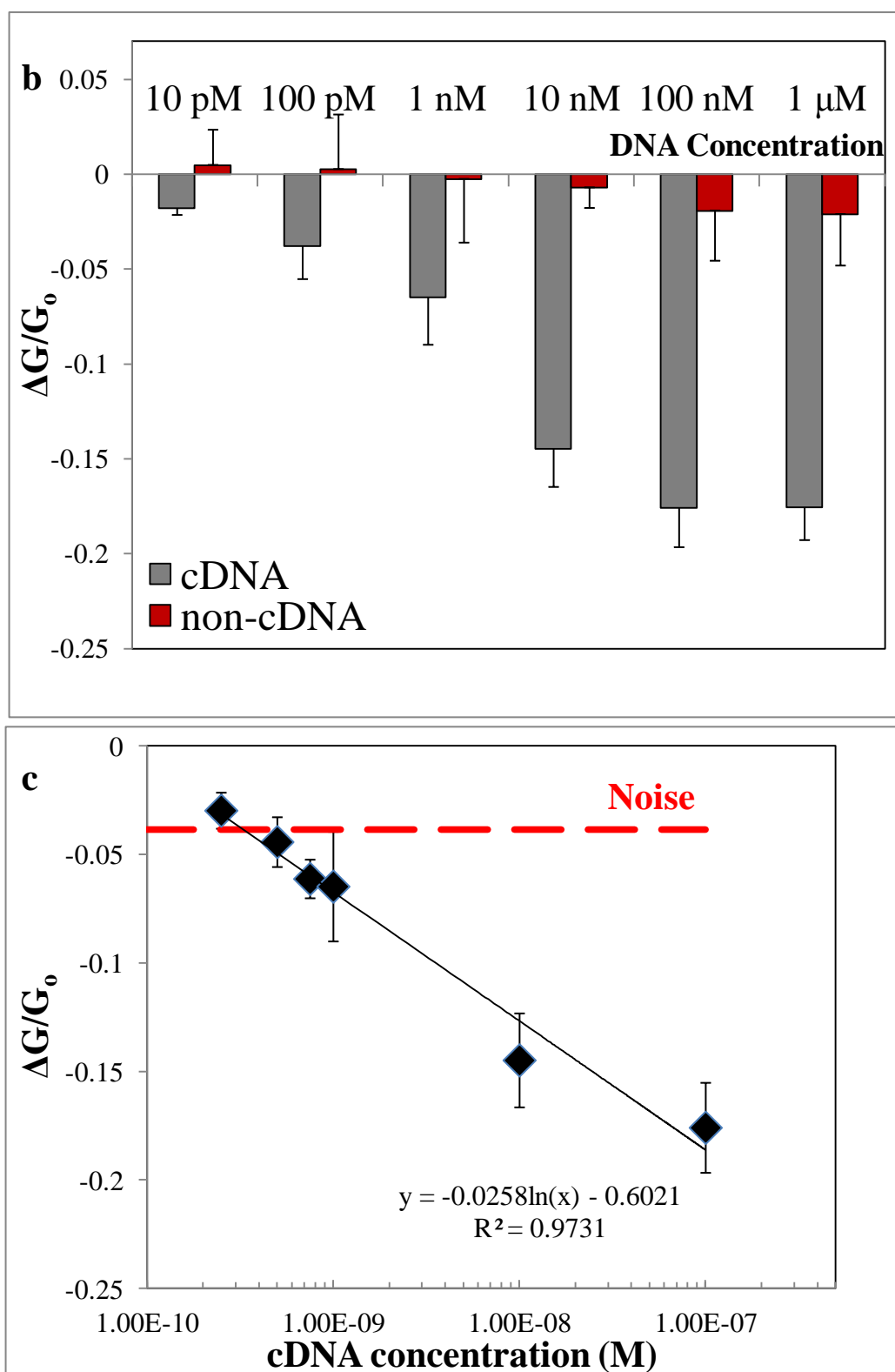


Figure 2.3.6. (a) Real-time measurement of conductance change of rGO FET biosensor functionalized with long capture probe upon exposure to various concentration (10 pM, 100 pM, 1 nM, 10 nM, 100 nM and 1 μ M) of cDNA and non-cDNA and (b) sensing signal ($\Delta G/G_0$) plot against concentration of DNA. (c) $\Delta G/G_0$ plot against the logarithmic concentration of cDNA. Noise level was

established by introducing blank buffer solution to the rGO FET channel. Statistical data was obtained from three individual devices.

2.3.7. Comparing rGO FET biosensor performance with different probe immobilization strategies

Through the past decades, there are numerous reports regarding graphene-based biosensor. Research focus of those reports included using various methods to fabricate and transfer graphene, modifying the FET channel into different structures or with different nano-materials, detecting different analytical targets, etc. However, how does different DNA capture probe immobilization methods affect bioFET performance is rarely studied. In this project, we compared the biosensing performance of rGO bioFET with three different probe immobilization methods: a.) covalent immobilization of amine-modified short capture probe with linker molecules, b.) π - π stacking fully complementary short capture probe and c.) π - π stacking partially complementary long capture probe. The first two approaches were widely adopted in previous researches while the final one has not been reported in FET biosensor yet. All these immobilization methods create barely any damage to graphene carbon lattice in rGO, maintaining the electrical property of rGO undamaged. PA is a widely used bifunctional linker molecule in graphene

biosensing. The pyrene-end binds strongly to the basal plane of graphene via π - π stacking interaction and the high carrier mobility in graphene can be preserved (Georgakilas et al., 2012, Pembroke et al., 2013). The carboxylate end of PA provides a facile tool for subsequent covalent attachment of biomolecules through well-established chemical rout, for example, the well-known EDC/NHS chemistry. To achieve covalent attachment of amine-modified short capture probe on rGO surface, PA was firstly linked with rGO surface via π - π stacking interaction. Amine-modified short capture probe was then covalently immobilized on rGO using EDC/NHS method. Functionalizing rGO short capture probe and long capture probe were achieved by π - π stacking and the operation procedure contained simply an incubating step and a washing step.

Relative conductance change of rGO transistors of rGO FET biosensor with different probe immobilization methods at different cDNA concentration shows in figure 2.3.7. Obviously, rGO transistors modified with long capture probe demonstrated the largest conductance change compared with those with short capture probe and PA linker. When target cDNA hybridized with long capture probe, they were brought to the very proximity of rGO surface leading to decrease of conductance by the n-doping effect. Although the PA/ amine-modified short

capture probe also has the ability to capture cDNA, distance between captured cDNA and rGO surface via PA linker immobilization was larger than the one captured by long capture probe. It was because the PA linker acted similar to a spacer that separated cDNA further from the surface of rGO. Since FET biosensor responses to the charge of biomolecules, separating target molecules further from the proximity of FET channel decreased the electric field of that biomolecule exerts on the FET channel, finally leads to lower sensor sensitivity. When rGO was functionalized with short capture probe, the corresponding sensitivity was better than the one using PA linker but still not comparable to the FET device functionalized with long capture probe. It is well known that when a π - π stacked DNA on a graphene-based material surface fully hybridized with the complementary target, the formation of double helix structure shielded the nucleobases from forming π - π stacking. The formed double-stranded structure losses their ability to π - π stack with graphene and the hybridized DNA tends to detach from the surface of graphene (Huang et al., 2012, Lu et al., 2009 and Liu et al., 2011). This assumption was testified in this chapter by fluorescence microscopy. Detachment of short capture probe-cDNA complex partially reversed the target capturing effect of probe DNA, which decreased the overall n-doping effect created. The short capture probe functionalized rGO-based bioFET is a less

reliable biosensor with lesser sensitivity.

The above experiment demonstrated long capture probe was the best choice of probe immobilization methods among those three we opted. Functionalizing with long capture probe has several advantages. First of all, using long capture probe omitted the need of bifunctional linker spacer between cDNA and the proximity of rGO, which brought the target closer to the graphene proximity and it is crucial to sensor sensitivity. Secondly, after hybridization, the extended section of long capture probe remained single stranded. The single stranded portion retained the ability to π - π stack with rGO, preventing the long capture probe-cDNA complex from detach. The short distance between target and FET channel together with the good stability of the hybridized long capture probe both contributed to the excellent performance of the rGO functionalized with long capture probe.

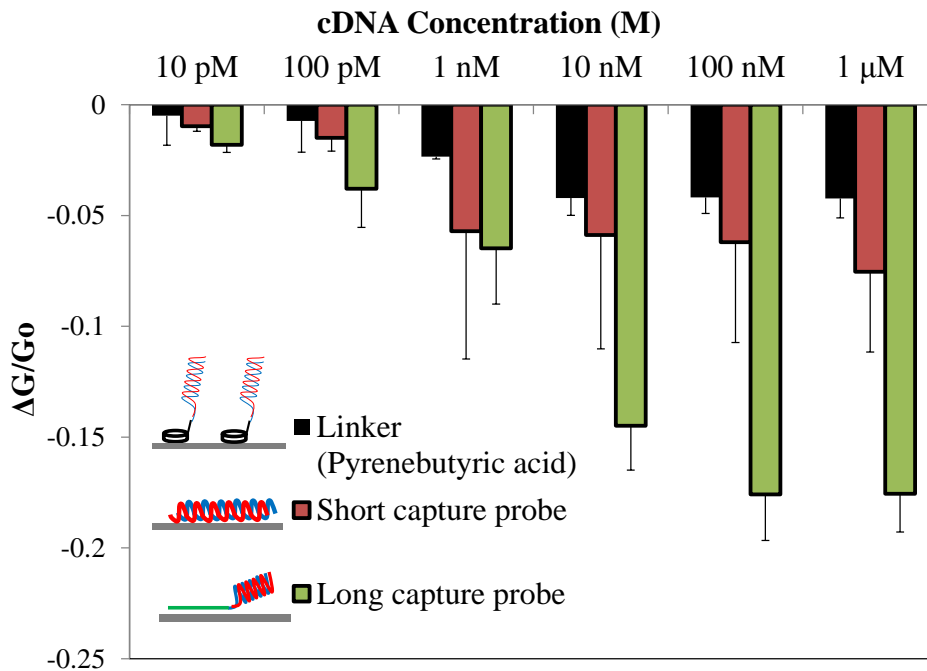


Figure 2.3.7. Histogram comparing rGO FET biosensor response with different probe immobilization methods when exposed to different concentration of cDNA. Probe immobilization methods investigated included covalent immobilization amine-modified short capture probe with PA, π - π stacking with short capture probe or long capture probe.

2.4. Summary

In summary, hydrazine reduction of rGO was first characterized and optimized by Raman spectroscopy and XPS. Morphology of the rGO channel was visualized by AFM. Long capture probe was found to be providing n-doping effect on rGO, which decreased the conductance of rGO transistor. Long capture probe with reasonably high concentration was used to functionalize rGO and the surface saturation of rGO surface was ensured.

After the fabrication process of rGO FET biosensor was verified and optimized, the capability of using long capture probe to detect target cDNA was investigated. By the I-V curves and real-time measurement, specificity of the biosensor was verified and the sensor was found to be working in a wide dynamic range with relatively low detection limit.

Finally, performance of rGO FET biosensor functionalized with three different DNA capturing probe immobilization strategies (short capture probe, long capture probe and amine-modified short capture probe using bifunctional linker) were compared. Tendency of probe detachment after hybridization were found in short capture probe but not long capture probe, which was confirmed by fluorescence microscopy. In real-time detection of cDNA, long capture probe outperformed the other two strategies by giving the best sensitivity and lowest LOD.

Chapter 3 Chemical Vapor Deposition Grown Graphene DNA Field-Effect Transistor Biosensor with Gold Nanoparticles Signal Amplification

3.1. Introduction

Avian influenza A H7N9 was a virus originally adapted to birds only before 2013. In March 2013, three incidents of human infection of H7N9 were found in Shanghai and Anhui, China (Gao et al., 2013). Two of the three patients passed away in March 2013 and the other died in April 2013. The severe infection of H7N9 with extremely high mortality rate posts a potential threat to human population (Hvistendahl et al., 2013). As suggested by World Health Organization (WHO), quantitative reverse-transcriptase polymerase chain reaction (qRT-PCR) is the gold standard for H7N9 detection. Although qRT-PCR is a very sensitive detection method and precise quantitative analysis can be provided, it requires expensive apparatus and well-trained technicians to perform the test in a laboratory environment (Hoffmann et al., 2007, Monne et al., 2008). The on-site application of qRT-PCR for detection of H7N9 is thus hampered by these disadvantages. There is an urgent need to develop other simple, low-cost, sensitive

and portable biosensor devices to detect oligonucleotide genes of H7N9 in order to screen the large amount of poultry and patients with H7N9 flu-like symptoms.

To detect viral oligonucleotide genes, bioFET is a very powerful tool. BioFET provides a label free, sensitive, quickly responding, multiplex and point-of-care detection platform for analyzing biomolecules. Performance of a bioFET highly depends on the semiconducting channel. Graphene, a 2D material consists of only one layer of carbon atoms arranged in honeycomb shaped lattice appeared as a perfect candidate in bioFET (Novoselov et al., 2004). The ultra-thin structure, intrinsic semi-conducting properties, high electron mobility, strong physical properties and high stability at ambient environment of graphene drew numerous researchers' attention for applying this amazing material in the field of biosensing (Lu et al., 2009, Ohno et al., 2010, Huang et al., 2010, Kuila et al., 2011). rGO, as the reduced form of GO, has been used in graphene FET (GFET) biosensing due to its richness in functional groups and we've developed a rGO-based FET biosensor in the previous chapter (Stine et al., 2010, Yin et al., 2012, Cai et al., 2014). Although reducing GO to rGO partially recovers the excellent electronic properties of graphene, high quality graphene fabricated through CVD still out-perform rGO. Attempts of using CVD-grown graphene in bioFET for DNA

detection have been reported recently with advantages of high conductivity and binding uniformity (Dong et al., 2010, Chen et al., 2013, Lin et al., 2013).

In this chapter, we report a CVD-grown graphene-based bioFET for avian influenza virus H7 subtype gene detection with signal amplification by reporter oligonucleotide probes conjugated AuNPs. Compared with other graphene bioFET, our device has two unique designs. Firstly, the capture probe has two sections, which directly assembled on graphene surface via π - π stacking interaction. One section of the capture probe is designed for π - π stacking immobilization and the other section has complementary sequence to capture target oligonucleotide. This capture probe design strategy could avoid the detachment of hybridized probes from graphene surface after the target hybridization. Moreover, the AuNPs conjugated with reporter oligonucleotide probe co-hybridize with target DNA, a sandwich assay bridged by target DNA will be formed. Charge density on the proximity of graphene can thus be enhanced and the analytical performance of this GFET biosensor can be improved. LOD of this GFET biosensor with reporter probe-AuNPs signal amplification is as low as sub-picomolar level for avian influenza virus H7 subtype gene detection with response time around 10-15 minutes.

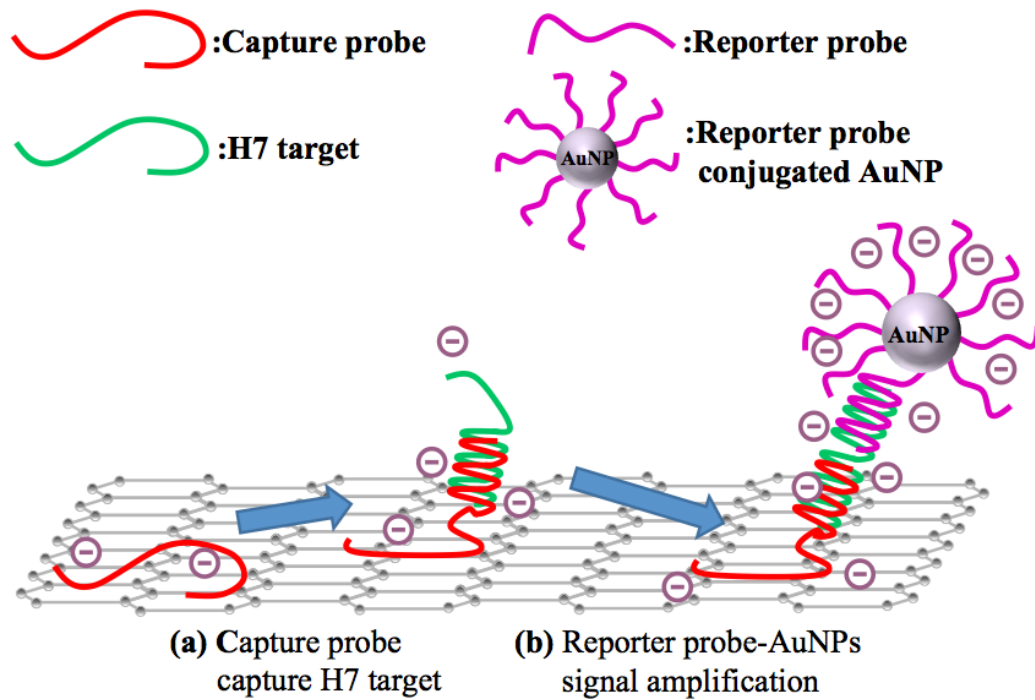


Figure 3.1.1. Schematic illustration of the proposed graphene bioFET sensing mechanism (a) capture probe captures target H7 DNA and (b) reporter probe-AuNPs amplifies sensing signal by enhancing charge density on the proximity of graphene.

3.2. Research methodology

3.2.1. Materials

Iron(III) nitrate nonahydrate, poly(methyl methacrylate) (PMMA, MW 996,000)

chlorobenzene, acetone, DL-dithiothreitol (DTT), 30 nm AuNPs, sodium chloride

(NaCl), potassium phosphate dibasic heptahydrate and potassium phosphate

monobasic monohydrate were purchased from Sigma-Aldrich, CVD graphene was bought from ACS Material. PBS 10X, pH 7.4) was purchased from Gibco. Silicon wafer (300 nm SiO₂ layer on Si) was purchased from MTI Corporation. Oligonucleotide was custom-made by Integrated DNA Technologies. Desalting gel columns (illustra MicroSpin G-25 Columns) were purchased from GE Healthcare.

The capture probe (5'-AAA AAA AAA AAA AAA CAT CTG CGG GAA-3'), reporter probe (5'-GCA GCA TTA TCT-SH-3'), complementary H7 hemagglutinin oligonucleotide target (5'-AGA TAA TGC TGC ATT CCC GCA GAT G-3'), a 25-bases fragment of influenza virus H7 gene sequence from an AIV isolate A/Hangzhou/1/2013 strain, genbank accession no. KC853766, non-target oligonucleotide (5'-AGA CAA TCC CCG ACC GAA TGA CCC A-3'), single-base mismatch target (5'-AGA TAA TGC TGC ATT CCA GCA GAT G-3'), double-bases mismatch (5'-AGA TAA TGC TGC ATT CCA CCA GAT G-3'), were synthesized by and purchased from Integrated DNA Technologies (IDT) Inc. (Coralville, IA, US).

3.2.2. CVD graphene transistor fabrication

Before CVD graphene transfer, two contact pads of Ti/Au for connecting source/drain electrodes was deposited on Si/SiO₂ wafer by magnetron sputtering.

A hard mask was used to pattern those source/drain contact pads. In the hard mask, there was two exposed area separated by 200 μm. After sputtering, metal contact pads were formed in the exposed area, on Si/SiO₂ wafer, separated by 100 μm and CVD graphene was later transferred on it.

CVD-grown graphene on copper foils was first transferred to silicon wafer following the protocol previously reported with slight modification (Suk et al., 2011). Briefly, CVD graphene on copper foil was first cut into small pieces and each piece will become a single FET device. Afterward, graphene grown on the backside of the copper foil was removed by plasma etching. PMMA dissolved in chlorobenzene (20 mg/ml) was then spin-coated on graphene and dried in air. The PMMA layer was estimated to be 50 nm thick. Subsequently, the CVD-grown graphene was suspended onto copper etchant (Iron(III) nitrate, 250 mg/ml). After the copper film was completely etched away, the PMMA/graphene membrane was gently transferred to DI water washing for three times. Finally, the

PMMA/graphene membrane was transferred to the surface of a Si/SiO₂ wafer. The PMMA/graphene/wafer substrate was dried in air and heated at 180 °C for 30 min. Finally, PMMA was dissolved with 55 °C hot acetone solution overnight. The as fabricated CVD graphene transistor was then washed with ethanol and DI water in sequence. The electrodes of the fabricated GFET were passivated by silicone rubber to create a reservoir with the gate area exposed.

3.2.3. Immobilization of capture probes on graphene

The fabricated GFET was firstly functionalized by immobilizing capture probe via π - π stacking interaction between nucleobases of DNA and graphene surface. Briefly, a 20 μ L solution of 10 μ M capture probe (in 1X PBS, pH 7.4) was added on the graphene channel and incubated overnight at room temperature. Afterwards, the loosely bonded DNA was removed by rinsing with 0.2% SDS in 1X PBS solution, 1X PBS solution and DI water sequentially for three times. Hybridization was performed by adding 20 μ L solution with H7 target probe in 1X PBS to the graphene channel. The hybridization time for each experiment was 2 hr. After hybridization was completed, the graphene channel was washed with 1X PBS containing 0.2% SDS, 1X PBS, and DI water in sequence for three times.

3.2.4. Conjugation of AuNPs with reporter probes for signal enhancement

AuNPs with the size of 15 nm were prepared using the previously reported method (Wong et al., 2012) while the 30 nm AuNPs were purchased commercially. The AuNPs were then conjugated with the reporter probe (5'-GCA GCA TTA TCT-SH-3') for signal enhancement correspondingly. Briefly, the thiol-modified reporter probe was first activated by DTT (0.1 M) in 1X PBS (pH 8.2) for 30 min. After activation, the solution was passed through a desalting column. The purified thiol-modified reporter DNA (2 μ M) was then mixed with AuNPs (4 nM) for incubation of 16 hr. Subsequently, the mixture was aged with NaCl (0.3 M) and potassium phosphate buffer (PB) (10 mM, pH 7.4) for 24 hr. The mixture was then centrifuged at 13, 200 rpm for 30 min to precipitate AuNPs. Supernatant was discarded to remove excess reporter probes and the red precipitate was redispersed in 1X PBS. The redispersed solution was then centrifuged again and redispersed in DI water. The stock concentration of reporter probe-AuNPs complex was 5 nM. For signal enhancement experiment, the reporter probe-AuNPs stock solution was diluted to 500 pM in 1X PBS. A 20 μ l of the diluted solution was added to the graphene channel after H7 target hybridization. After incubation of 2 hr, the

non-specifically adsorbed reporter probe-AuNPs complex was washed away with PBS solution.

3.2.5. Electrical measurement

During the electrical measurement, solution-gate was adopted by inserting a platinum wire electrode as gate electrode into electrolyte (10 mM PB, pH 7.4) on top of CVD graphene channel. Transfer curves were scanned with V_{DS} of 0.05 V and V_G increasing from 0 V to 0.5 V with scanning rate of 4 mV/s.

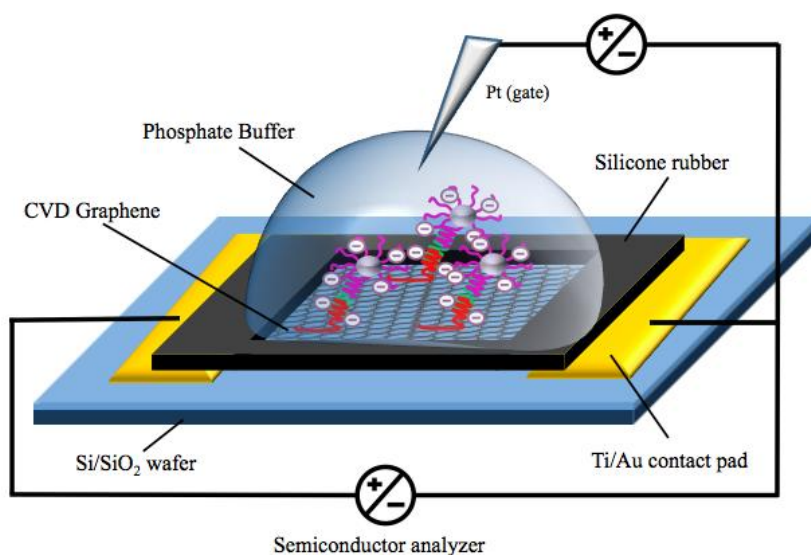


Figure 3.2.4. Illustration of the configuration of CVD graphene-based bioFET during electrical measurement.

3.2.6. Instrumentation

Electrical signals of CVD graphene transistors were measured with semiconductor parameter analyzer (Keithley 4200). Plasma treatment was carried out by a Harrick Plasma cleaner PDC-32G. AFM experiment was performed with a multifunctional Scanning Probe Microscopy (Digital Instruments NanoScope IV). Raman spectroscopy was conducted by Horiba HR800 with 488 nm laser.

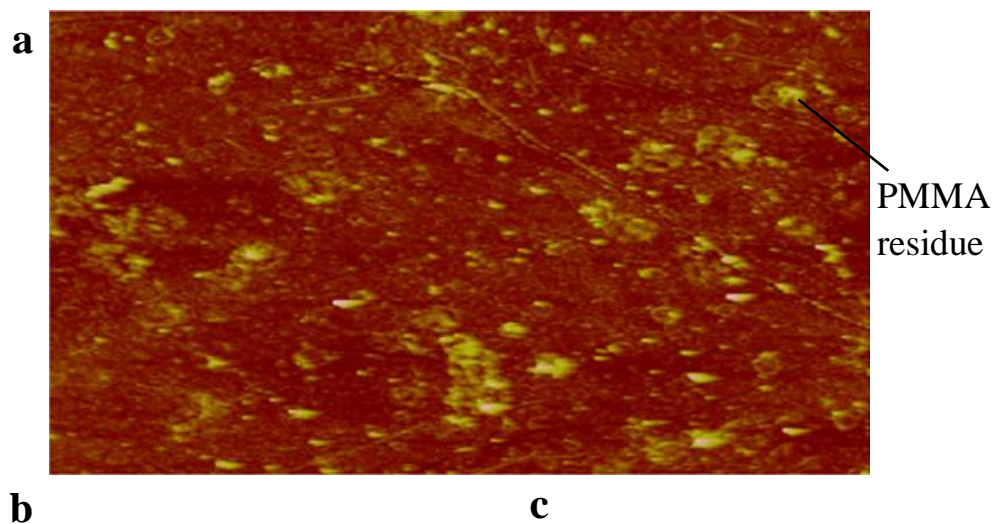
3.3. Results and discussion

3.3.1. AFM image of CVD graphene and TEM images of AuNPs

After graphene was transferred onto a Si/SiO₂ wafer, morphology of CVD graphene was studied by AFM. Figure 3.3.1. a shows AFM image of transferred CVD-grown graphene on a Si/SiO₂ wafer surface. From the AFM image, it can be observed that the graphene surface was quite smooth. However, there were some protrusions, which should be PMMA residue leftover from the CVD graphene transfer process. During copper wet-etching process, the PMMA supporting layer was crucial for maintaining the macrostructure of graphene. Although PMMA wet-transfer of graphene was widely used, the polymer-supporting layer was almost impossible to be cleaned thoroughly by acetone (Lin et al., 2012). PMMA

residues were commonly found on the wet-transferred graphene (Chen et al., 2013). Disregards of those PMMA residues, the graphene transferred was generally flat and smooth without large cracks or defects.

Figure 3.3.1. b and c shows TEM images of AuNPs with diameter of 15 nm and 30 nm respectively conjugated with reporter probes for signal amplification during electrical measurement of biosensor. Two sizes of AuNPs were used in this chapter and their signal amplification effects were. From the TEM images, both of the AuNPs shows good dispersity in water with uniform morphology and without obvious aggregation.



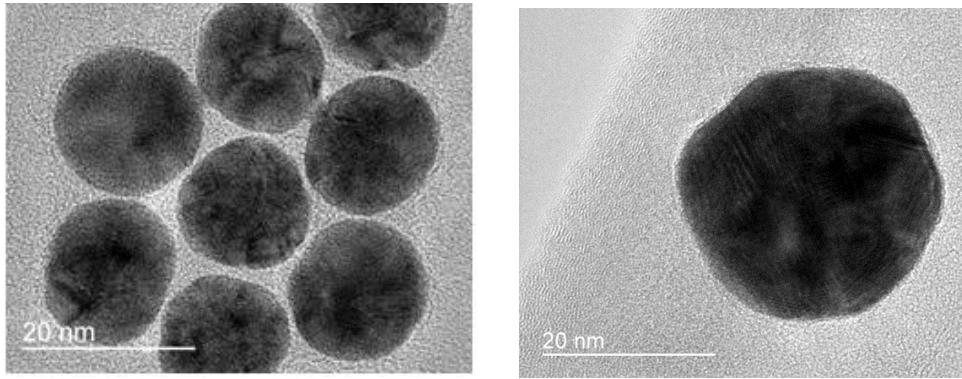


Figure 3.3.1. (a) AFM image of CVD-grown graphene transferred onto a Si/SiO₂ wafer; (b) TEM image of AuNPs in 15 nm and (c) 30 nm conjugated with reporter probes for signal amplification.

3.3.2. Transfer curve of CVD graphene transistor

After the graphene transistor was fabricated, transfer curve was measured in a solution gate setup. Instead of traditional back gate setup, V_G was applied to the analyte on top of the FET channel. When voltage was applied, ions in the analyte were attracted to or repelled from the gate electrode according to their charge. Ions repelled from the gate electrode accumulated on the proximity of graphene and the locally concentrated ions created an electric field that gated the transistor. Solution gate is particularly suitable for a bioFET since most of the biological analyte exists in solution phase. Conventional buffer solution also has high dielectric constant making the graphene FET channel very sensitive to the application of V_G (Heller et

al., 2010, Ohno et al., 2009, Karimi et al., 2014).

Figure 3.3.2. shows the transfer curve of CVD graphene FET device measured with solution gate. A typical “V-shaped” transfer curve was recorded in the measurement. The ambipolar transfer curve is the signature characteristic of graphene. When V_G increased from 0 V to 0.25 V, graphene worked in p-type region, which hole acted as the major carrier. Conductivity of FET channel decreased with the increment of V_G . When V_G increased in the positive direction, positively charged ions accumulated on graphene surface attracting electron carriers in graphene. The attracted electron neutralized hole and decreased the major carrier concentration in graphene. At $V_G = 0.25$ V, conductivity of graphene reached minimum where hole carrier concentration equaled to electron carrier concentration. That point was termed as “charge neutrality point” (V_{CNP}). When V_G increased across the V_{CNP} , the graphene transistor was then working in n-type region, which electron was the major carrier. Increasing V_G led to the restoration of conductivity of graphene. It should also be noted that the V_{CNP} in the transfer curve presented deviated from 0 V, which is the ideal theoretical value. The positive shift of V_{CNP} is a very common phenomenon that adsorption of atmospheric molecules including water, oxygen, and the residue of PMMA could

be the dopant shifting the V_{CNP} to positive side.

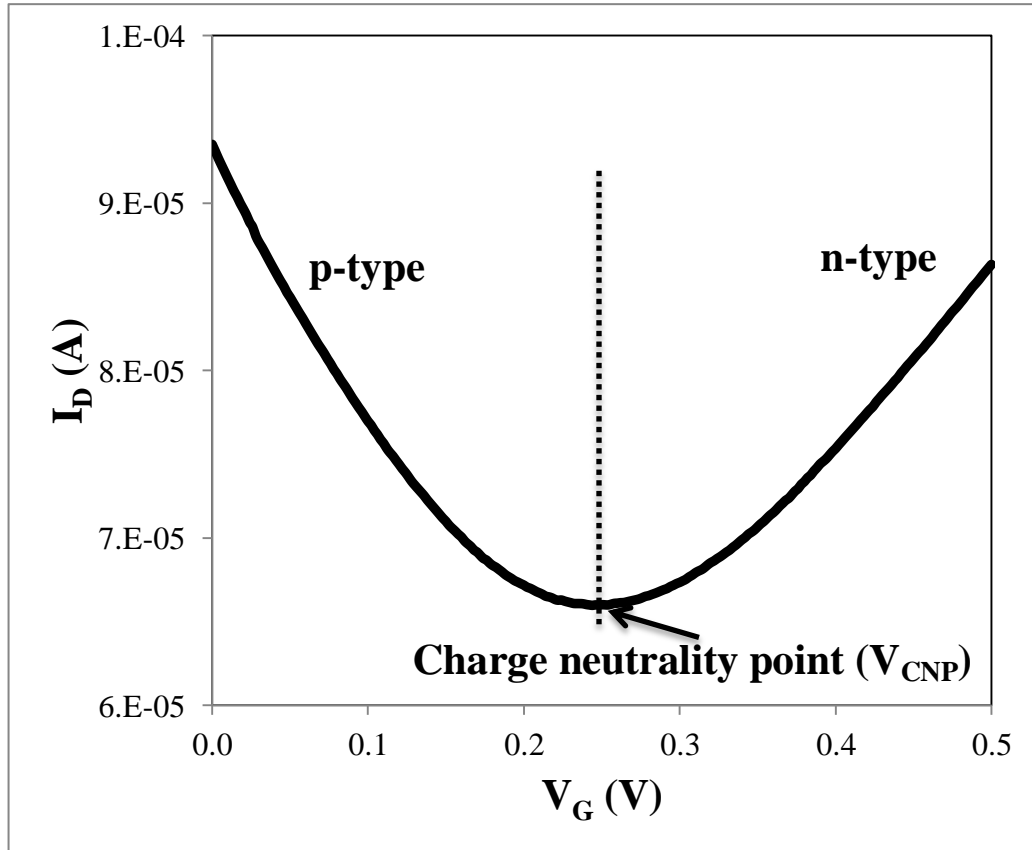


Figure 3.3.2. Transfer curve measured from a bare CVD graphene transistor. V_G was applied through a Pt electrode via solution gate.

3.3.3. Stability of CVD graphene transistor

The CVD graphene FET was proved to be workable in the previous section. In this section, reliability and stability of the transistor was evaluated by continuously sweeping V_G from 0 V to 0.5 V, back to 0 V for seven times. For a bioFET, it is crucial that the intrinsic electrical properties of semiconductor channel remained

unchanged when no event was happening on the surface of FET channel. In a single sweeping, figure 3.3.3. a shows a very obvious hysteresis effect between the forward sweeping and backward sweeping, where two curves did not overlap and an open loop was formed. In a FET device, hysteresis was commonly found when charge was trapped in the dielectric layer after the application of V_G (Paska et al., 2012). When it comes to solution gate, the charge-trapping phenomenon in traditional solid gate would not exist but instead, hysteresis could be caused by the diffusion of ions in the electrolyte. When V_G was applied, dielectric double layer of ions was formed and the graphene FET was gated according to it. When V_G was changed or diminished, the dielectric layer would not disappear instantly but it would gradually dissipate due to diffusion of ions. This delayed formation of dielectric layer could be the reason causing hysteresis effect. Although hysteresis effect was found to exist, it should not be affecting the biosensing performance of our bioFET. In our proposed system, transfer curve of the CVD graphene bioFET was measured before and after introduction of samples. Time intervals between two measurements were in the range of hours, not to mention the repeatedly washing steps removed the dielectric layer formed after the application of V_G .

By comparing transfer curves of multiple sweeps, stability of a transistor can be evaluated. Ideally, transfer curve of different sweeps should completely overlap. However, there are practical reasons that may change the electrical properties of graphene transistor upon transfer curve sweeping. For example, passing current through graphene may damage the structure of graphene and thus hamper the electronic behavior of graphene. In 2007, Moser et al., also reported that when current passes through a graphene device, electromigration and Joule heating effect could lead to a surface cleaning effect on graphene which altered the electrical behavior of graphene (Moser et al., 2007). In our empirical result, figure 3.3.3 a shows that transfer curve in multiple sweeping did not totally overlap with each other. It seems that the CVD graphene bioFET is not totally stable. It is obvious that absolute conductance at different point varied sweeping from sweeping. However, if we take a closer look into those transfer curves, V_{CNP} did not varied too much and stayed at ~ 0.25 V in forward sweeping despite of the variation in absolute current (figure 3.3.3. b). This evidence suggested that V_{CNP} is a reliable indicator to be used in biosensing.

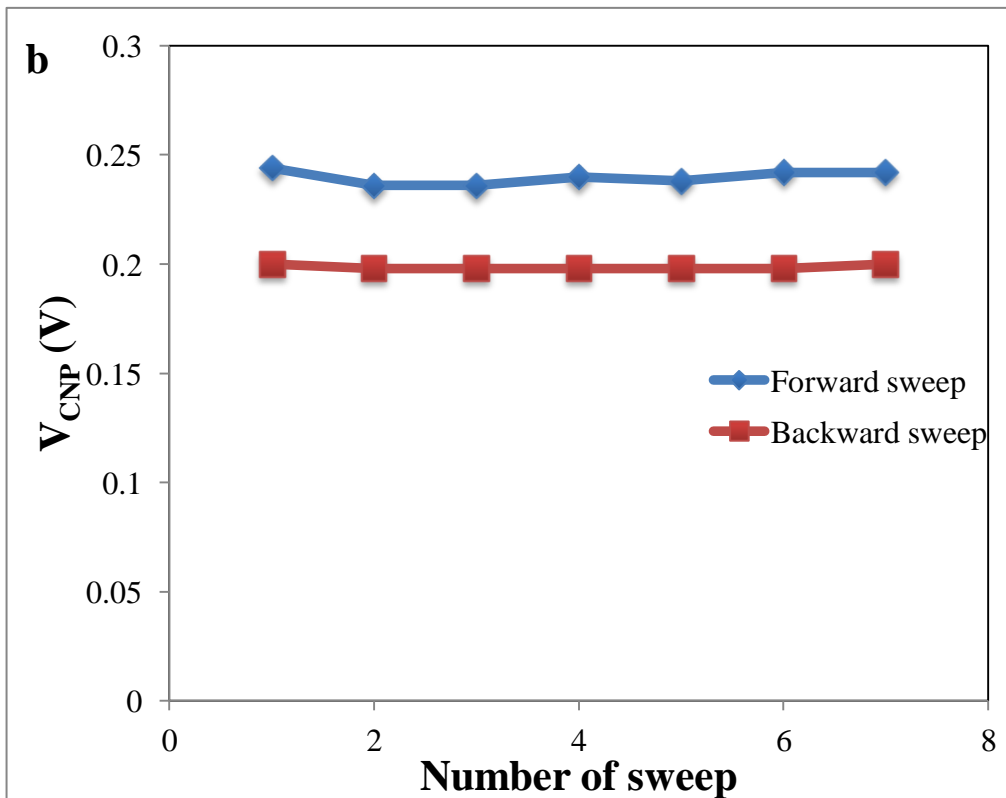
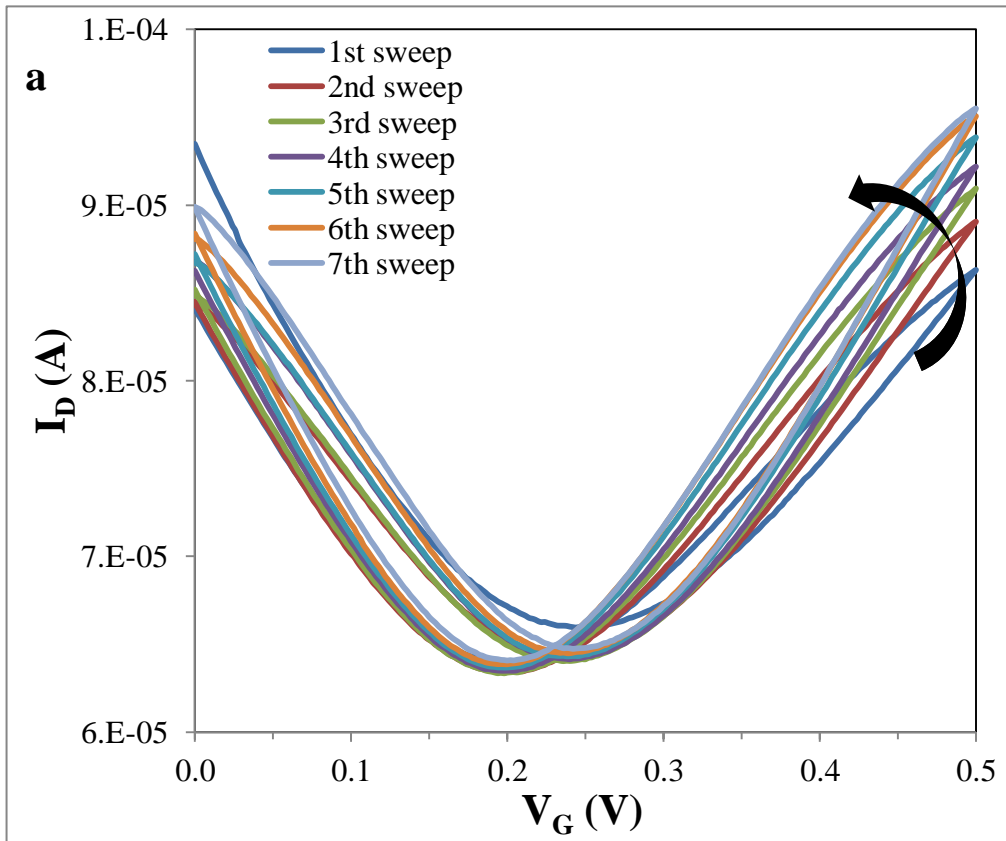


Figure 3.3.3. (a) Transfer curves measured from a bare CVD graphene transistor by sweeping for seven times. (b) V_{CNP} of forward sweep and backward sweep during different number of transfer curve sweeping.

3.3.4. Functionalization and Detection

After the basic electrical behavior of graphene transistor was characterized, its response upon the addition of DNA (including capture probe and target) was investigated. In order to turn the as fabricated CVD graphene transistor into a biosensor, it was firstly functionalized with capture probe. Capture probe consisted of two sections: a.) a section for π - π stacking on graphene and b.) a complementary section for target recognition. In order to assemble capture probe onto graphene surface, it was incubated with graphene overnight forming a self-assemble layer by π - π stacking interaction force between the π electron in graphene and the one in the nucleobases of capture probe.

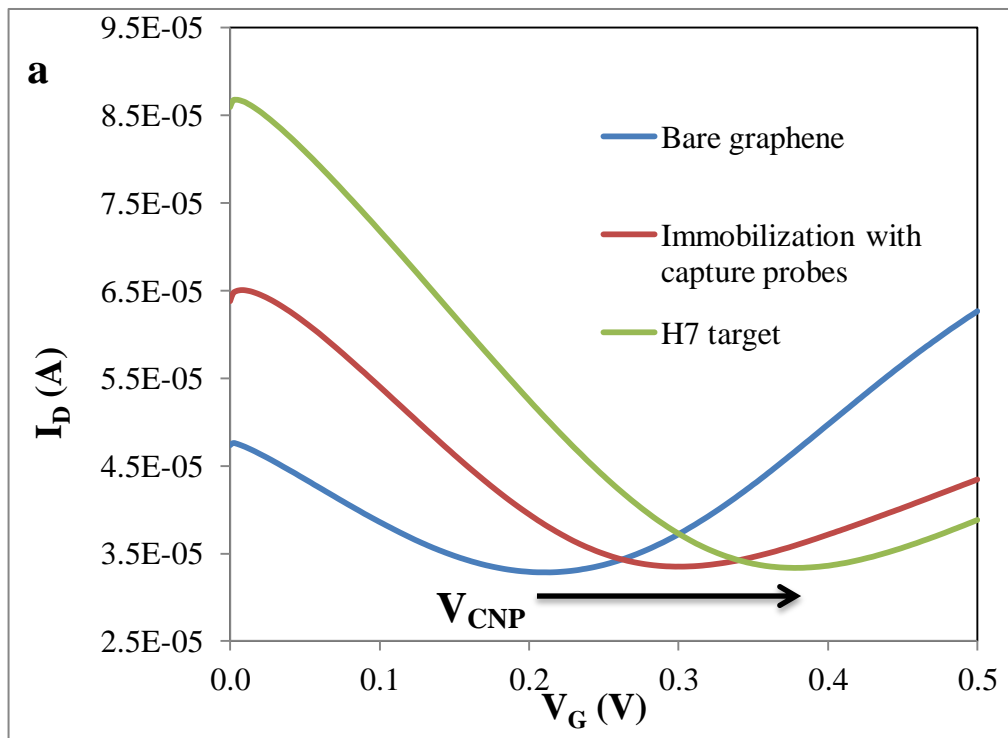
When the bioFET device was functionalized and ready, it was used for H7 target oligonucleotide detection. The transfer curves (I_{D_s} versus V_G) were recorded in various conditions: a.) bare graphene, b.) capture probe functionalized graphene, c.) exposed to H7 target and d.) exposed to non-target DNA. Those transfer curves were measured in 10 mM, pH 7.4 PB as standard electrolyte. After each steps, the graphene surface was rinsed and measured in PB solution again. Figure 3.3.4. a shows the transfer curves of the graphene FET device measured with bare

graphene, after capture probe immobilization, and hybridization with H7 target. The typical ambipolar transfer characteristic of graphene was found in all conditions, without noticeable shift of minimum conductance. Immobilization of capture probes caused a right shift of V_{CNP} from 0.21 V to 0.31 V due to the electrostatic gating effect of DNA. The accumulation of negative charges on the proximity of graphene attracted and increased the hole carrier concentration in graphene. A higher V_G was needed to off-set the electrostatic gating effect posed by capture probes and shifted the transfer curve to positive side. It should be noted that the effect of DNA adsorption on the transfer curve shift of graphene is still controversial. Some of the reports in literature observed a negative shift of transfer curve after DNA adsorption indicating a n-doping effect (Dong et al., 2010, Chen et al., 2013, Lin et al., 2013). Controversially, there are also reports observing positive shift of transfer curve, similar to our case (Lin et al., 2010, Kwon et al., 2012). The mechanism between the interaction of graphene and DNA is very complicated. P-doping, n-doping, chemical gating and electrostatic gating could happen simultaneously (Mohanty et al., 2008, Lu et al., 2010, Yin et al., 2012, Lin et al., 2013). Our empirical result in transfer curve measurement was further confirmed by Raman spectroscopy shows in Figure 3.3.4. c. G peak of graphene shifted positively for about 10 cm^{-1} after probe immobilization. Positive shift of G

peak indicated DNA adsorption posed p-doping effect on graphene, which increased the hole concentration. Disregard of the complexity of the interaction between DNA and graphene, Raman spectroscopy agreed with our empirical data in transfer curve measurement and literature report (Lin et al., 2010).

After functionalization, detection of H7 target was performed by exposing the graphene bioFET to H7 target for two hours. Rigorous washing steps were carried out in order to remove any non-specific adsorption. Introduction of H7 target further increased the V_{CNP} of graphene to 0.36 V, shifting transfer curve to a more positive V_{G} . The shift can be explained by the capture probe specifically hybridized and captured H7 target to the proximity of graphene. When more DNA nucleobases were brought to graphene surface, the charge density on the proximity of graphene was increased. Electrostatic gating and p-doping effect created by DNA were enhanced leading to a positive shift of V_{CNP} . Fig. 3.3.4. b shows the transfer curves of graphene FET incubated with 1 nM non-target DNA. By exposing the graphene bioFET to a relatively high concentration of non-target DNA, whether the biosensor was responding specifically to the designed analytical target can be justified. When the non-target DNA was introduced, no obvious V_{CNP} shift was observed. Non-complementary DNA failed to hybridize

with the capture probes and the vacancy on the graphene channel was occupied by capture probe. Capture probe generate electrostatic repulsion effect to the non-target DNA preventing it from being adhered on the graphene surface. After the vigorous washing steps, surface condition of graphene generally did not change and the transfer curve remained unchanged. Our experiment shows the graphene bioFET has good specificity against the designed analytical target (H7 target) and the shift of V_{CNP} was a reliable transducing indicator.



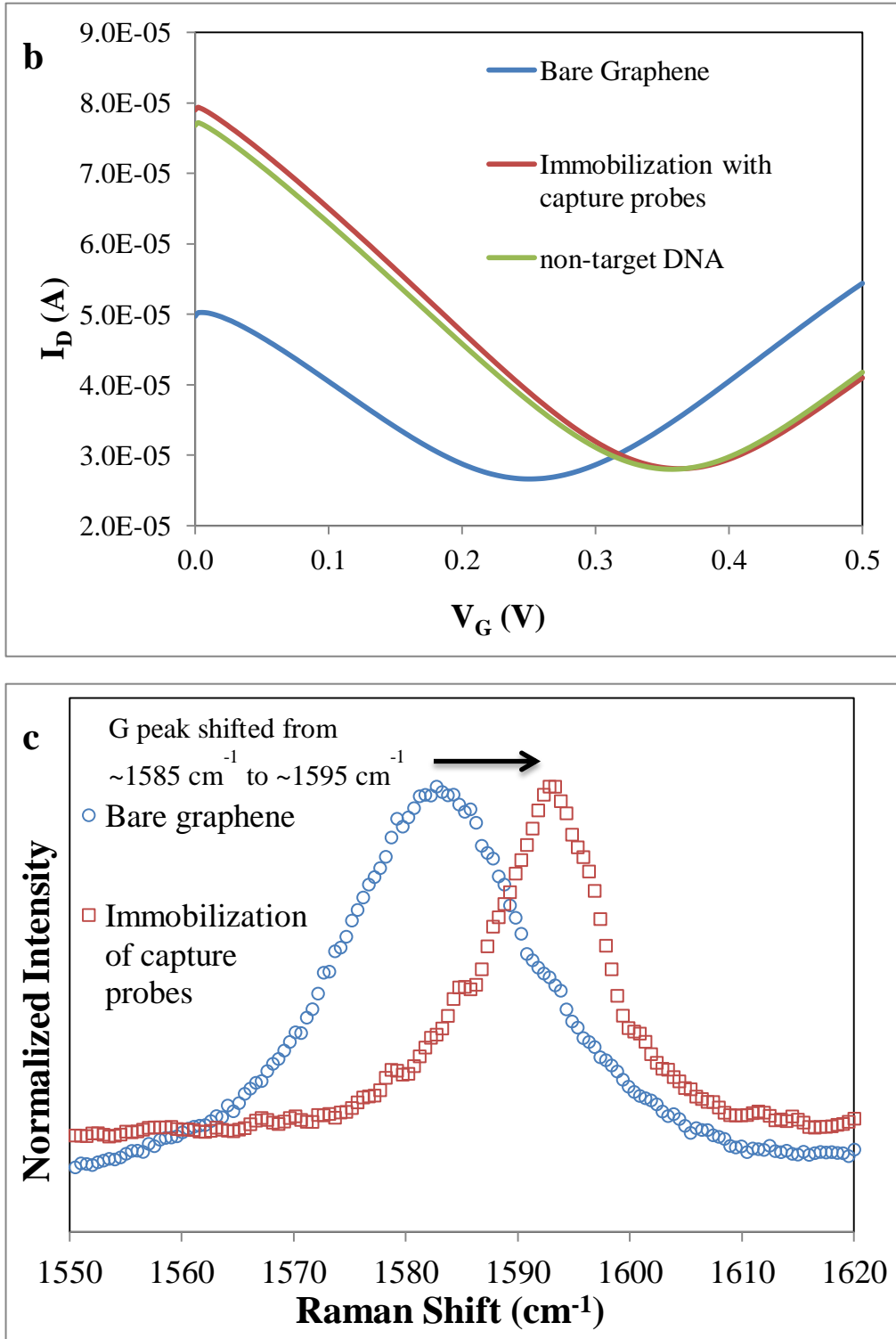


Figure 3.3.4. (a) GFET transfer curves of bare graphene, capture probes functionalized graphene, after incubation with 1 nM H7 target and (b) 1nM non-target DNA. (c) Raman spectrum of bare graphene and capture probes functionalized graphene.

3.3.5. Real-time response

Although the shift of V_{CNP} is a widely used indicator in graphene FET biosensor, the setup of transfer curve measurement is contradictory to real-time measurement. By real-time measurement, valuable information can be obtained including the sensors responding time and hybridization time. It is crucial to ensure target hybridization time is long enough before washing steps in order to develop a reliable system.

After the transfer curve measurement presented in the previous section, real-time measurement was carried out and result shows in figure 3.3.5. Real-time measurement was performed by monitoring the change of I_{DS} ($V_{\text{G}} = 0 \text{ V}$ and $V_{\text{D}} = 0.05 \text{ V}$) in order to unveil the response time of this graphene FET when it was exposed to different concentration (1 pM, 50 pM and 100 pM) of H7 target. The response was normalized as $(I - I_0) / I_0$ in order to obtain a fair inter-device comparison. Stabilized I_{DS} of graphene FET with blank 1X PBS in the sample reservoir as standard electrolyte was defined as I_0 and the current measured when H7 target was introduced was I .

When H7 target was introduced, there was a dramatic fluctuation of I_{DS} which was probably caused by movement artifacts created during sudden injection of sample. The response current increased gradually with time and eventually reached a steady state after approximately 10 – 15 minutes, which is similar to the literature (Stine et al., 2010, Yin et al., 2012). When V_G was set at zero, graphene FET was operating in p-type region where hole was acting as the major carrier. Capturing of H7 target on the proximity of graphene increased the number of negatively charged biomolecules on graphene and increased the hole concentration in graphene. Electrostatic gating and p-doping of H7 target explains the observation in the real-time measurement, which the relative current increased after the introduction of H7 target. By studying the real-time response, it can be observed that the graphene bioFET seems not to be able to detect 1 pM H7 target. When the H7 target concentration increased to 50 pM and 100 pM, the stabilized relative current measured obviously increased. 50 pM H7 target increased the I_{DS} for ~ 5% while 100 pM H7 target increased I_{DS} for ~ 8 %. From this real-time measurement, it can conclude that the DNA hybridization on graphene FET stabilized in approximately 15 minutes. In order to ensure complete hybridization, sample was incubated for 2 hours with GFET in the subsequent experiments.

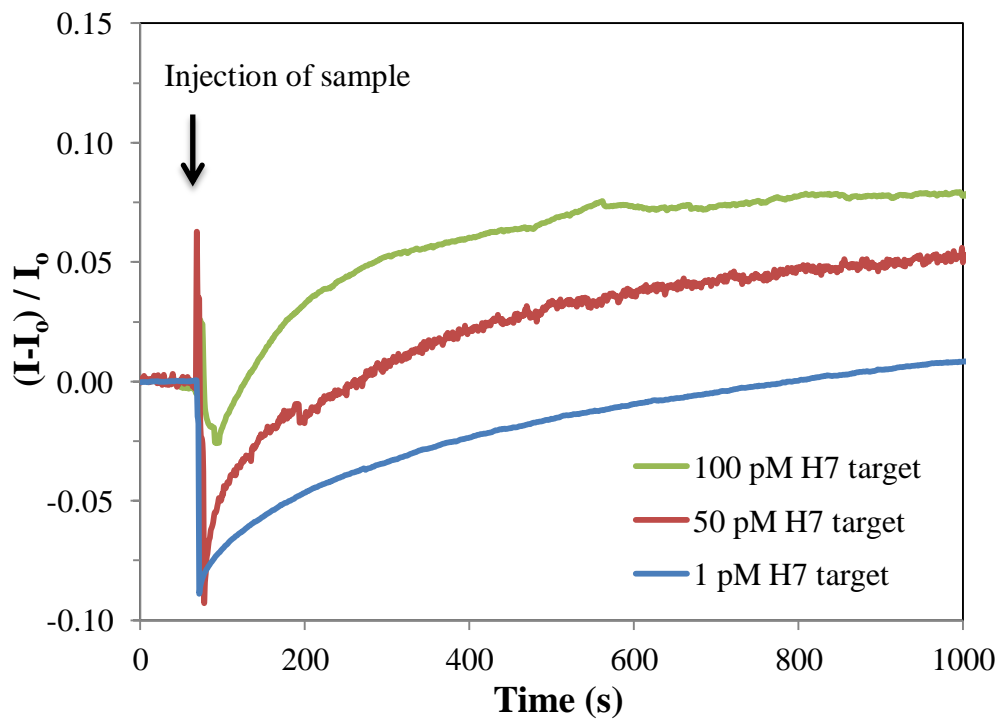


Figure 3.3.5. Real-time response of graphene bioFET biosensors exposed to 1 pM, 50 pM and 100 pM H7 target.

3.3.6. Signal amplification by reporter probe-AuNPs

To explore the signal amplification effect of reporter probe-AuNPs, graphene FET was firstly incubated with $D = 15$ nm reporter probe-AuNPs after exposing to H7 target. There are two possible routes to perform reporter probe-AuNPs enhancement: a.) mix H7 target with reporter probe-AuNPs and incubate the mixture with the functionalized graphene FET channel, or b.) incubate the H7 containing analyte with the graphene FET, wash away excess analyte and

eventually introduce the reporter probe-AuNPs containing solution. In this project, the later route was opted. In the former route, it is possible that multiple H7 target will be hybridized onto a single reporter probe-AuNP, which the excess H7 target will be “wasted” since it cannot be hybridized with capture probe on graphene.

In the experiment, transfer curves at different stages of the sandwich assay were recorded. Figure 3.3.6. a represents the transfer curves of the graphene FET device with capture probes immobilized, 1 pM H7 target hybridized and eventually reporter probe-AuNPs co-hybridized. After each step, SDS and PBS solution was applied gently to wash away any nonspecific binding species before the measurements. Transfer curve measurement before H7 target hybridization was used as a reference point, which was used to compare with the subsequent measurements and calculate the ΔV_{CNP} . In figure 3.3.6. a, it can be observed that 1 pM of H7 target only created a slight response in the graphene FET (V_{CNP} changed from 0.228 V to 0.232 V, $\Delta V_{\text{CNP}} = 4 \text{ mV}$). The ΔV_{CNP} was so small that it could not be distinguished from noise.

After reporter probe-AuNPs co-hybridization, the V_{CNP} of graphene further shifted to positive side. Subsequent reporter probe-AuNPs incubation after H7 target

introduction shifted the V_{CNP} of graphene to the more positive side, where the “undetectable” change was amplified to a “detectable” signal (V_{CNP} changed from 0.228 V to 0.240 V, $\Delta V_{\text{CNP}} = 12$ mV). The reporter probe-AuNPs was coated with DNA and the surface carried negative charge. With reporter probe-AuNPs was introduced to the graphene FET, reporter probe-AuNPs hybridized to the capture probe-H7 target complex and were captured on the graphene surface. The negative charge of reporter probe-AuNPs gated the graphene FET and thus amplified the detection signal.

In order to verify that the signal amplification of graphene bioFET was due to co-hybridization of reporter probe-AuNPs, XPS was carried out to confirm the capturing of reporter probe-AuNPs on graphene surface. XPS spectra presents in figure 3.3.6. b indicated the present of Au element on GFET surface after RP-AuNPs enhancement. Before reporter probe-AuNPs signal amplification was carried out, signal of Au element cannot be observed in the XPS spectrum. After reporter probe-AuNPs treatment, the signature peaks in XPS of Au element appeared which was accounted for the co-hybridized reporter probe-AuNPs being captured on the graphene surface by capture probes/H7 target.

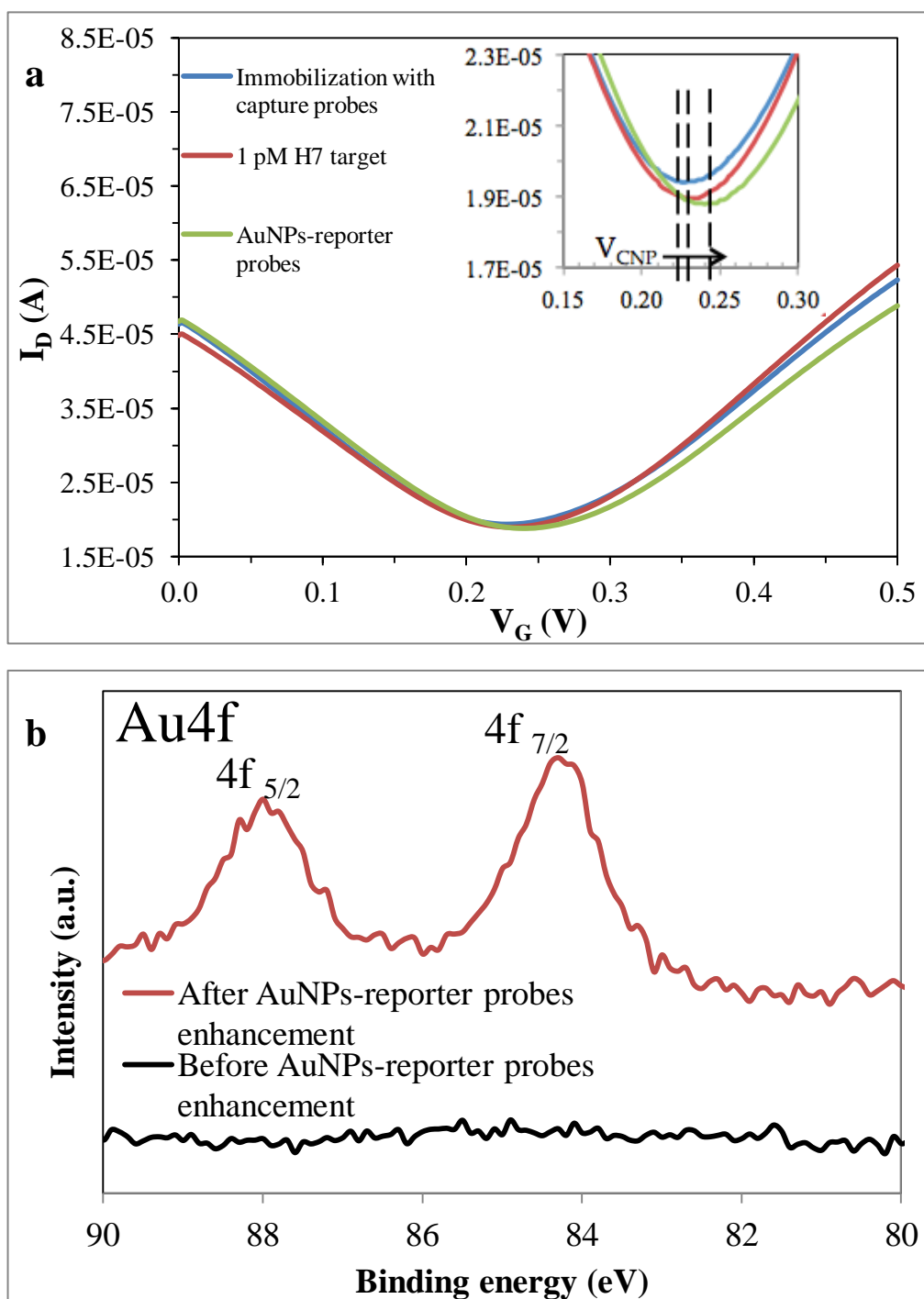


Figure. 3.3.6. (a) Transfer curves of the graphene FET device with capture probes immobilized, exposed to 1 pM H7 target and 15 nm reporter probe-AuNPs. Inset: magnification of the region near V_{CNP} . (b) XPS spectra recorded before and after reporter probe-AuNPs signal amplification.

3.3.7. Effect of the size of reporter probe-AuNPs

To explore the analytical performance of this GFET biosensor setup, further experiments detecting different concentrations of H7 target were carried out. Figure 3.3.7. shows the shift of V_{CNP} of GFET biosensor (ΔV_{CNP}) as a function of concentration of H7 target, with and without further reporter probe-AuNPs (D = 15 nm or 30 nm) amplification. Noise level (mean plus three times of the standard deviation of noise signal) was obtained by incubating GFET with blank PBS was represented by the red-dashed line.

In the absence of reporter probe-AuNPs signal amplification, V_{CNP} right shifted when the H7 target concentration increased from 1 pM to 100 pM. The shift of V_{CNP} (ΔV_{CNP}) linearly correlated with the logarithm of H7 target concentration. Dynamic detection range ended when the concentration of H7 target exceeded 100 pM, probably caused by the saturation of capture probes. This linear relationship was found in both conditions that 15 nm reporter probe-AuNPs signal amplification was and was not applied. 15 nm reporter probe-AuNPs signal amplification increased the sensitivity and lower the LOD of graphene FET biosensor while the dynamic range remained roughly the same. The LOD of GFET with and without reporter probe-AuNPs signal amplification were estimated to be approximately 4 pM and 1 pM respectively.

Application of reporter probe-AuNPs obviously enhanced the graphene bioFET analytical performance while the size of AuNPs could also affect the signal amplification effect. A recent study suggested that solution-gated bioFET is able to respond to an event that happened at a distance much larger than the Debye's length (Palazzo et al., 2015). It was hypothesized that the biomolecules on the surface of FET channel formed multiple layers of dielectric capacitor. The charge in the outermost layer could propagate down to the surface of the FET channel by the dielectric double layer. It would be beneficial to the analytical performance of graphene bioFET when AuNPs with larger diameter were used. AuNPs with larger diameter have larger surface area per-particle and the number of reporter probes loaded on a single AuNP would be more. If those extra negative charges beyond Debye's length can also be detected by the semiconducting channel, larger AuNPs should have a better signal amplification effect. The empirical results shown in figure 3.3.7., the 30 nm reporter probe-AuNPs were found to be posing a greater signal amplification effect on graphene bioFET when compared with the 15 nm reporter probe-AuNPs counterpart. When the 30 nm reporter probe-AuNPs were applied, the LOD decreased to approximately 64 fM. This improvement is probably caused by the increased number of reporter probes per AuNP followed

with the increase of AuNP diameter and surface-area. Although the LOD was improved with 30 nm reporter probe-AuNPs, upper detection limit decreased and the dynamic detection range decreased from 100 pM to 10 pM. It is hypothesized that 30 nm reporter probe-AuNPs occupied a relatively larger space when it was captured on graphene. The maximum number of 30 nm reporter probe-AuNPs that can be captured on a fixed area is lesser than the 15 nm reporter probe-AuNPs, which caused an earlier saturation of binding site and decrement of upper detection limit.

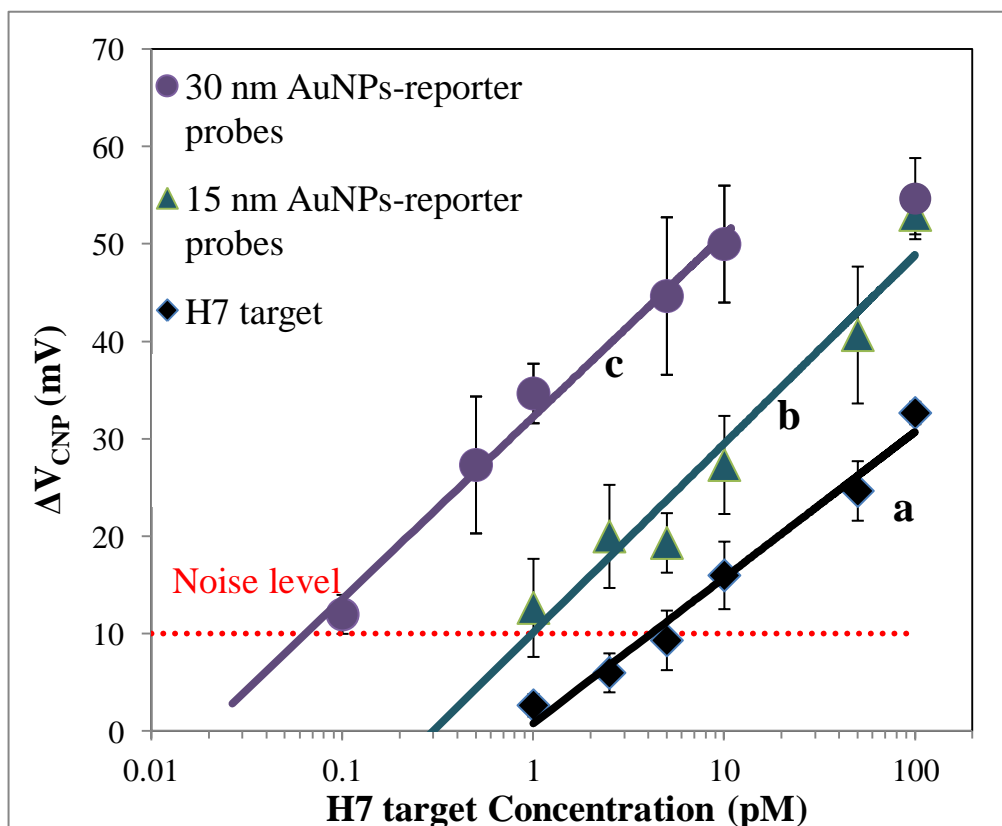


Figure 3.3.7. Shift of V_{CNP} of graphene bioFET after incubation with various H7 target concentrations, (a) without and with (b) 15 nm or (c) 30 nm reporter

probe-AuNPs signal amplification.

3.3.8. Specificity of the graphene bioFET

As a bioFET, specificity in target detection is a very important factor. To verify the specificity of this bioFET, fully complementary H7 target, single-base mismatched DNA and double-base mismatched DNA were introduced to the GFET and their corresponding response were compared. DNA biosensors with the ability of distinguishing single-base mismatch (or single-base nucleotide polymorphism (SNP)) DNA have great importance in clinical analysis (Zhong et al., 2003). Even a small deletion, insertion or point mutation in a human gene could cause severe illness.

In the previous section, 30 nm reporter probe-AuNPs was found to be having a better signal amplification performance and it was chosen to be the reporter probe-AuNPs used in the specificity test. As illustrated in figure 3.3.8., the blank sample and double-base mismatched sample induced a negligible shift of V_{CNP} to the GFET (1.5 mV and -7.3 mV, respectively). The single-base mismatched sample generated a significantly smaller ($\Delta V_{\text{CNP}} = 18.7$ mV) response compared

with the fully complementary H7 target ($\Delta V_{\text{CNP}} = 54.7 \text{ mV}$). This is because the single-base mismatched-capture probe complex was relatively unstable with a lower melting temperature (T_m). Hybridization event between single-base mismatched sample and capture probes is ineffective and unstable. A considerable lesser amount of single-base mismatched sample was captured on the graphene surface, thus resulted in a lower ΔV_{CNP} . All in all, the graphene bioFET with reporter probe-AuNPs signal amplification was able to discriminate fully complementary H7 target with the single-base mismatched DNA. It suggested this biosensor is very specific in H7 target detection.

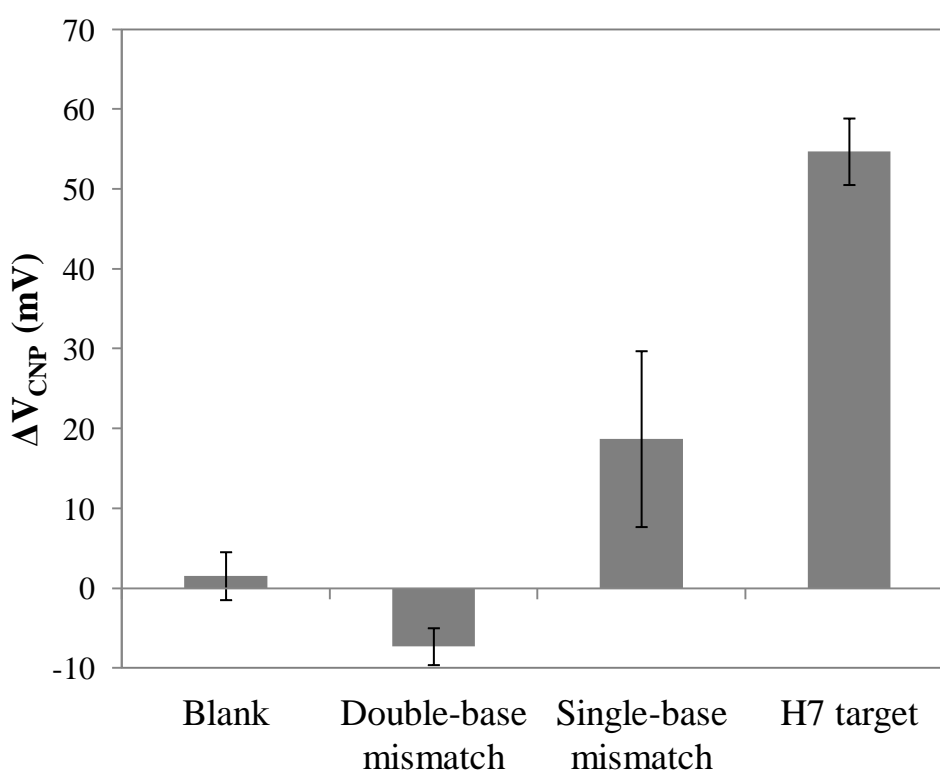


Figure 3.3.8. ΔV_{CNP} of CVD graphene bioFET with reporter probe-AuNPs signal amplification after exposing to blank buffer, double-base mismatch target, single-base mismatch target and fully complementary H7 target.

3.4. Summary

In this chapter, an ultra-sensitive detection of avian influenza virus H7 subtype gene was demonstrated using solution gated CVD-grown graphene-based bioFET via reporter probe-AuNPs signal amplification. The capture probe was assembled on graphene surface while the capture probe was designed into two sections. One section was designed for π - π stacking immobilization and the other section was complementary to H7 target for capturing the H7 target. Capture probe hybridized with half of the H7 target leaving the other half of the H7 target dangling as single-stranded. Afterward, reporter probe-AuNPs were then co-hybridized on graphene surface to form a sandwich assay structure for signal amplification. Best performance of this bioFET setup was achieved by using 30 nm reporter probe-AuNPs for signal amplification, which the LOD was as low as 64 fM.

Chapter 4 A rGO-Modified Gold Electrode for Ultrasensitive Electrochemical Detection of Botulinum Neurotoxin

4.1. Introduction

Bacterial toxins are proteins that secreted by bacterial pathogen and are the major virulence factors accounting for infection in host (Grill et al., 1982 and Rappuoli et al., 1996). Among those, botulinum neurotoxins (BoNT) are extremely lethal toxins secreted by *Clostridium botulinum* (DasGupta et al., 1989). To date, there are seven serotypes (A to G) of botulinum toxins identified. In those seven serotypes, BoNT serotype A (BoNT/A) caused the most foodborne botulism events in human (sobel et al., 2004). Most of the BoNT/A infected patients were infected by ingesting improperly handled food. BoNT/A consists of a heavy chain and a light chain (LcA). The LcA component has enzymatic activity of cleaving synaptosomal-associated protein 25 (SNAP-25), which is a crucial protein for axon terminal to excrete synaptic vesicles (Foran et al, 2003). BoNT/A infected victims hence develop fatal paralytic illness. A reliable, low-cost, rapid and sensitive detection approach for sensing BoNT/A enzymatic activity is important

for ensuring food safety and botulism prevention.

Currently, gold standard of BoNT/A detection remains to be mouse-bioassay.

Although mouse-bioassay is reliable with quite low LOD (20 pg/mL), it requires

well-trained technicians, can only be performed in a laboratory, assay time is

relatively long (~2 to 3 days) and not to mention animals scarification is

mandatory to perform the test (Shapiro et al., 1998). These disadvantages

prevented mouse-bioassay to be an ideal platform for the detection of BoNTs. In

the past decades, different analytical techniques of BoNT/A were proposed.

Examples include cell-based fluorescence resonance energy transfer assay

(Basavanna et al., 2013), enzyme-linked immunosorbent assay (ELISA) (Bok et

al., 2013), fluorescent immunoassay (Jones et al., 2008) and mass spectrometry

(Barr et al., 2011). These approaches are sensitive but still, they required

expensive equipment and complicated experiment protocols. To solve this issue,

an electrochemical biosensing system of BoNT/A is proposed in this project.

Electrochemical biosensor is commonly known as a sensitive, reliable, low-cost

and one-site-operating device. The most renowned example is the glucose meter.

In electrochemical biosensor, graphene has become one of the research focuses,

owing to its extraordinary electronic property, electrochemical catalytic ability, wide working window, abundant functional groups for further modification and biocompatibility (Mao et al., 2014). Different forms of graphene-based electrochemical sensors were explored, including redox probe monitoring (Zhang et al., 2013), direct redox of target biomolecules (Farah et al., 2013 and Lin et al., 2014), enzyme-assisted electrochemical assay (Vilian et al., 2014), impedance spectroscopy assay (Bonanni et al., 2012) or even novel electrochemiluminescence biosensing (Wu et al., 2012).

In this chapter, rGO modified working electrode was used in electrochemical biosensing bacterial toxin BoNT-LcA. rGO-based electrode was covalently functionalized with SNAP-25-GFP which is the enzymatic cleavage target of BoNT-LcA. The SNAP-25-GFP covered rGO working electrode surface, which provided steric hindrance and electrostatic repulsion force to repel redox probe ($[\text{Fe}(\text{CN})_6]^{3-/4-}$) and decreased electrochemical signal generated by redox event. When BoNT-LcA presented in analyte, it specifically cleaved SNAP-25-GFP that reduced the steric hindrance and electrostatic repulsion force on the working electrode, leading to a recovery of the electrochemical signal. Under this proposed biosensing system, the lower LOD was as low as 5 pg/mL LcA and the sensing is

specific to active LcA. Heat-inactivated LcA and LcB provided little to none non-specific interaction. More importantly, this detection system was demonstrated to have little interference from the complex protein environment in real sample (milk). All in all, our proposed LcA biosensor provided a sensitive, specific and reliable sensing platform for the detection of LcA, which could also be anticipated to be developed into a low-cost and portable biosensing platform.

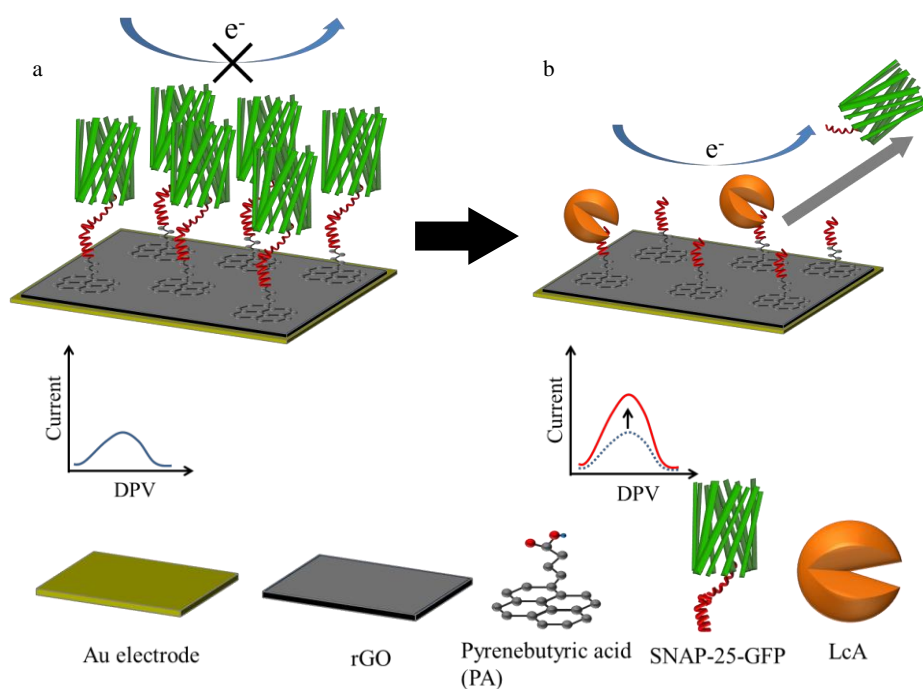


Figure 4.1.1. Detection mechanism of the rGO-based biosensors. (a) SNAP-25-GFP immobilized on rGO blocked the electrode surface preventing electron-transfer. (b) LcA cleaved the SNAP-25-GFP, exposing rGO electrode surface thus recovered DPV signal (Adopted from Chan et al., 2015).

4.2. Research methodology

4.2.1. Materials

GO prepared by modified Hummer's method was obtained from graphene supermarket. Hydrazine monohydrate, Tween 20, Phosphate buffered saline (PBS), tris(hydroxymethyl)aminomethane, SDS, DL-Dithiothreitol (DTT), trihydrate, , 1-pyrenebutyric acid (PA), Sulfo-NHS and MES hydrate, potassium hexacyanoferrate (III) and potassium hexacyanoferrate (II) were purchased from Sigma-Aldrich. Potassium Chloride (KCl) and HEPES buffer were purchased from Sigma. EDC was obtained from Fluka. PDMS (Sylgard 184) was purchased from Dow Corning. Alcohol was brought from Uni Chem. N,N-Dimethylformamide (DMF) was purchased from Acros while Zinc chloride was purchased from Yueqiao. BoNT LcA and SNAP-25-GFP were prepared according to previous study (Ye et al., 2013).

4.2.2. Reduction of rGO

GO prepared by modified Hummer's method was first reduced by hydrazine in order to enhance its electrical property, following previous report (Park et al.,

2011). First, 6 mL GO (0.5 mg/mL) was sonicated for 10 minutes in order to obtain single-layered, well-dispersed solution. Afterward, GO was mixed with 1 μ L hydrazine and 0.03 SDS and the resulted mixture was incubated overnight in 65 °C oven.

4.2.3. Preparation of rGO/Au electrode

Magnetron sputtering was utilized to prepare a thin Ti/Au (roughly 10 nm and 50 nm) film on glass slide as working electrode PDMS film with 5 mm hole punched on it was used to define the effective area of working electrode The PDMS film was fixed on the working electrode by silicon rubber. A metal wire was attached to the Ti/Au film by silver paste for connection to an electrochemical analyzer (VersaSTAT 3). Outside the 5 mm reservoir of PDMS film, silicon rubber was applied to passivate the exposed metal. Finally, the freshly prepared Au electrode was activated under 0.3 M KCl, scanning with CV from -0.2 V to 1.05 V at 100 mV/s for three cycles (Lin et al., 2014).

After the Au electrode was fabricated, rGO was drop casted on the Au electrode and allowed to dry in room temperature. An Au/rGO electrode was then obtained.

4.2.4. Covalently functionalization of rGO/Au electrode with SNAP-25-GFP

To immobilize SNAP-25-GFP on rGO, PA was utilized. PA is a bi-functional linker that has a pyrene ring on one end. Pyrene ring is able to self-assemble with graphene via π - π stacking. Carboxylate terminus on the other end of PA can subsequently be covalently linked with amine terminus in SNAP-25-GFP. Briefly, 30 μ L 10 mM PA in DMF was applied on rGO and incubated for 2 hours. Excess PA and DMF were washed away with alcohol and DI water subsequently. 40 μ L 10 μ M SNAP-25-GFP was immobilized on the PA treated rGO by EDC/NHS chemistry. Afterward, the electrode surface was washed with DI water and 50 mM Tris buffer in order to quench the excess NHS. Finally, the electrode was washed and passivated by 0.5 % Tween-20.

4.2.5. BoNT-LcA enzymatic activity biosensing

To detect the enzymatic activity of BoNT LcA, LcA and LcB samples from frozen stock were diluted by 50 mM HEPES buffer supplemented with 2 mM DTT and 10 μ M ZnCl₂ to various concentrations. Heat-inactivated LcA was prepared by

heating fresh LcA in a 85°C oven for one hour. During detection, 20 μL of sample was pipetted on the Au/rGO/PA/SNAP-25-GFP electrode surface, incubated in ambient environment for 2 hours. Afterward, the electrode was washed with 0.5% Tween-20 and DI water in sequence.

4.2.6. Electrochemical measurement

During electrochemical measurement, the previously fabricated Au/rGO/PA/SNAP-25-GFP electrode was used as a working electrode, Pt wire was used as counter electrode and Ag/AgCl was used as a reference electrode. All three electrodes were connected to VersaSTAT 3 and immersed in 1X PBS with 5 mM $[\text{Fe}(\text{CN})_6]^{3-/4-}$ (1:1) and 100 mM KCl for CV, DPV and EIS measurement.

CV was scanned from -0.2 V to 0.6 V with scan rate of 50 mV/s. DPV was carried out with scanning range from 0.1 V to 0.5 V, 0.02 s pulse width, 4 mV/s scan rate and 50 mV pulse height. EIS was performed with scan frequency ranged from 0.1 Hz to 100 kHz, potential of 0.2 V and amplitude of 5 mV. To quantitatively determine LcA concentration, sensor response was represented by relative change in peak current of DPV (ΔI).

$$\Delta I\% = \frac{\text{DPV peak current measured before sample incubation} - \text{DPV peak current measured after sample incubation}}{\text{DPV peak current measured before sample incubation}} \times 100\%$$

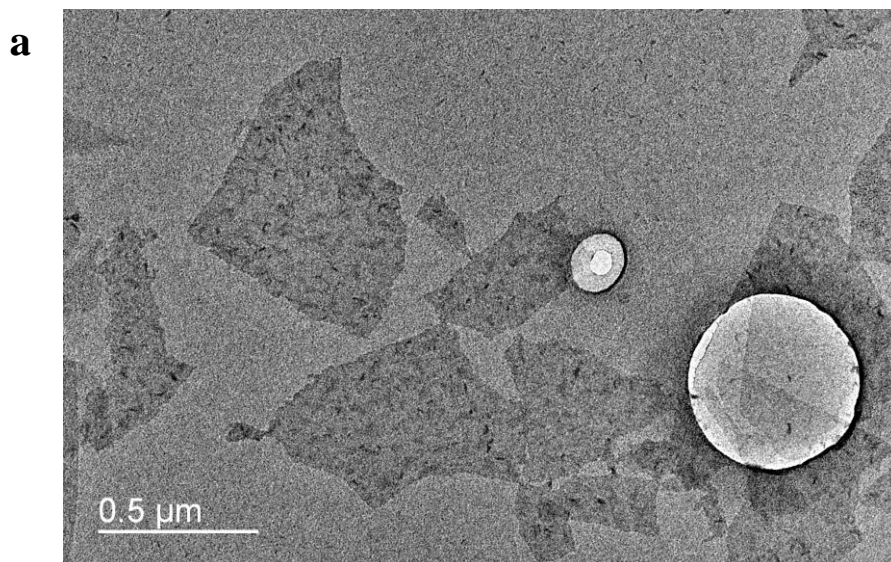
4.2.7. Instrumentation

Electrochemical measurement was performed by VersaSTAT 3 (Princeton Applied Research). TEM images were taken by a field-emission electron microscope from JEOL, model JEM-2100F. Raman spectra of GO and rGO was recorded by Horiba HR800 Raman spectrometer. XPS spectra was performed with a SKL-12 spectrometer modified with VG CLAM 4 multichannel hemispherical analyzer. Ultraviolet–visible (UV-Vis) adsorption spectrum were recorded by Ultrospec™ 2100 pro UV-Visible spectrophotometer. Fourier transform infrared spectroscopy (FTIR) was measured by a PerkinElmer Spectrum 100 FTIR spectrometer (PerkinElmer Inc., USA) that equipped with DTGS (deuterated triglycine sulphate) detector and KBr beam splitter assembly.

4.3. Results and discussion

4.3.1. Morphology of rGO

After the rGO was fabricated, the morphology of it was firstly visualized with TEM. From figure 4.3.1. a, the rGO flakes existed mostly in a mono-dispersed, single-layered form with lateral size of about 500 nm. rGO appeared with wrinkled morphology where they are more prominent in high resolution TEM (Figure 4.3.1 b). These ripples and wrinkles could be the result of deformation and surface cracking after exfoliation processes (Fu et al., 2013, Zhen et al., 2013). With these nanostructured defects, surface-area of rGO contacting redox probe could possibly be increased, giving the working electrode better electrocatalytic performance.



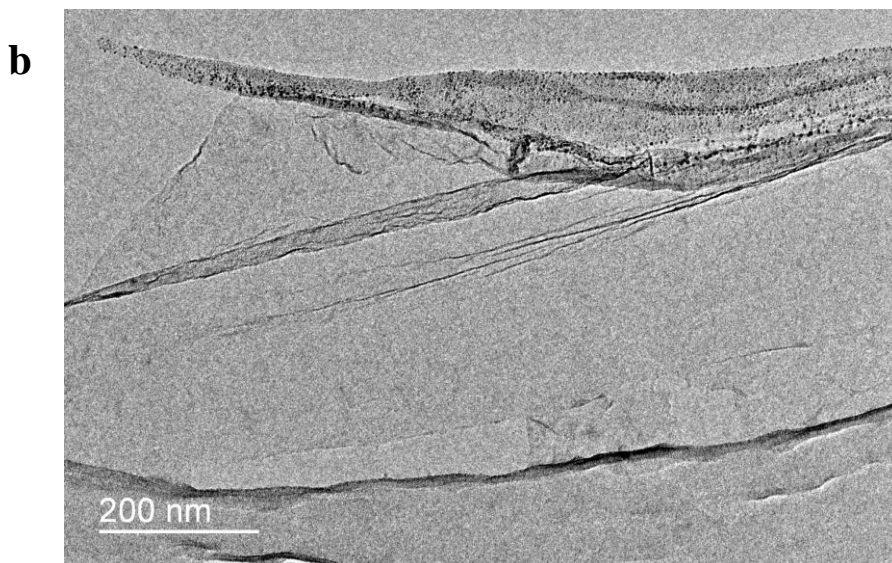


Figure 4.3.1. TEM images of rGO nanoflakes under different magnification (Adopted from Chan et al., 2015).

4.3.2. Characterization of hydrazine reduction

After hydrazine reduction of rGO, the reduction process was characterized by various spectroscopy approaches, including UV-Vis, Raman spectroscopy and XPS. After GO being treated by hydrazine, the most direct observation is that color of solution changed from yellow-brown to black, which was one of the characteristic change after a successful reduction process (Pei et al., 2011). In order to systematically study the color change, GO and rGO were both investigated by UV-Vis (Figure 4.3.2. a). UV-Vis spectrum of GO shows in figure 4.3.2. a indicated two absorption peaks. The first one appeared at 230 nm corresponded to π - π^* transition of aromatic C-C bonds while the second one at

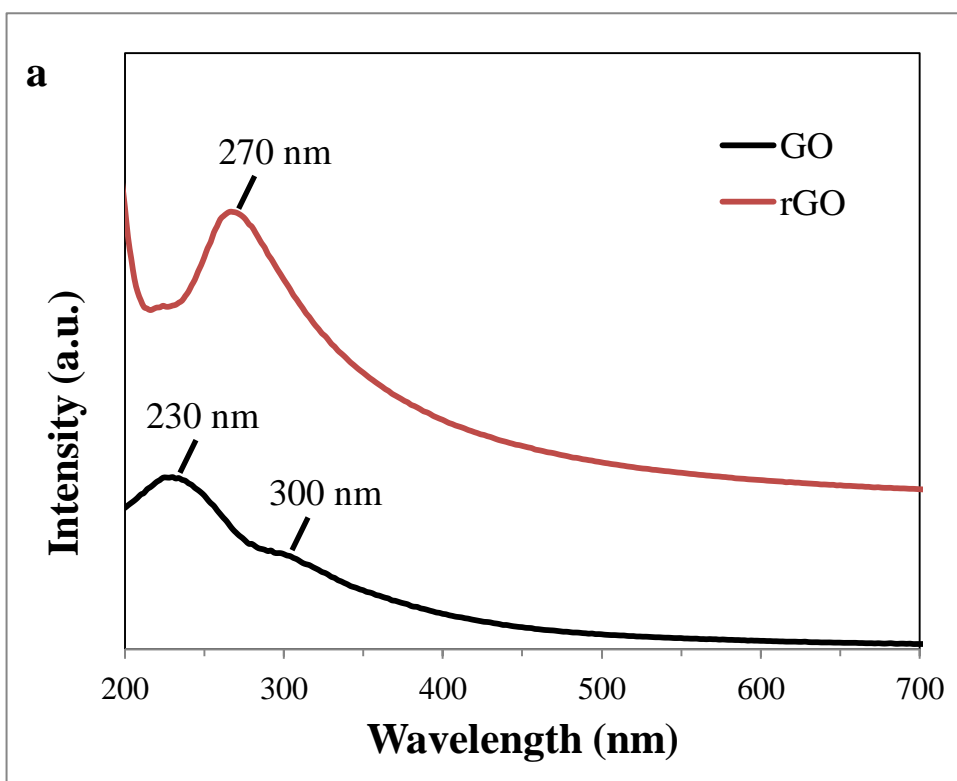
300 nm was generated by $n-\pi^*$ transition of C=O bonds (Das et al., 2014). After reduction, those peaks of GO disappeared and a new absorption peak at 270 nm rose. It was caused by the restoration of carbon aromatic structure after reduction which shifted absorption peak of the $\pi-\pi^*$ transition of aromatic C–C from 230 nm to 264 nm (Li et al., 2008).

Raman spectroscopy is another widely adopted method for characterizing the quality of graphene-based material. In the Raman spectra of GO, there is two signature peaks: a.) D band at $\sim 1350\text{ cm}^{-1}$ and b.) G band at $\sim 1600\text{ cm}^{-1}$ (Kudin et al., 2008; Stankovich et al., 2007). G band originated from the in-phase vibration of carbon in-plane sp^2 domain of graphene while the D band came from the edge of graphitic domain. Raman spectrum of our GO and rGO presents in figure 4.3.2. b. Before reduction process, GO possessed a slightly higher relative intensity of G band compared with D band. After the reduction process, rGO had a relative intensity decrement in G band and a rise of relative intensity in D band, while the height of D band surpassed the one of G band. This observation can be explained by creation of new and smaller graphitic domains during hydrazine reduction, which decreased the average size of sp^2 domains in graphene. The decrease of I_D/I_G in rGO after reduction process was also reported in previous research, which

suggested our hydrazine reduction was successful (Stankovich et al., 2007).

To further investigate the change of elemental composition of rGO after hydrazine reduction, XPS was adopted. XPS is a very powerful tool of studying the elemental composition of a material that can detect the presence of an element with very low concentration (down to parts per thousand range). XPS spectrum of GO and rGO shows in figure 4.3.2 c. In the XPS spectrum of GO, there are three prominent peaks, which correspond to C 1s, O 1s and N 1s. C 1s attributed to the carbon in GO while the O 1s accounted for the oxygen containing functional groups (or defects) including hydroxyl, epoxy, carboxyl groups. Besides these major component, there are also trace amount of nitrogen detected by XPS. Those nitrogen atoms may be doped into GO during chemical exfoliation process, which nitric acid was used as one of the oxidizing agent. After reduction, there was an obvious decrease in the O 1s peak of rGO. The proposed reaction pathway of hydrazine reduction started with a ring-opening process of epoxy group and the epoxy group transformed into an aminoaziridine moiety. Finally, the aminoaziridine moiety undergone thermal elimination of di-imide and the $-C=C-$ was restored (Stankovich et al., 2007). Besides the epoxy-elimination suggested, Gao et al., proposed that hydroxyl groups within the aromatic region of GO is not

stable. At moderate temperature, they can be removed or migrate to the edge of GO (Gao et al., 2009). As a result of these hypothesis, the decreased of O 1s peak in the XPS spectrum of rGO provided a solid evidence of the successfulness in the hydrazine reduction process.



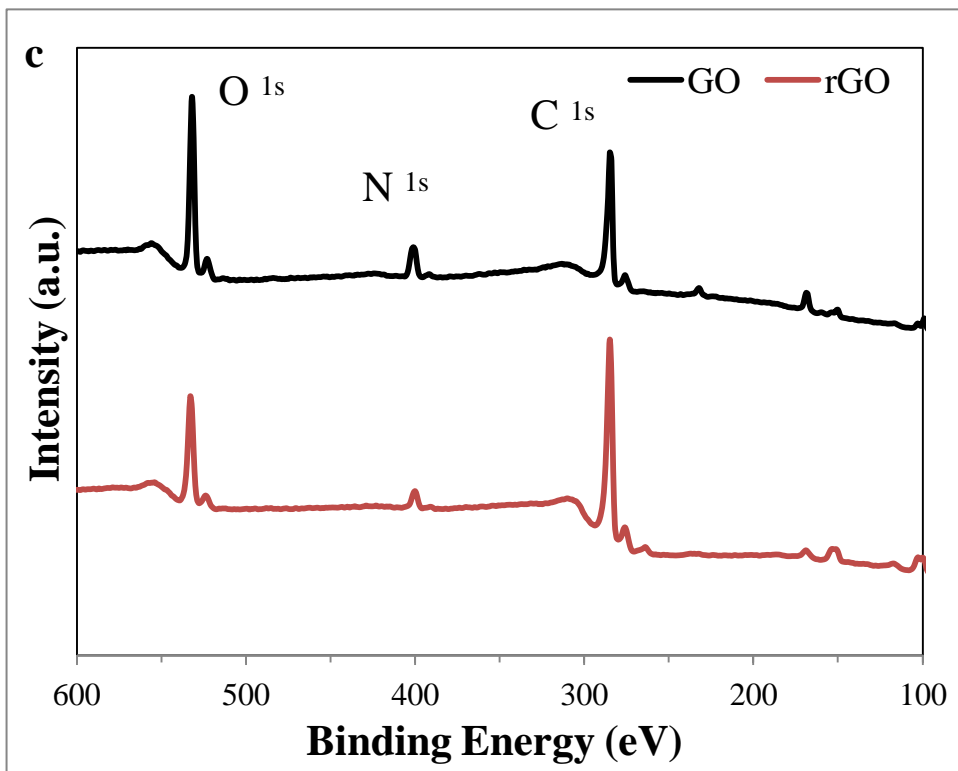
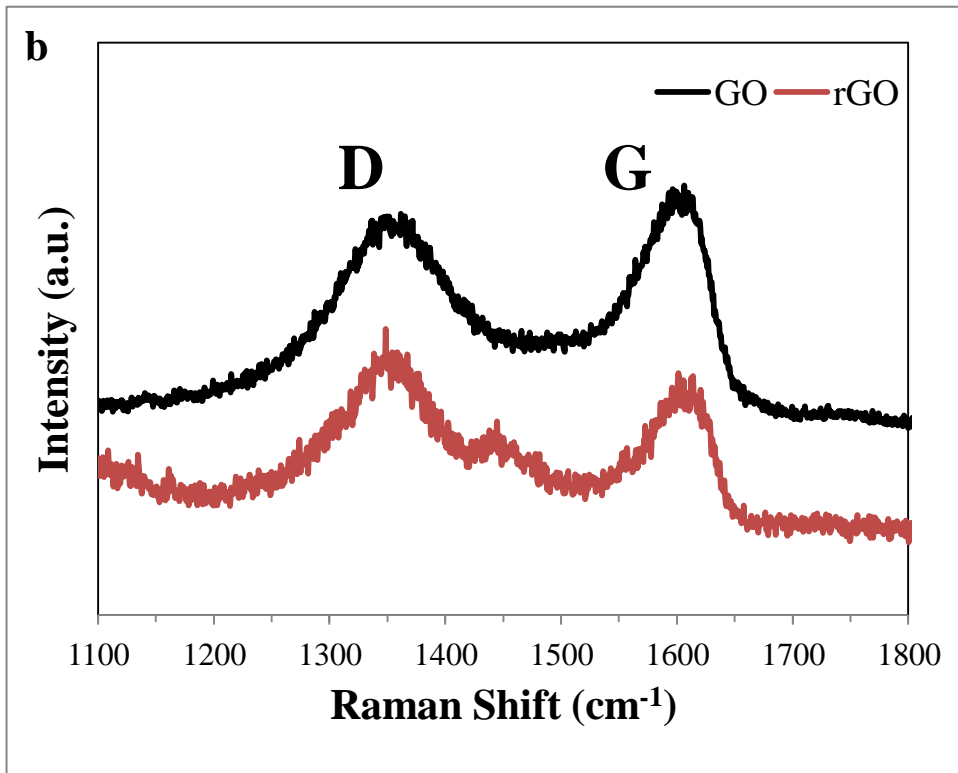


Figure 4.3.2. (a) UV-Vis spectrum, (b) Raman spectrum and (c) XPS spectrum of GO and rGO (Adopted from Chan et al., 2015).

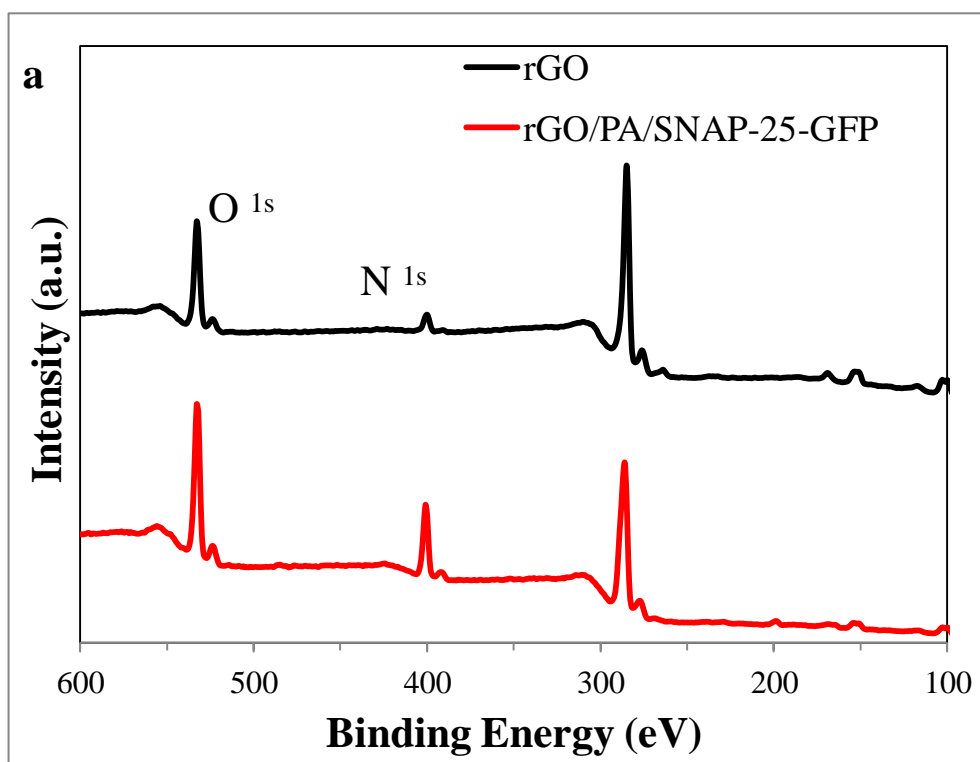
4.3.3. Characterization of SNAP-25-GFP immobilization

After rGO was successfully reduced, subsequent covalent-immobilization of SNAP-25-GFP on rGO film was achieved by EDC/NHS chemistry with PA linker molecule. The result was confirmed by XPS and FTIR.

Figure 4.3.3. a shows the XPS spectrum of rGO film and SNAP-25-GFP modified rGO/PA/SNAP-25-GFP film. Comparing those XPS spectrum, rGO/PA/SNAP-25-GFP film has increased relative intensity of N_{1s} and O_{1s} peaks. The source of nitrogen and oxygen atoms detected by XPS should be attributed to the SNAP-25-GFP immobilized on rGO. SNAP-25-GFP is a protein in nature, which composed with amino acids linked by amide bond. Amide bond and amino acid itself contains abundant nitrogen and oxygen elements that contributed to the rise of N 1s and O 1s in the XPS spectrum of rGO/PA/SNAP-25-GFP.

To further confirm the immobilization of SNAP-25-GFP, FTIR spectrum of rGO and GO/PA/SNAP-25-GFP were obtained and shows in figure 4.3.3. b. In the FTIR spectrum of rGO, there were no obvious absorption peak except the one of -OH at $\sim 3401\text{ cm}^{-1}$, which corresponded to the abundant hydroxyl group on rGO.

After conjugation of SNAP-25-GFP, a few new absorption peaks in FTIR spectrum appeared, including $\text{-CH}_2\text{-}$ stretching vibration at $\sim 2925\text{ cm}^{-1}$ and 2860 cm^{-1} , -CO-NH- at $\sim 1660\text{ cm}^{-1}$ and $\sim 1580\text{ cm}^{-1}$, -CO stretching vibration at 1213 cm^{-1} . Those peaks attributed to the ethyl groups and amide bonds from SNAP-25-GFP and suggested the immobilization process was successful.



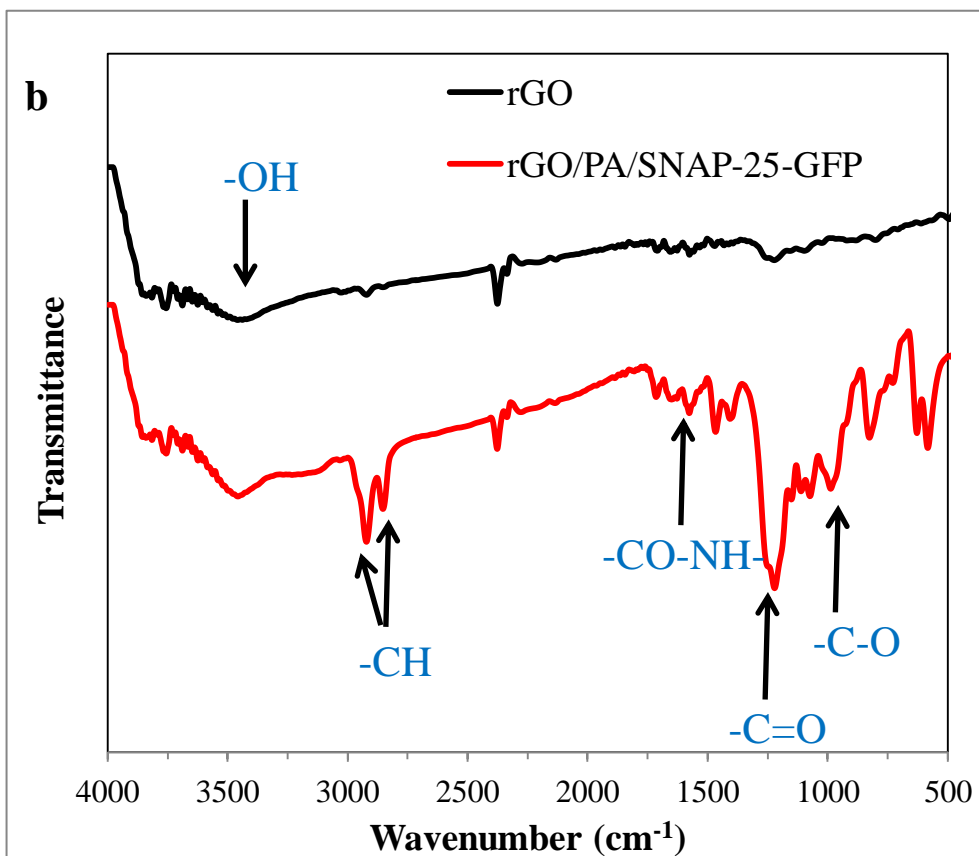


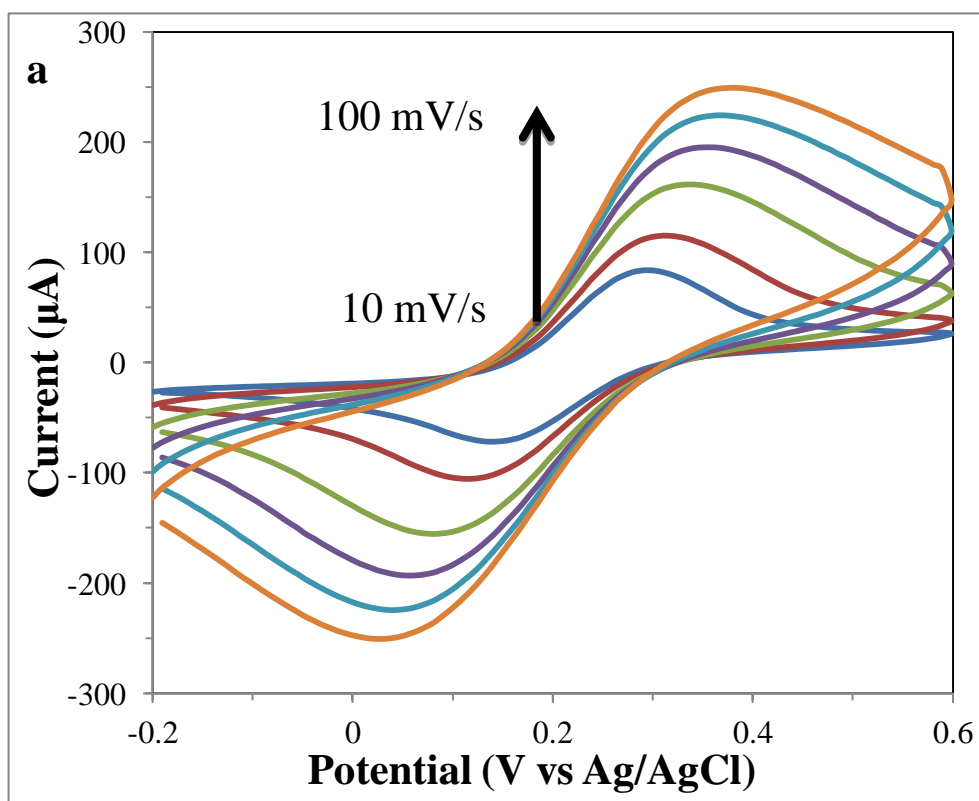
Figure 4.3.3. (a) XPS spectrum and (b) FTIR spectrum of of rGO and rGO/PA/SNAP-25-GFP (Adopted from Chan et al., 2015).

4.3.4. C.V. electrochemical behavior of Au/rGO working electrode at different scanning rate

After rGO was drop-casted on Au electrode, CV was performed using the as-prepared Au/rGO working electrode under pH 7.4 1X PBS supplemented with 5 mM $[\text{Fe}(\text{CN})_6]^{3-/4-}$ and 100 mM KCl with different scanning rate. In figure 4.3.4. a, there was a pair of well-defined redox peaks in each of the CV scanning curves, which attributed to the redox event of $[\text{Fe}(\text{CN})_6]^{3-/4-}$. When the scanning rate was

increased, anodic and cathodic peak currents (I_{pa} and I_{pc}) increased accordingly.

Linear relationships were found between I_{pa} or I_{pc} and square root of scan rate and the plot shows in figure 4.3.4. b. This relationship revealed the electrochemical kinetics was a solution phase quasi-reversible process and the electrochemical peak currents were limited by diffusion of redox probe while the heterogeneous electron transfer process between redox probe and working electrode was rapid. The rapid electron transfer characteristic of our Au/rGO electrode could be benefited by the superior electrochemical catalytic ability of rGO.



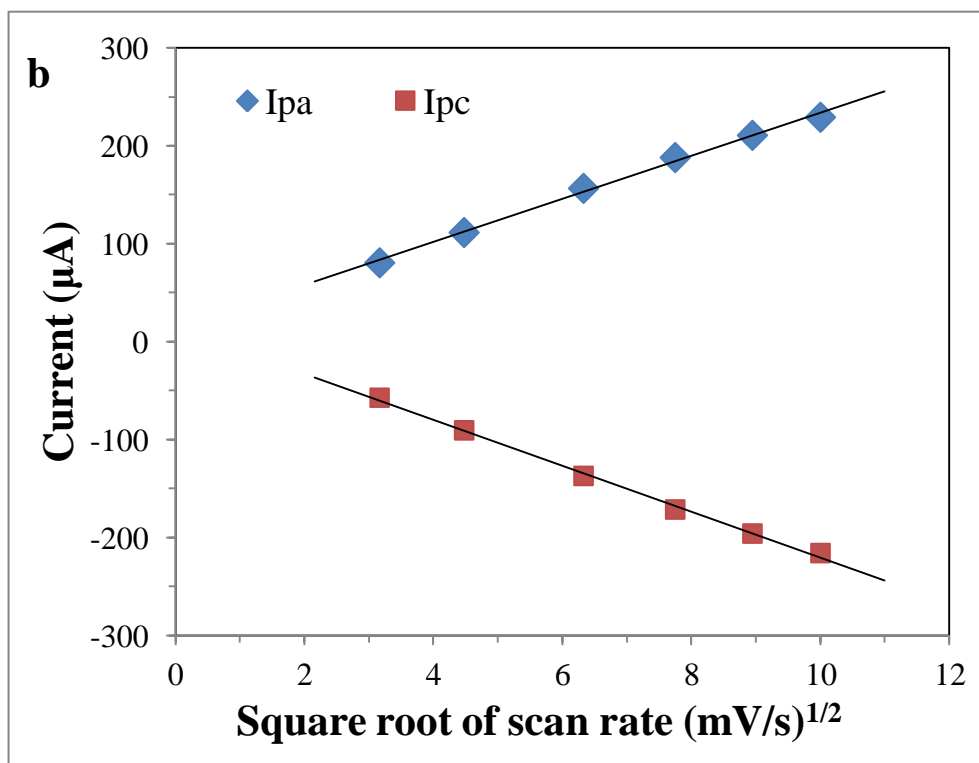


Figure 4.3.4. (a) Cyclic voltammogram of Au/rGO electrode scanning from -0.2 V to 0.6 V with various scanning rate (10 mV/s, 20 mV/s, 40 mV/s, 60 mV/s, 80 mV/s, 100 mV/s) in pH 7.4 1X PBS supplemented with 5 mM $[\text{Fe}(\text{CN})_6]^{3-/4-}$ and 100 mM KCl. **(b)** Anodic (I_{pa}) and cathodic current (I_{pc}) plot against the square root of scanning rate (Adopted from Chan et al., 2015).

4.3.5. C.V. and E.I.S. characterization of working electrode modification

Physical characterization methods presented in the previous sections confirmed the hydrazine reduction and SNAP-25-GFP conjugation process were successful. In this section, effects of each modification steps on the electrochemical behavior of working electrode were investigated by CV and EIS.

Cyclic voltammograms of bare Au electrode, Au/rGO electrode, Au/rGO/PA electrode and Au/rGO/PA/SNAP-25-GFP was recorded in pH 7.4 1X PBS

supplemented with 5 mM $[\text{Fe}(\text{CN})_6]^{3-/4-}$ and 100 mM KCl, scanning from -0.2 V to 0.6 V under scan rate of 50 mV/s. In the cyclic voltammograms scanning with bare Au electrode, a pair of reduction peak and oxidation peak can clearly be observed (Figure 4.3.5. a). After modifying with rGO, dramatic intensity enhancement of both peaks were observed. This enhancement could be attributed to the superior catalytic ability and charge transfer ability of graphene while this observation agreed with those literature reported (Lin et al., 2011; Zhang et al., 2013).

After rGO was drop-casted and dried on Au electrode, PA in DMF was incubated with the Au/rGO electrode. Pyrene ring in PA enabled it to be self-assembled on rGO. After PA was adhered on rGO, there was an obvious decrement in CV peak current. The suppression of electrochemical signal after the modification of PA can be explained by two reasons. Firstly, the layer of PA physically covered the rGO electrode and prevented it from encountering the redox probes ($[\text{Fe}(\text{CN})_6]^{3-/4-}$) by increasing steric hindrance. Secondly, the carboxyl group grafted on rGO by PA deprotonated under neutral buffer solution carried negative charge. Those negative charges on rGO created electrostatic repulsion force against redox probes, which were also negatively charged. These two factors

contributed together for the peak current decrement in the cyclic voltammogram of Au/rGO/PA electrode. Finally, SNAP-25-GFP was conjugated on the Au/PA/SNAP-25-GFP electrode and the corresponding redox peak in cyclic voltammogram was further suppressed. There are two major factors contributed to this observation, similar to the reason of PA modification. Firstly, coverage of SNAP-25-GFP on the rGO surface increased steric hindrance, which prevented redox probe from performing electron-transfer on the electro surface. Secondly, the isoelectric point of SNAP-25-GFP is smaller than the pH of the buffer solution (4.66 for SNAP-25 and 6.2 for GFP). SNAP-25-GFP was deprotonated and its negative charge provided electrostatic repulsion force, which further suppressed the electrochemical signal by repelling the redox probe away from electrode surface.

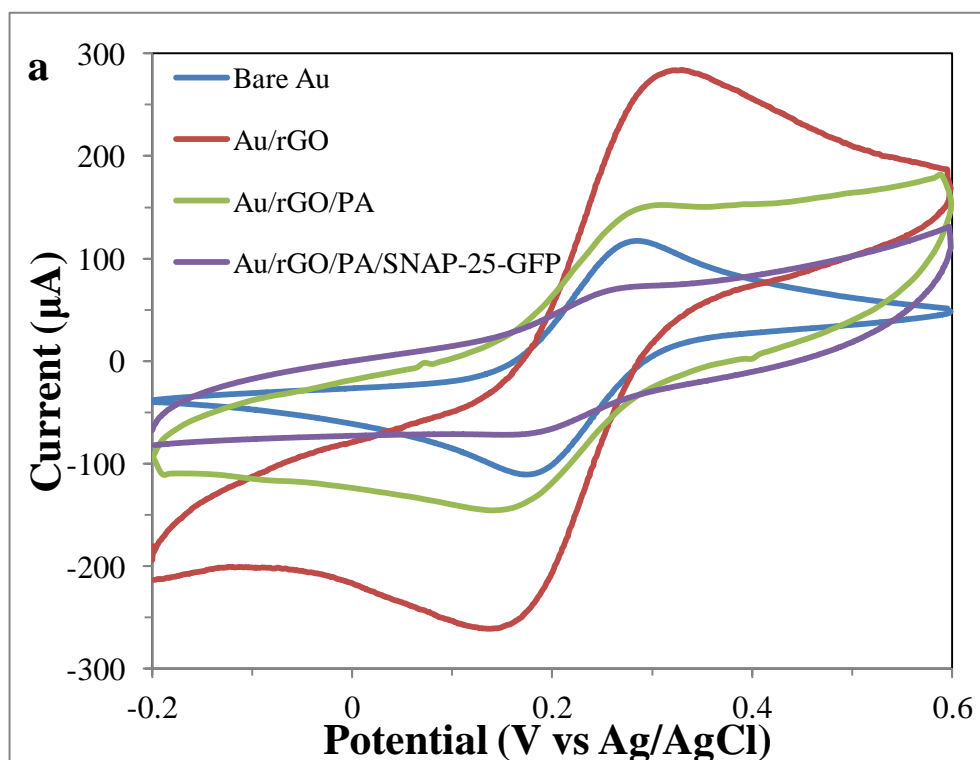
Besides CV, EIS was employed to study the surface behavior of working electrode during different modification process. EIS is a very sensitive electrochemical technique that can provide lots of information about the electrochemical events happening on the surface of electrode (Bonanni et al., 2012). As for a graphene-based electrode, it is indeed very suitable for being investigated under EIS given by its metallic conductivity, rapid heterogeneous

electron transfer rate and extraordinary high surface area (Bonanni et al., 2012).

In the EIS spectrum, the data was fitted to a Randles equivalent circuit, as shows in figure 4.3.5. b. The Randles equivalent circuit consisted of four components. R_1 stands for the solution phase resistance. CPE is the constant phase element of the circuit, while it is sometimes expressed in double-layer capacitance. R_{ct} corresponds to the heterogeneous R_{ct} of the electrode against redox probe when operating in Faradaic mode. W is the Warbuge impedance, which corresponds to mass-transfer diffusion in the system. Here, we particular interest in the change of R_{ct} after different modification steps. R_{ct} is a very sensitive parameter, which can reflect subtle changes on the electrode. In Nyquist plot, there is a semi-circle and a linear component. The semicircle of Nyquist plot at high frequency range represented the electron-transfer process at the electrode surface while R_{ct} can be obtained from the diameter of the semi-circle component.

Figure 4.3.5. b shows EIS plot of bare Au electrode, Au/rGO electrode, Au/rGO/PA electrode and Au/rGO/PA/SNAP-25-GFP electrode fitted to Randles equivalent circuit. EIS spectrum of bare Au electrode forms a typical shape of Nyquist plot, consisted with a semi-circle and a linear component. After modified with rGO, the Nyquist plot of Au/rGO electrode had a decreased diameter of

semi-circle, indicating a decrease of R_{ct} . This phenomenon should be attributed to the outstanding catalytic effect of rGO, which speeded-up the heterogeneous electron transfer between electrode and redox probes. By modifying with PA and SNAP-25-GFP, the R_{ct} of electrode increased gradually. This should be account for the steric hindrance and electrostatic repulsion effect built up gradually after the immobilization of PA and SNAP-25-GFP against the negatively charged redox probe. These observations in EIS characterization throughout electrode modification steps genuinely agreed with the observation using CV as characterization technique while providing a bit more information about what was happening in the electrochemical system.



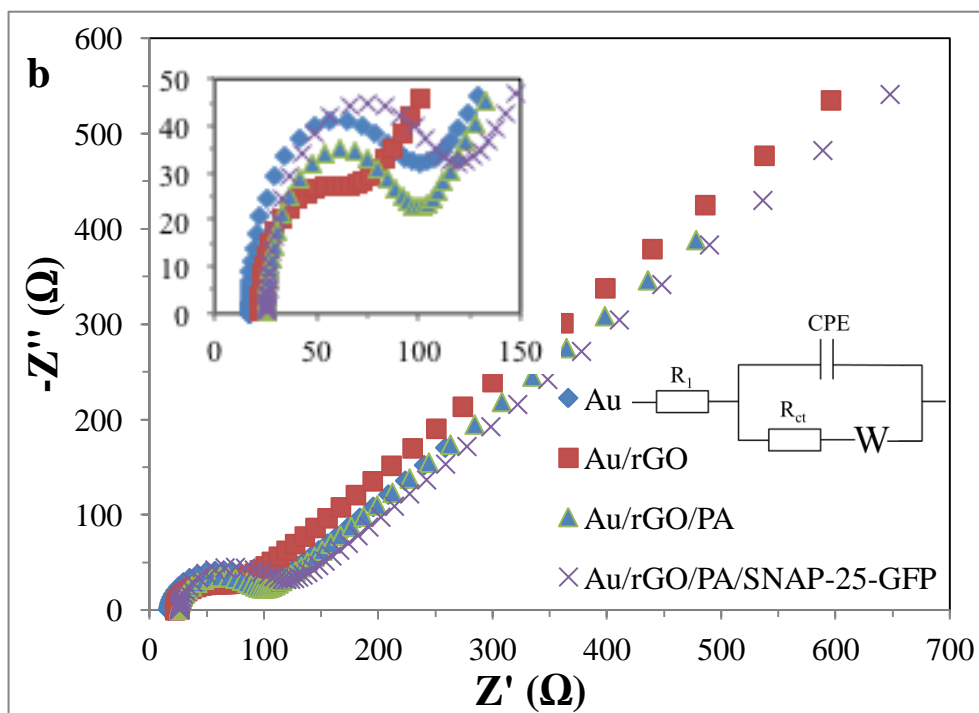


Figure 4.3.5. (a) Cyclic voltammograms and (b) EIS Nyquist plot with Au, Au/rGO, Au/rGO/PA and Au/rGO/PA/SNAP-25-GFP modified electrodes. Measurement was performed in pH 7.4 1X PBS supplemented with 5 mM $[\text{Fe}(\text{CN})_6]^{3-/4-}$ and 100 mM KCl. Inset: magnified Nyquist plot (Adopted from Chan et al., 2015).

4.3.6. LcA detection using differential pulse voltammetry (DPV)

Successfulness of the electrode functionalization process was established by various characterization methods in the previous sections. In this section, the functionalized electrode (Au/rGO/PA/SNAP-25-GFP) was used to detect enzymatic activity of LcA. In order to detect LcA, DPV was chosen as the method to obtain signal from the electrochemical system. DPV is an extremely sensitive electrochemical technique and it is very suitable for quantitative study. In DPV measurement, staircase waveform superimposes with pulse waves was

introduced to the electrochemical system. With this technique, background capacitive and non-Faradaic current can be effectively removed from the current signal obtained (Zhao et al., 2009).

To establish LcA detection, DPV was measured before and after the functionalized working electrode was incubated with analyte. Final signal was expressed in the change of percentile peak current throughout two DPV measurements (ΔI). Since our rGO and electrodes were prepared in a home-made way, it is reasonable that inter-sample variation could exist, which made using a single DPV peak current as sensing parameter inaccurate. By calculating ΔI , baseline of each individual sample was first established and the change of electrochemical performance of working electrode was extracted. ΔI could represent the LcA cleaving event happened on the surface of working electrode more genuinely and resulted in a more accurate measurement.

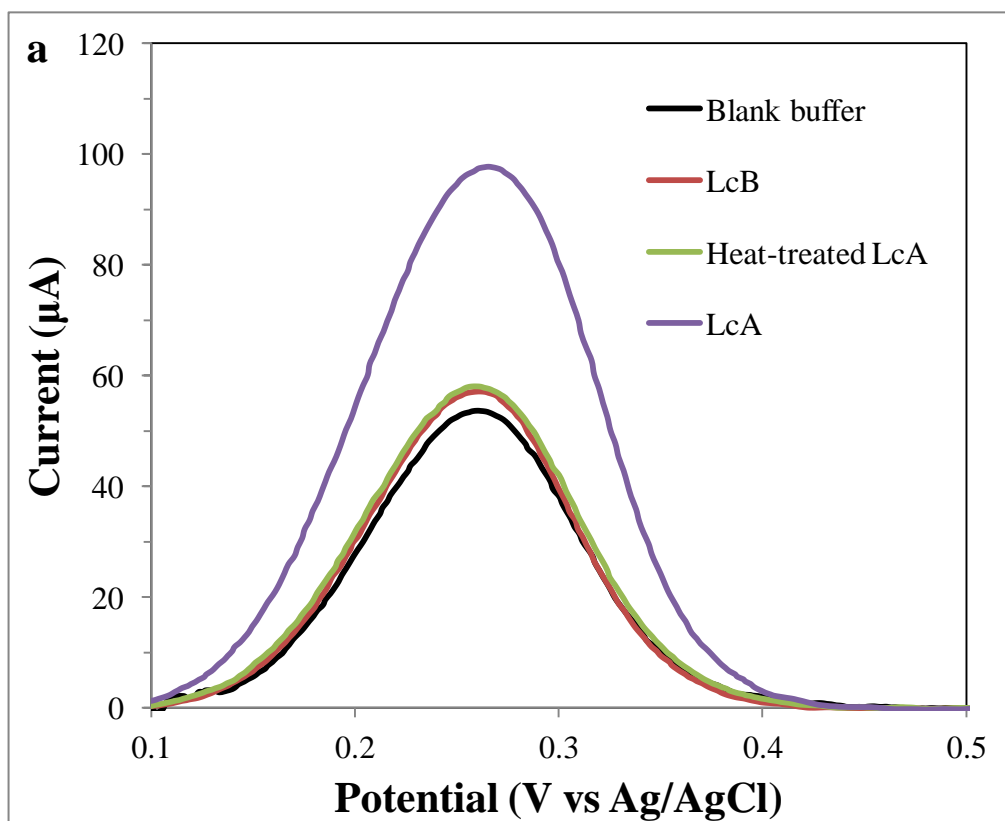
As an initial attempt to evaluate the sensing performance of our prepared working electrode against LcA, the sample was diluted with pure buffer supplemented with Zn^{2+} (10 μM) and DTT (2mM). It is well known that LcA is a Zn^{2+} dependent metalloprotease (Schiavo et al., 1992). Zn^{2+} is crucial for

maintaining the enzymatic activity of LcA and DTT is a common reducing agent used to preserve protein. Figure 4.3.6. a shows DPV curve of a working electrode measured after incubated with different analyte. The curve measured with blank buffer incubation represented the background state of working electrode LcB is botulinum neurotoxin light chain B, which is also one of the BoNT but with a different enzymatic target compare with LcA. Heat-treated LcA was heated in 85 °C for an hour in order to deactivate its enzymatic activity. Fresh LcA is the only one among those four samples with SNAP-25 cleavage activity. From those DPV measurements, we can observe that only after incubated with fresh LcA obviously increased DPV peak current. The increased DPV peak current should be attributed to the cleavage of SNAP-25-GFP immobilized on working electrode by LcA. After incubated with fresh LcA, the SNAP-25-GFP was cleaved and removed in the washing step, which reduced steric hindrance and electrostatic repulsion on the surface of working electrode. When the protein covering the working electrode was partially removed and the charge density was decreased, redox probes became easier to approach the working electrode surface and perform heterogeneous charge transfer. This increased of redox activity on the surface of working electrode enhanced the DPV current measured from the working electrode after incubation with fresh LcA. The other curves measured

after incubate with LcB and heat-treated LcA did not increase the peak current in DPV. Although LcB was active, it did not have any enzymatic activity against SNAP-25 and the heat-treated LcA was denatured under high temperature. These samples did not affect the peak current in DPV measurement obviously. Although these non-target samples should not increase DPV current due to their lack of enzymatic cleavage activity against SNAP-25, it was still a concern that passive adsorption of these proteins may decrease the DPV current and affect the accuracy of biosensor. However, empirical result suggested that passive adsorption did not occur since the DPV signal was not decreased. It can be concluded that the washing step where detergent (0.5 % Tween-20) was introduced was effective in removing passive adsorption of other non-target biomolecules.

Figure 4.3.6. b. shows the relative DPV peak current change (ΔI) after incubated with different analyte. The LcB, heat-treated LcA and fresh LcA concentration were both 1 ng/mL and each condition was repeated with three individual samples. The ΔI of working electrode measured after incubated with blank buffer (noise), LcB and heat-inactivated LcA were $2.32 \pm 1.47 \%$, $4.93 \pm 5.47 \%$, $8.43 \pm 6.54 \%$ respectively. The LcB and heat-inactivated LcA did not increase ΔI very

much. However, fresh LcA greatly increased ΔI by 61.15 ± 8.65 %. It can be concluded that the electrochemical biosensor for LcA activity detection was successfully fabricated. Neither the non-target LcB nor the heat-inactivated LcA were able to recover DPV signal. Our electrochemical biosensor was able to specially response to active LcA only while having little interference from other analyte that have no enzymatic activity against SNAP-25. Thus, the increased DPV signal was able to genuinely represent the presence of active LcA in the analyte.



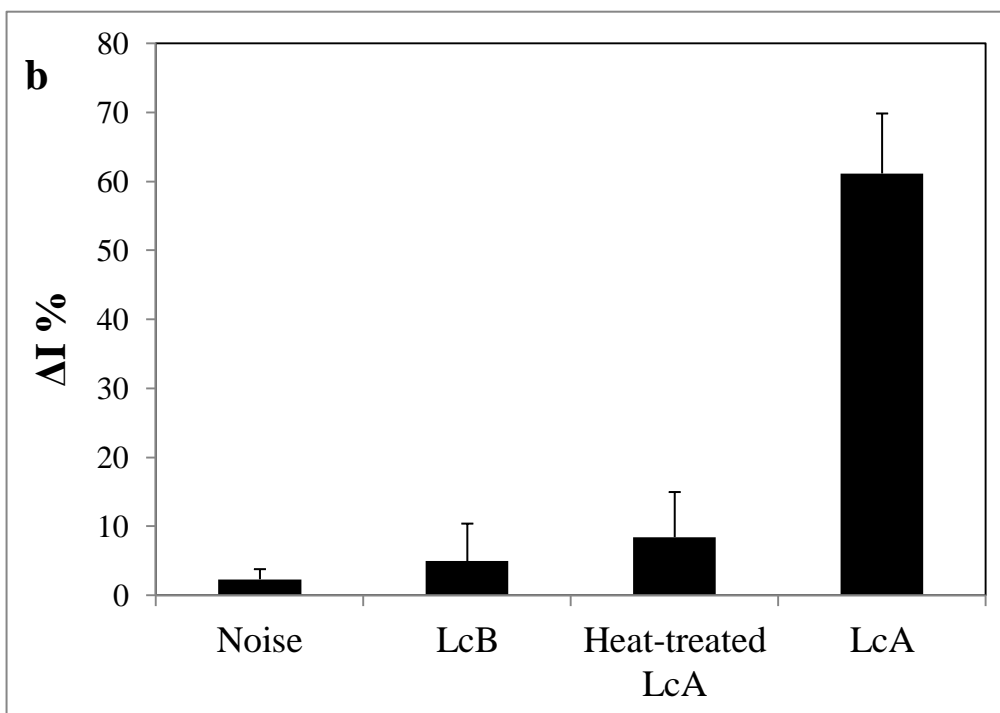


Figure 4.3.6. (a) Differential pulse voltammograms of Au/rGO/PA/SNAP-25-GFP treated with blank buffer, LcB (1 ng/mL), heat-treated LcA (1 ng/mL) and fresh LcA (1 ng/mL). DPV measurements were performed in 1X PBS supplemented with 5 mM $[\text{Fe}(\text{CN})_6]^{3-/4-}$ (1:1) and 100 mM KCl (b) Histogram showing the DPV peak current change (ΔI) before and after different sample incubation (n=3) (Adopted from Chan et al., 2015).

4.3.7. Limit of detection (LOD) against LcA

After our electrochemical biosensor was proved to be specific and able to detect fresh LcA, its detection limit was further studied by incubating working electrode with various concentration of LcA in pure buffer. Figure 4.3.7. a shows a plot of sensor response (ΔI) against various concentration of LcA (2.5 pg/mL, 7.5 pg/mL, 10 pg/mL, 25 pg/mL, 50 pg/mL, 100 pg/mL, 500 pg/mL and 1000 pg/mL). It was found that 2.5 pg/mL LcA barely created any response and there was no observable change in ΔI . As the concentration of LcA increased from 2.5 pg/mL to

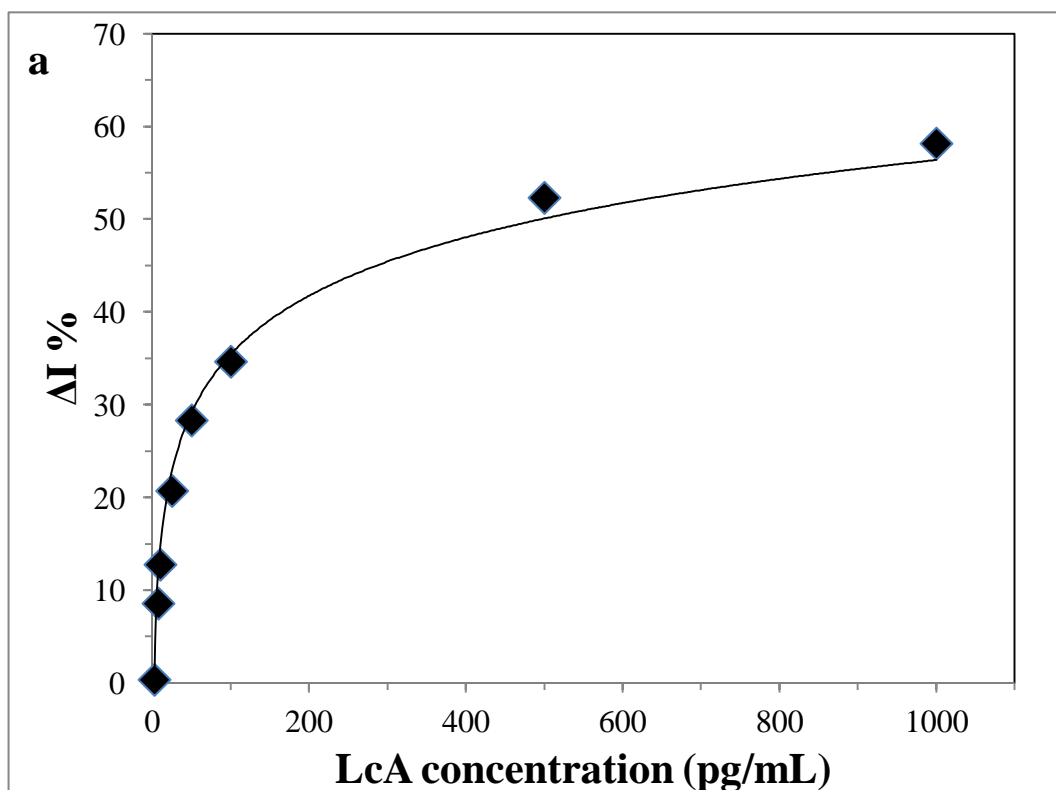
1000 pg/mL, ΔI gradually increased from 0.33 % to 58.13 %. The increased concentration of LcA should increase the SNAP-25 cleavage rate. When more and more SNAP-25-GFP was cleaved and removed, negative charge density and steric hindrance on working electrode decreased gradually. These effects both increased the accessibility of redox probes to the working electrode surface and increased the ΔI measured by DPV. When LcA concentration increased from 500 pg/mL to 100 pg/mL, ΔI (from 52.29 to 58.13) did not increase as obvious as the other concentration intervals. It is probably due to the fact that LcA started to saturate and most of the SNAP-25-GFP immobilized on working electrode was cleaved. Further increasing LcA concentration cannot remove anymore probe protein from working electrode surface and it hardly increased ΔI in DPV measurement.

The trend of ΔI increment against LcA concentration did not fit well with a standard linear regression model. Figure 4.3.7. b fitted ΔI with the logarithm of LcA concentration (in pg/mL) and a good correlation was found. When LcA concentration increased from 2.5 pg/mL to 1000 pg/mL, the linear equation of sensor response is $\Delta I \% = 9.0945 \ln(\text{LcA concentration}) - 6.4527$ with $R^2 = 0.9802$. The relationship between ΔI and LcA concentration agreed with other reports, which BoNT/A activity was studied and sensor response was linear to the

logarithm of BoNT/A concentration (Bagramyan et al., 2008, Frisk et al., 2008, Stevens et al., 2013). This non-linear relationship between ΔI and LcA concentration was probably due to the fact that active LcA could not only cleave one single SNAP-25. Being an enzyme, a LcA molecule could cleave multiple SNAP-25 until its enzymatic activity was lost. Interestingly, for the biosensors proposed to detect LcA using immunoassay, sensor response was directly linear to the concentration of toxin (Bok et al., 2013). In this type of immunoassay biosensor, each LcA captured a single antibody with reporter probe leading to one transduction event. Generally, it can be concluded that for biosensor using immunoassay to recognize LcA gives a linear relationship between sensor response and LcA concentration, while for the one that detects the enzymatic activity of LcA, biosensors response linearly to the logarithm of LcA concentration. As our proposed biosensor fitted to the later categories, fitting a linear regression for ΔI with the logarithm of LcA concentration should reflect the event happening on working electrode more genuinely.

In order to obtain LOD of our electrochemical biosensor, noise level was established. The noise level was measured with incubating working electrode with blank buffer and obtaining the corresponding ΔI and this experiment was repeated

for five times. Final noise level was calculated by averaging individual noise plus three times of its standard deviation (noise +3 SD), which is $\Delta I \% = 11.17 \%$. Fitting noise level with the correlation between ΔI and LcA concentration, the LOD was calculated to be 5.27 pg/mL. Our proposed electrochemical biosensor for the detection of LcA was found to be having a low detection limit with a wide dynamic range, ranged from 2.5 pg/mL to 1000 pg/mL.



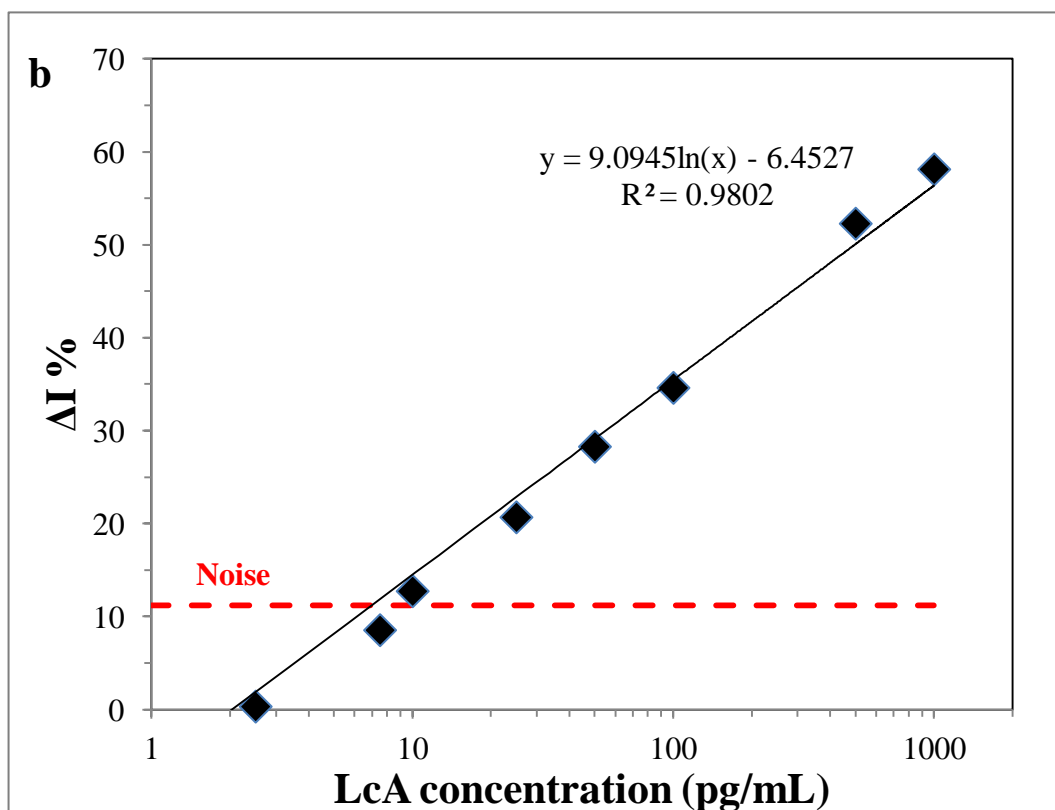


Figure 4.3.7. (a) Calibration curve for the change in DPV current ($\Delta I\%$) at different LcA concentration. (b) calibration curve plot for $\Delta I\%$ vs. log LcA concentration (in pg/mL). Noise level was established by incubating with blank buffer and calculated by its mean + 3 SD ($n = 5$).

4.3.8. Stability of the electrochemical LcA biosensor

Besides the specificity and detection limit, stability is another important parameters that has to be addressed for a biosensor. Here, the functionalized working electrode was incubated with blank buffer for one hour and measured by DPV scanning and this procedure was repeated for seven times. The goal was to investigate whether there are any deterioration in the electrochemical performance of electrode or if the immobilized detection probe (SNAP-25-GFP) was detached in the incubation or washing steps.

Figure 4.3.8. a shows the DPV curves of a working electrode measured after incubated with buffer for different times (from one times to seven times). Through all measurements, there were no obvious changes in peak position or peak current. In figure 4.3.8. b, peak current of different measurement was standardized by the DPV peak current of the first measurement while the first measurement was standardized as 1. After seven measurements, the relative peak current in DPV was only slightly deteriorated to 0.87. It suggested a good stability of our electrochemical biosensor with little deterioration. More importantly, this empirical result suggested that the probe protein (SNAP-25-GFP) immobilized did not detached from the electrode surface. If the immobilization process was not reliable and it was detached from the working electrode surface, the DPV current should not decreased. Instead, the DPV peak current should be increased since the steric hindrance and electrostatic repulsion should be decreased. Here, the slight decrement of DPV peak current in our stability test ruled out the possibility of probe detachment and suggested a good stability of working electrode

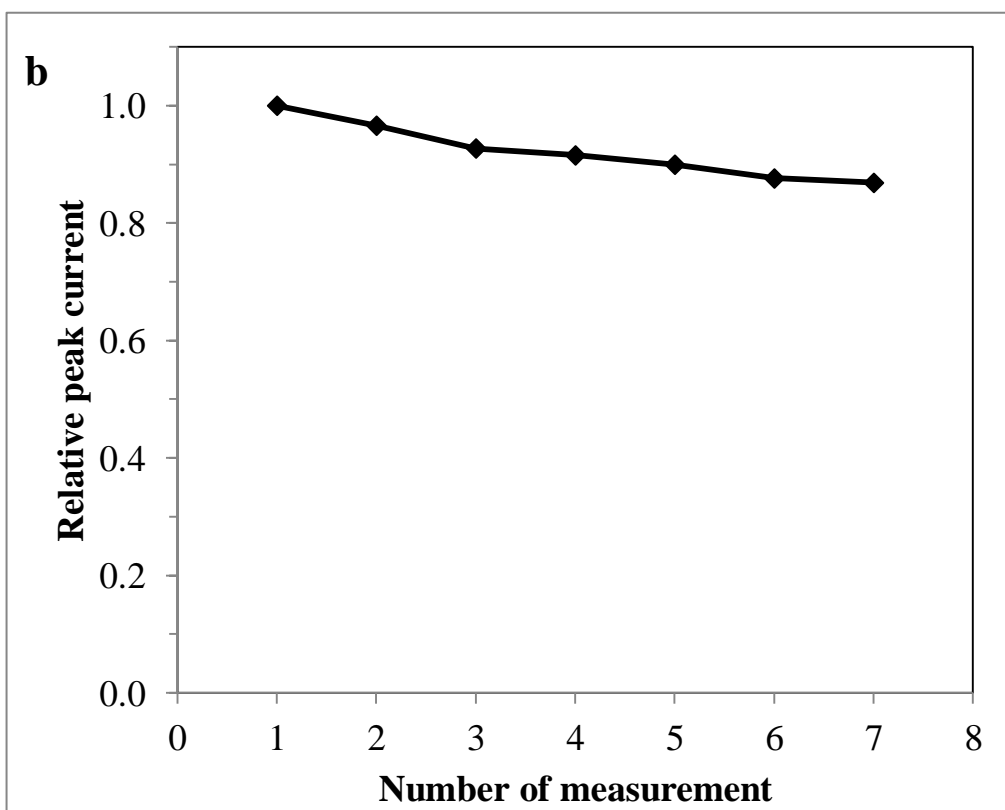
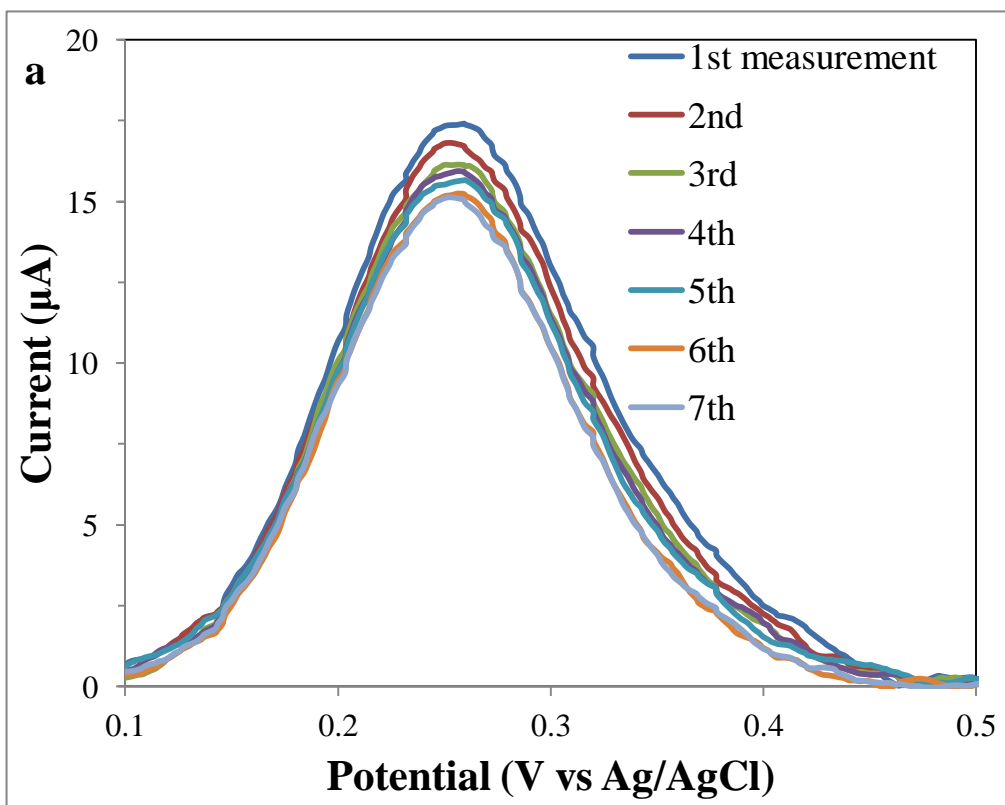


Figure 4.3.8. (a) DPV curves of functionalized working electrode measured after incubated with blank buffer. The same working electrode was repeated with the

same experiment for seven times. **(b)** Relative DPV peak current at different measurements. All DPV peak current was standardized by the first measurement.

4.3.9. Interference effect of milk sample

BoNT/A is a food bond pathogen and it usually infects patients via ingestion of improperly handled food. As a BoNT/A biosensor it would be desirable that it is able to work under a complex environment, i.e. food extract. If this complex environment provides little interference on the biosensor, further treatment of the sample including centrifugation, filtering can be minimalized and the overall detection time and cost can be reduced. When operate under a raw extract of food, there could be many unpredictable factors that will interfere with the sensing mechanism. For example, auto-fluorescence in food extract that affects a fluorescence biosensor, chromophore or colored food additives that may affect a colorimetric biosensor or even passivate adsorption of macromolecules on electrode surface that may severely ruin an electrochemical biosensor or a FET biosensor. Even worst, signal obtained was merely caused by the fluctuation caused by interference of non-target species, which resulted in false negative or false positive results (Shehada et al., 2012, Wang et al., 2014). In order to address this issue, fresh BoNT-LcA was injected into skimmed milk purchased from a conventional supermarket, mimicking BoNT/A contaminated milk, which may

actually be found in real life.

Figure 4.3.9. shows the sensor response (ΔI) of our biosensor against various concentration of LcA (0 pg/mL, 1 pg/mL, 5 pg/mL, 10 pg/mL, 50 pg/mL, 100 pg/mL) dispersed in pure buffer or skimmed milk. From the response of 0 pg/mL, it showed that pure skimmed milk did not induce any obvious response to the biosensor. Unlike buffer, skimmed milk has a very complicated content including lipids, proteins, salts, minerals and vitamins. These components may interact with our working electrode in a non-specific way, for example, passive adsorption. However, this potential problem seemed not be playing any significant role in affecting the biosensor. After each time the working electrode was incubated with analyte, it underwent rigorous washing steps. With the aid of surfactant, it was very effective in removing nonspecific adsorbed molecules on working electrode. With little non-specific adsorption left behind, skimmed milk did not pose any observable changes to the electrochemical-sensing signal and almost no interference was found. The fluctuation caused by a real sample (milk) seemed minimal.

Besides of the sensor irresponsiveness from the complex molecular environment

in skimmed milk, results indicated that LcA could be detected even if it is presented in milk. In Figure 4.3.9, ΔI rised with the concentration of LcA, no matter it is in pure buffer or milk. However, LcA in milk generally created slightly lesser response, compared with the same concentration of LcA but in pure buffer environment. The slightly decreased sensor response can be explained by two reasons. Firstly, when LcA was suspended in milk, it is possible that the solution did not provide an optimal environment for LcA to perform its enzymatic activity. The variance in pH, enzyme cofactor or even the present of competitor could possibly affect the sensor's detection against LcA proteolytic activity. Secondly, the abundant macromolecules in skimmed milk may compete with LcA to be adsorbed on working electrode surface. This competition may decrease the SNAP-25 cleavage efficient of LcA and thus resulted in a lesser ΔI . Despite all those factors, our sensor was able to detect LcA suspended in milk and interference created by skimmed milk was found to be minimal.

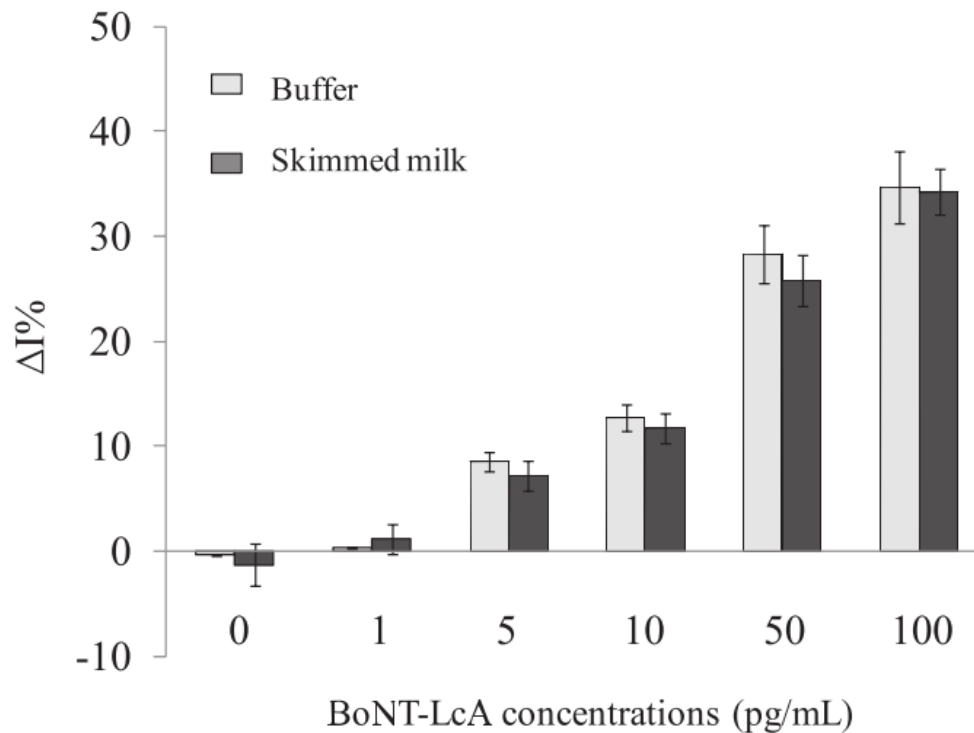


Figure 4.3.9. Comparison of our electrochemical biosensor response against various concentration of LcA in pure buffer or skimmed milk samples (Adopted from Chan et al., 2015).

4.4. Summary

The rGO-based electrochemical sensor fabrication and functionalization process was characterized by TEM, UV-Vis, XPS, Raman spectroscopy and FTIR. Afterward, effects of functionalization processes on the electrochemical behavior of working electrode were further characterized by CV and EIS. The relative change of DPV peak current (ΔI) in DPV was used as an indicator of sensor response, which could reduce the inter-sample variance. This suggested detection method achieved a very good LOD of 5.27 pg/mL LcA with wide dynamic range,

up to 1000 pg/ml. The system was found to be very specific which react to active LcA only, but not the heat-inactivated LcA nor LcB. Repeated measurements and rigorous washing steps neither created observable damage to the electrochemical behavior of the sensor. Interference study of injecting LcA into skimmed milk suggested a real-life mimicking complex protein environment created minimal interference on the sensor's performance.

Chapter 5 Discussion

5.1. Reduced graphene oxide transistor with extended DNA capture probe for DNA Detection

Using graphene-based material for FET biosensing DNA has been widely reported but how the probe immobilization approach could affect the biosensor was rarely studied. In this project, a long capture probe immobilized via π - π stacking was suggested and it was compared with other conventional probe immobilization approaches.

5.1.1. Affinity of ssDNA-graphene and ds-DNA-graphene

π - π stacking DNA capture probe on graphene has been widely in graphene-based biosensors. π - π stacking is a non-covalent attraction force between aromatic rings. Nucleobases in DNA and the graphene giant covalent structure both contain abundant π electrons that facilitated DNA to be self-assembled on graphene. Separation between a single nucleobase and the graphene it stacked on is estimated to be about 3.5 Å (Gowtham et al, 2007).

Although there are many proposed interaction forces between DNA and graphene besides π - π stacking, including hydrogen bonding, electrostatic interaction, van der Waal forces and hydrophobic interaction, the π - π stacking remained as the major interaction mechanism (Akca et al., 2011, Gowtham et al, 2007). In order to study the adsorption process of both ssDNA and dsDNA on the surface of graphene, Zeng et al., performed molecular simulation to simulate the adsorption at atomic level (Figure 5.1.1.). In fact, ssDNA is a very flexible structure and it can eventually lie flat on the surface of graphene (Manna et al., 2013, Zeng et al., 2015). In contrast, dsDNA can only be adhered on graphene vertically with little contact area. The van der Waals energy in the dsDNA-graphene system is much smaller than the ssDNA-graphene one, indicating dsDNA adsorption on graphene is relatively thermodynamically unfavorable (Zeng et al., 2015). dsDNA is often described as a “rigid structure” that it can hardly be bended and the double helical structure can hardly be opened (Mills et al., 2004). Since π - π stacking is a short-range interaction, nucleobases protected in the helical structure of dsDNA cannot stack with the hydrophobic domain in graphene thus dsDNA has a lower affinity with graphene, comparing with ssDNA. The low affinity between dsDNA and graphene is the key reason that after hybridization, fully complementary

capture probe originally immobilized on the surface of graphene detaches into solution phase. The long capture probe design suggested in chapter 2 solved this problem by retaining a single-stranded sequence after hybridization in order to maintain the π - π stacking interaction force.

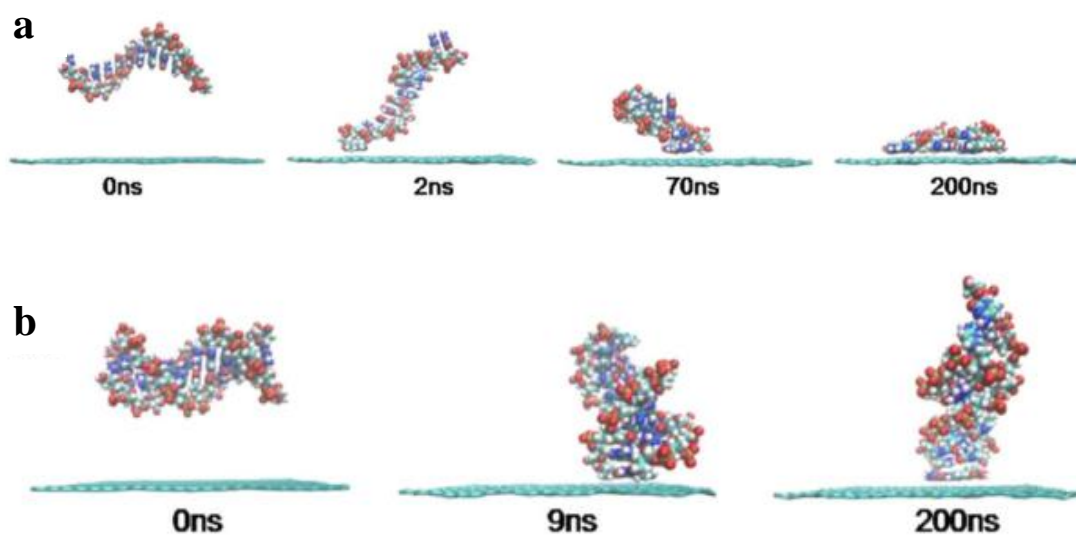


Figure 5.1.1. The trajectories of (a) ssDNA and (b) dsDNA absorbing on graphene

(Adopted from Zeng et al., 2007).

5.1.2. Length of the single-stranded sequence in the long capture probe

In the long capture probe designed in chapter 2, there are two regions: a.) a complementary region for target capture and b.) a single-stranded region for π - π stacking immobilization. The former region is defined by length of target DNA (18

base pairs) and the later region was designed as 30 base pairs. Here, the length of the single-stranded region in long capture probe was chosen by considering two reasons.

Firstly, the single-stranded region must not be too short, e.g., one or two base pairs. π - π stacking interaction force between ssDNA and graphene is a reversible bonding and the adhesion strength between ssDNA and graphene depends on the number of base pairs. Each nucleobase in DNA provides π electron to stack with graphene. Thus, a longer ssDNA has a higher affinity with graphene and it is possible for it to displace a shorter ssDNA from graphene (Zhao et al., 2011, He et al., 2014). In order to immobilize the long capture probe stably, the length of the single-stranded sequence must be greater than 18 base pairs so it will not be displaced by target DNA or other oligonucleotide in the analyte.

Secondly, the single-stranded region should not be too long. The single-stranded region is expected to lie on the surface of graphene. Each extra nucleobase in the single-stranded region occupy extra vacancy of the graphene FET channel. In consequence, a longer long capture probe leads to a lower probe density on the graphene. In a solid-state biosensor, probe density on the surface of the

transduction element is the key factor determining the ability of the immobilized probe to capture target dispersed in analyte. Higher probe density immobilized on a transducer surface could lead to a higher sensing sensitivity and a higher upper-limit of detection (Hu et al., 2014).

Although increasing the length of single-stranded region in the long capture probe could increase the probe stability, it is indeed sacrificing sensing performance including sensitivity and dynamic range. To balance these factors, we opted a length of the single-stranded sequence in the long capture probe that is long enough to avoid non-specific displacement but not too long in order to preserve high probe density on the surface of graphene, which was 30 base pairs.

5.2. Chemical vapor deposition grown graphene DNA field-effect transistor biosensor with gold nanoparticles signal amplification

In the previous section, different probe immobilization strategies were compared and a graphene-based bioFET using long capture probe was established. Although the long capture probe functionalized bioFET was found to be sensitive and stable. In this follow up study, two major amendments were made to the sensing setup in

order to improve the bioFET performance: a.) FET channel was switched from rGO to high quality CVD graphene and b.) reporter probe-AuNPs signal amplification was applied to co-hybridize with target cDNA, enhancing the LOD.

5.2.1. Size of AuNPs on the effect of signal amplification

Reporter probe-AuNPs in 15 nm and 30 nm was applied to enhance the V_{CNP} shift in the detection of H7 target correspondingly. 30 nm AuNPs were having a higher surface area compared with the 15 nm one. Assuming all the AuNPs were perfect sphere, their surface area can be calculated by $A = 4\pi r^2$, to which the surface area of a 30 nm AuNP is 4 times larger than the 15 nm one. With a greater surface area, the number of reporter probe loaded on a 30 nm AuNP was expected to be roughly 4 times more than a 15 nm AuNP. Assuming each H7 target captured on the CVD graphene surface was able to capture one reporter probe-AuNP, 30 nm AuNPs brought more negative charge to the proximity of graphene compared with the 15 nm AuNPs. The 30 nm reporter probe-AuNPs increased the charge density on the surface of graphene more effectively leading to a more sensitive DNA detection platform. Yet, the lowest LOD of graphene-based bioFET for DNA detection was 100 fM by using PNA as capturing probe and our setup surpassed it (Cai et al.,

2014)

5.2.2. FET sensing beyond Debye's length

In a high salt concentration environment, the Debye's screening length usually falls below 10 nm. Any charge located beyond the Debye's screening length from the proximity of FET channel in principle should not result in any change on the FET channel and it is an important concern for using 30 nm reporter-probe AuNPs for signal amplification purpose. However, there was a recent study overthrown this principle by showing that when the bioFET operated in solution-gate, FET channel was able to react with charged molecules captured 30 – 40 times of Debye's screening length (20 – 30 nm) (Palazzo et al., 2015). The capacitive layer generated by the outmost layer of charged molecules, which “remotely” gated the FET channel, explained this unexpected observation. On this ground, the 30 nm reporter probe-AuNPs were able to provide better electrostatic gating effect on CVD graphene FET channel.

5.2.3. Choosing AuNPs as reporter probe carrier

In this section, AuNPs was chosen as the reporter probe carrier. The surface charge of AuNPs highly depends on the types of ligand conjugated. DNA is a highly negatively charged macromolecule. With reporter probe conjugated on an AuNPs, the surface of reporter probe-AuNPs composites carries negative charge, which can enhance the electrostatic gating effect posed by H7 target on graphene FET channel.

The major benefit of using AuNPs is that by using thiol-modified DNA, it is very easy to create a stable monolayer on the surface of AuNPs by forming gold-sulfur bond (Arvizo et al., 2010). The gold-sulfur bond is well researched and has been widely applied in creating different functional materials (Zhang et al., 2011).

Besides the facile gold-sulfur bond that can be used to functionalize AuNPs, the tunable size of AuNPs (from 1 to 100 nm) is another huge advantages in the application of biosensing (Zhang et al., 2011). Size of AuNPs synthesized by common citrate reduction method can be tuned by simply varying the ratio of reducing agent and HAuCl_4 , changing the type of reducing agent or modifying the synthesis condition (Zhao et al., 2012). The synthesis process of AuNPs usually requires a relatively simple setup and mild condition. Cost of using AuNPs as

reporter-probe carrier is low and it is beneficial in reducing the fabrication cost of a biosensor.

5.3. A rGO-modified gold electrode for ultrasensitive electrochemical detection of botulinum neurotoxin

In the above sections, the capability of graphene-based bioFET in the detection of DNA using long capture probe was well demonstrated. DNA detection plays a very important role in diagnostic, food safety validation and identify of specific organism. However, DNA sometimes fails to provide direct toxicity information of a food product. Protein detection bridges this gap. Protein is the down-stream product of DNA and it is the biomolecules that directly involved in physiological events. Here, a graphene-based electrochemical biosensor detecting the activity of BoNT/s was reported.

5.3.1. Detection mechanism

Our proposed graphene-based electrochemical biosensor for BoNT/A activity detection is a signal-on system. The electrochemical signal of this system

increases when the working electrode exposes to BoNT/A-containing analyte. Increment of electrochemical signal can be explained by the enhanced accessibility of redox probe to the working electrode surface when it encounters BoNT/A.

After biofunctionalization, detection probe (SNAP-25-GFP) immobilized on the working electrode prevents it from accessing the redox probe by two mechanisms: a.) steric hindrance and b.) electrostatic repulsion. SNAP-25-GFP forms a monolayer on the working electrode that physically blocks the redox probe from accessing the electrode and the steric hindrance effect is increased. Besides, isoelectric point of SNAP-25 and GFP are both smaller than the pH of standard buffer uses in electrochemical measurement. Detection probe SNAP-25-GFP carries negative charge during electrochemical measurement, which repels the negatively charged redox probe. When the working electrode encounters BoNT/A, detection probe SNAP-25-GFP is cleaved and the aforementioned repulsion forces are reduced. The effects created by probe immobilization are partially reversed and the DPV signal is then recovered.

5.3.2. Using SNAP-25-GFP instead of SNAP-25 as detection probe

In this project, SNAP-25-GFP was used as detection probe instead of solely SNAP-25. SNAP-25 is the enzymatic cleavage target of BoNT/A. Molecular weight of SNAP-25 is approximately 25 kDa and consists of 206 amino residues (Binz et al, 1994). Cleavage site of BoNT/A locates at glutamine-196 and arginine-197 and it is close to C-terminus. The conventional probe conjugation technique usually binds the N terminus of a biomolecule to graphene. In this case, such setup is unfavorable to the sensing performance since the cleavage induced by BoNT/A only removes a small portion of SNAP-25 from the electrode surface. In order to enhance the contrast upon BoNT/A cleavage, GFP was conjugated to the C-terminus of SNAP-25 by plasmid construction. GFP is green fluorescence protein exists in nature with molecular weight of approximately 30 kDa and it is often being used in studying molecular biology as fluorescence probe (Remington, 2011). Here, GFP was not used as a fluorescence probe but as a signal amplification probe with isoelectric point close to SNAP-25. Under neutral buffer, SNAP-25 and GFP both carry negative charge and repel redox probe. When BoNT/A exists in the analyte, a small residue of SNAP-25 and the whole GFP will be removed from the electrode surface. Contrast before and after BoNT/A

cleavage can thus be enhanced, improving sensing sensitivity.

5.3.3. Compare our proposed electrochemical BoNT/A biosensor with gold standard mouse bioassay

Compared with the current gold standard of BoNT detection, which is mouse bio-assay, this proposed biosensor provided a critical improvement that the sacrifice of animal can be eliminated. Mouse bioassay requires a centralized laboratory and experienced technicians to handle the test, which is expensive and inconvenient. Electrochemical biosensor provides a portable platform for BoNT/A detection and the testing procedure can be very simple. It can eliminate the sensor delivering time by providing the possibility of performing on-site detection. Detection cost and turnover time for performing BoNT/A detection can thus be drastically reduced.

If convert the LOD of our proposed electrochemical biosensor into the weight of BoNT/A (LcA was used in this project, which is the active component in BoNT/A), the LOD is approximately 16 pg/mL BoNT/A. LOD of our proposed system is comparable to the one of mouse bioassay, which is approximately 20 pg/mL

(Shapiro et al., 1998). Also, the detection time of our electrochemical system falls in hours while mouse bioassay requires days to complete the whole test. In summary, our proposed electrochemical biosensor has comparable performance compared with the current gold standard mouse bioassay in BoNT detection. It definitely is a promising candidate for the detection of BoNT/A.

Chapter 6 Conclusion

In the first study (chapter 2), long capture probe immobilization strategy was proposed for graphene-based FET biosensing. Comparing with other conventional probe immobilization strategies (π - π stacking fully complementary short capture probe and covalent immobilization amine-modified short capture probe via PA), long capture probe was very stably immobilized on rGO even after target hybridization. Sensitivity and LOD of rGO-based bioFET using long capture probe was found to be the best. However, the LOD in this bioFET system was not optimal and transfer curve of rGO FET was not measured. Improvements were made in the next chapter.

In order to further improve sensitivity and LOD of graphene-based bioFET for DNA detection, chapter 3 fabricated a CVD graphene-based bioFET using long capture probe to capture target and reporter probe-AuNPs to amplify the electrostatic gating effect created by H7 target. Experimental results demonstrated that sensitivities and LOD of the bioFET were enhanced after reporter probe-AuNPs signal amplification. This graphene bioFET biosensor could achieve LOD as low as 64 fM for avian influenza virus H7 subtype gene detection with

good specificity. Even single-base mismatch target can be discriminated from the fully complementary one. This graphene FET biosensor has the potential to be used for ultrasensitive detection of avian influenza viruses and demonstrated the best LOD in graphene-based bioFET for DNA detection yet reported.

In the final study, a rGO-based electrochemical biosensor for the detection of LcA activity was established. In order to perform electrochemical detection, DPV was chosen due to its superior sensitivity. Over rigorous testing, our proposed electrochemical biosensor was found to respond very specific to the activity of LcA. Neither heat-inactivated LcA nor LcB induced any considerable sensor response. Moreover, this electrochemical biosensor worked in a wide dynamic range (2.5 pg/mL to 1000 pg/mL) with low LOD (5.27 pg/mL) when LcA was diluted in pure buffer. By injecting LcA into skimmed milk in order to mimic real-life sample, little interference was found. This proposed electrochemical biosensor has the feasibility of working under complex protein environment, ensuring its promising future of being operated in real-life.

Chapter 7 Future Works

Graphene-based FET biosensors have been demonstrating its great potential in the past decade. Different FET configurations and fabrication approaches were proposed. Some of the detection method even reached the detection limit of fM (Cai et al., 2014). However, the exact interaction mechanism between DNA and graphene is still unclear. Some of the empirical results and simulations are contradictory. The most concerned issue is that there are reports suggesting DNA adsorption on graphene surface shifted transfer curve of graphene to positive side (Mohanty et al., 2008, Lin et al., 2010, Guo et al., 2011) while the others reported a negative shift (Don et al., 2010, Yin et al., 2012, Chen et al., 2013, Lin et al., 2013, Cai et al., 2014). In fact, there are many possible factors involved in the transfer curve shift after DNA adsorption, for example, ionic strength and pH of the buffer solution, oligonucleotide sequence of DNA, materials of the contact pads, etc. In order to further develop a reliable DNA sensor using graphene-based FET, this issue should be clarified thoroughly.

After developing DNA biosensor using graphene, it would be beneficial to apply the developed technology into protein sensing. Comparing with DNA sensing,

protein sensing can sometimes provide more accurate diagnostic information from a variety of disease, since protein is a down-stream product in translation process. To achieve protein detection, aptamer can be used as a capture probe and amplification probe while using the long capture probe strategies. Aptamer is a sequence of oligonucleotide, which has specific affinity to certain target. Its nature of oligonucleotide allows it to be used in a similar way of conventional DNA capture probe.

A solid and well-performing electrochemical biosensor for detection of BoNT/A was presented in chapter 4, but there are still some directions for us to work on in order to refine the biosensor. Firstly, the Au/rGO was prepared with a drop-casting approach. Drop casting is easy to be achieved but have little control on the film thickness and lateral size. In order to tackle this problem, rGO film can be deposited on Au electrode by other approach including langmuir-blodgett or electrochemical deposition.

Secondly, the working electrode structure presented in this project based on a centimeter sized Au film. By applying micro-fabrication technique, it is possible to shrink the electrode size into micrometer regime and form an array of

electrochemical sensing system. With a micro-array of sensors, multiplex biosensing can be achieved in a palm-sized chip.

References

- Akca, S., Foroughi, A., Frochtzwaig, D., Postma, H.W.C., 2011. PLoS One 12, e18442.
- Alwarappan, S., Erdem, A., Liu, C., Li, C.Z., 2009. J. Phys. Chem. C 113, 8852-8857.
- An, J.H., Park, S.J., Kwon, O.S., Bae, J., Jang, J., 2013. ACS Nano 7, 10563-10571.
- Ang, P.K., Chen, W., Wee, A.T.S., Loh, K.P., 2008. J. Am. Chem. Soc. 130, 14392-14393.
- Arvizo, R., Bhattacharya, R., Mukherjee, P., 2010. Expert Opin. Drug Deliv. 7, 753-763.
- Bae, S., Kim, H., Lee, Y., Xu, X., Park, J., Zheng, Y., Balakrishnan, J., Lei, T., Kim, H. R., Song, Y.I., Kim, Y.J., Kim, K.S., Ozyilmaz, B., Ahn, J.H., Hong, B.H., Iijima, S., 2010. Nat. Nanotechnol. 5, 574-578.
- Bagramyan, K., Barash, J.R., Arnon, S.S., Kalkum, M., 2008. PLoS One 3, e2041.
- Banica, F.G., 2012. What are Chemical Sensors? in Chemical Sensors and Biosensors: Fundamentals and Applications. John Wiley & Sons, Ltd, 1-20.
- Barr, J.R., Kalb, S.R., Pirkle, J.L., 2011. Amer. Chemical. Soc. 1065, 83-97.
- Basavanna, U., Muruvanda, T., Brown, E. W., Sharma, S. K., 2013. Int. J. Microbiol. 2013, 593219.
- Berger, C., Song, Z.M., Li, T.B., Li, X.B., Ogbazghi, A.Y., Feng, R., Dai, Z.T., Marchenkov, A.N., Conrad, E.H., First, P.N., de Heer, W.A., 2004. J. Phys. Chem. B 108, 19912-19916.
- Berger, C., Song, Z.M., Li, X.B., Wu, X.S., Brown, N., Naud, C., Mayou, D., Li, T.B., Hass, J., Marchenkov, A.N., Conrad, E.H., First, P.N., de Heer, W.A., 2006. Science 312 1191-1196.
- Bergveld, P., 1970. IEEE Trans. Biomed. Eng. 70-71.
- Binz, T.J., Blasi, S., Yamasaki, A., Baumeister, E., Link, T.C., Sudhof, R., Jahn,

- R., Niemann, H.J., 1994. *Biol. Chem.* 269, 1617–1620.
- Bok, S., Korampally, V., Darr, C.M., Folk, W.R., Polo-Parada, L., Gangopadhyay, K., Gangopadhyay, S., 2013. *Biosens. Bioelectron.* 41, 409-416.
- Bonaccorso, F., Colombo, L., Yu, G., Stoller, M., Tozzini, V., Ferrari, A.C., Ruoff, R.S., Pellegrini, V., 2015. *Science* 347, 1246501.
- Bonanni, A., Loo, A.H., Pumera, M., 2012. *Trends Anal. Chem.* 37, 12-21.
- Bonanni, A., Pumera, M., 2011. *ACS Nano* 5, 2356-2361.
- Brand, U., Reinhardt, B., Ruther, F., Scheper T., Schugerl, K., 1991. *Sens. Actuator B-Chem.* 4, 315-318.
- Brownson, D.A., Banks, C.E., 2012. *Phys. Chem. Chem. Phys.* 14, 8264-8281.
- Cai, B., Wang, S., Huang, L., Ning, Y., Zhang, Z., Zhang, G., J., 2014. *ACS Nano* 8, 2632-2838.
- Caras, S., Janata, J., 1980. *Anal. Chem.* 52, 1935-1937.
- Casiraghi, C., Hartschuh, A., Qian, H., Piscanec, S., Georgi, C., Fasoli, A., Novoselov, K.S., Basko, D.M., Ferrari, A.C., 2009. *Nano Lett.* 9, 1433-1441.
- Chan, C.Y., Guo, J., Sum, C., Tsang, M.K., Tian, F., Hao, J., Chen, S., Yang, M., 2015. *Sens. Actuator B-Chem.* 220, 131-137.
- Chen, T.Y., Phan, T.K.L., Hsu, C.L., Lee, Y.H., Wang, J.T.W., Wei, K.H., Lin, C.T., Li, L.J., 2013. *Biosens. Bioelectron.* 41, 103-109.
- Ciesielski, A., Samori, P., 2014. *Chem. Soc. Rev.* 43, 381-398.
- Clark, Jr L.C., Lyons, C., 1962. *Ann. N. Y. Acad. Sci.* 102, 29-45.
- Cohen-Karni, T., Qing, Q., Li, Q., Fang Y., Lieber, C.M., 2010. *Nano Lett.* 10, 1098–1102.
- Daniels, J.S., Pourmand, N., 2007. *Electroanalysis* 19, 1239-1257.
- Das, A.K., Srivastav, M., Layek R.K., Uddin, M.E., Jung, D., Kima, N.H., Lee, J.H., 2014. *J. Mater. Chem. A* 2, 1332-1340.
- DasGupta, B. R., Foley, J. Jr., 1989. *Biochimie*, 71, 1193-1200.

Dong, X.C., Shi, Y., Huang, W., Chen, P., Li, L.J., 2010. *Adv. Mater.* 22, 1649-1653.

Dong, X.C., Huang, W., Chen, P., 2011. *Nanoscale Res. Lett.* 6, 60-66.

Farah, A.M., Thema, F.T., Dikio, E.D., 2012. *Int. J. Electrochem. Sci.* 7, 5069-5083.

Foran, P.G., Mohammed, N., Lisk, G.O., Nagwaney, S., Lawrence, G.W., Johnson, E., Smith, L., Aoki, K.R., Dolly, J.O., 2003. *J. Biol. Chem.* 278, 1363-1371.

Frisk, M.L., Berthier, E., Tepp, W.H., Johnson, E.A., Beebe, D.J., 2008. *Lab Chip* 8, 1793-1800.

Fu, W., Nef, C., Knopfmacher, O., Tarasov, A., Weiss, M., Calame, M., Schönenberger, C., 2011. *Nano Lett.* 11, 3597-3600.

Fu., C.J., Zhao G.G., Zhang, H.J., Li, S.A, 2013. *Int. J. Electrochem. Sci.* 8 6269-6280.

Gao, R., Cao, B., Hu, Y., Feng, Z., Wang, D., Hu, W., Chen, J., Jie, Z., Qiu, H., Xu, K., 2013. *N. Engl. J. Med.* 368, 1888-1897.

Geim, A.K., Novoselov, K.S., 2007. *Nat. Mater.* 6, 183-191.

Georgakilas, V., Otyepka, M., Bourlinos, A.B., Chandra, V., Kim, N., Kemp, K.C., Hobza, P., Zboril, R., Kim, K.S., 2012. *Chem. Rev.* 11, 6156-6214.

Gill, D.M., 1982. *Microbiol. Rev.* 46, 86-94.

Grieshaber, D., MacKenzie, R., Vörös, J., Reimhult, E., 2008. *Sensors* 8, 1400-1458.

Gowtham, S., Scheicher, R.H., Ahuja, R., Pandey, R., Kama, S.P., 2007. *Phys. Rev. B* 76, 033401.

Guan, J.G., Miao, Y.Q., Zhang, Q.J., 2004. *J. Biosci. Bioeng.* 97, 219-226.

Guo, S.R., Lin, J., Penchev, M., Yengel, E., Ghazinejad, M., Ozkan, C.S., Ozkan, M., 2011. *J. Nanosci. Nanotechnol.* 11, 5258-5263.

He, Q., Sudibya, H.G., Yin, Z., Wu, S., Li, H., Boey, F., Huang, W., Chen, P., Zhang, H., 2010. *ACS Nano* 4, 3201-3208.

He, Y., Jiao, B., Tang, H., 2014. RSC Adv. 4, 18294-18300.

Heller, I., Chatoor, S., Männik, J., Zevenbergen, M.A., Dekker, C., Lemay, S.G., 2010. J. Am. Chem. Soc. 132, 17149-17156.

Hernandez, F.J., Ozalp, V.C., 2012. Biosensors 2, 1-14.

Hoffmann, B., Harder, T., Starick, E., Depner, K., Werner, O., Beer, M., 2007. J. Clin. Microbiol. 45, 600-603.

Holzinger, M., Goff, A.L., Cosnier, S., 2014. Front. Chem. 2, 63.

Hu, S., Zhao, Y., Qin, K., Retterer, S.T., Kravchenko, I.I., Weiss, S.M., 2014, ACS Photonics 1, 590-597.

Huang, P.J.J., Liu, J.W., 2012. Small 8, 977-983.

Huang, Y., Dong, X., Shi, Y., Li, C. M., Li, L.J., Chen, P., 2010. Nanoscale, 2, 1485-1488.

Hummers Jr W.S., Offeman R.E., 1958. J. Am. Chem. Soc. 80, 1339.

Hvistendahl, M., Normile, D., Cohen, J., 2013. Science, 340, 414-415.

Janata, J., Moss, S.D., 1976. Biomed. Eng. 6, 240-245.

Jang, H.D., Kim, S.K., Chang, H., Roha, K.M., Choi, J.W., Huang, J., 2012. Biosens. Bioelectron. 38, 184-188.

Jones, R.G., Ochiai, M., Liu, Y., Ekong, T., Sesardic, D., 2008. J. Immunol. Methods. 329, 92-101.

Kang, X., Wang, J., Wu, H., Aksay, I.A., Liua, J., Lin, Y., 2009. Biosens. Bioelectron. 2009, 25, 901-905.

Karimi, H., Yusof, R., Rahmani, R., Hosseinpour, H., Ahmadi, M.T., 2014. Nanoscale Res. Lett. 9, 71.

Kergoat, L., Piro, B., Berggren, M., Horowitz, G., Pham, M.C., 2012. Anal. Bioanal. Chem. 402, 1813-1826.

Khan, U., Porwal, H., O'Neill, A., Nawaz, K., May, P., Coleman, J.N., 2011. Langmuir 27, 9077-9082.

- Kudin, K. N., Ozbas, B., Schniepp, H. C., Prud'homme, R. K., Aksay, I. A., Car, R., 2008. *Nano Lett.* 8, 36-41.
- Kuila, T., Bose, S., Khanra, P., Mishra, A.K., Kim, N.H., Lee, J.H., 2011. *Biosens. Bioelectron.* 26, 4637-4648.
- Kwon, O.S., Park, S.J., Hong, J.Y., Han, A.R., Lee, J.S., Lee, J.S., Oh, J.H., Jang, J., 2012. *ACS Nano* 6, 1486-1493.
- Lafkioti, M., Krauss, B., Lohmann, T., Zschieschang, U., Klauk, H., Klitzing, K.V., Smet, J.H., 2010. *Nano Lett.* 10, 1149-1153.
- Lee, C.S., Kim, S.K., Kom, M., 2009. *Sensors* 9, 7111-7131.
- Li, D., Muller, M.B., Gilje, S., Kaner, R.B., Wallace, G.G., 2008. *Nat. Nanotechnol.* 3, 101-105.
- Li, X.S., Cai, W.W., An, J.H., Kim, S., Nah, J., Yang, D.X., Piner, R., Velamakanni, A., Jung, I., Tutuc, E., Banerjee, S.K., Colombo, L., Ruoff, R.S., 2009. *Science* 324, 1312-1314.
- Lin, C.T., Loan, P.T.K., Chen, T.Y., Liu, K. K., Chen, C.H., Wei, K.H., Li, L.J. 2013. *Adv. Funct. Mater.* 23, 2301-2307.
- Lin, C.W., Wei, K.C., Liao, S.S., Huang, C.Y., Sunc, C.L., Wua, P.J., Lu, Y.J., Yang, H.W., Ma, C.C., 2015. *Biosens. Bioelectron.* 67, 431-437.
- Lin, C.Y., Lu, C.C., Yeh, C.H., Jin, C., Suenaga, K., Chiu, P.W., 2012. *Nano Lett.* 12, 414-419.
- Lin, J., Teweldebrhan, D., Ashraf, K., Liu, G., Jing, X., Yan, Z., Li, R., Ozkan, M., Lake, R.K., Balandin, A.A., Ozkan, C.S., 2010. *Small*, 6, 1150-1155.
- Lin, L., Liu, Y., Tang, L., Li, J., 2011. *Analyst* 136, 4732-4737.
- Lin, W.,J., Liao, C.S., Jhang, J.H., Tsai, Y.C., 2009. *Electrochem. Commun.* 11, 2153.
- Liu, Y.X., Liu, F., Seo, T.S., 2011. *Chem. Commun.* 47, 12149-12151.
- Lu, C.H., Yang, H.H., Zhu, C.L., Chen, X., Chen, G.N., 2009. *Angew. Chem. Int. Ed.* 48, 4785-4787.

Lu, Y., Goldsmith, B.R., Kybert, N.J., Johnson, A.T.C., 2010. *Appl. Phys. Lett.* 97.

Manna, A.K., Pati, S.K., 2013. *J. Mater. Chem. B* 1, 91-100.

Mannoor, M.S., Tao, H., Clayton, J.D., Sengupta, A., Kaplan, D.L., Naik, R.R., Verma, N., Omenetto, F.G., McAlpine, M.C., 2012. *Nat. Commun.* 3, 763.

Mao, S., Lu, G., Yu, K., Bo, Z., Chen, J., 2010. *Adv. Mater.* 22, 3521-3526.

Mao, S., Yu, K., Lu, G., Chen, J., 2011. *Nano Res.* 4, 921-930.

Mao, X.W., Rutledge, G.C., Hatton, T.A., 2014. *Nano Today* 9, 405-432.

Mills, J.B., Hagerman, P.J., 2004. *Nucleic Acids Res.* 2, 4055-4059.

Mohanty, N., Berry, V., 2008. *Nano Lett.* 8, 4469-4476.

Monne, I., Ormelli, S., Salviato, A., Battisti, C.D., Bettini, F., Salomoni, A., Drago, A., Zecchin, B., Capua, I., Cattoli, G. 2008. *J. Clin. Microbiol.* 46, 1769-1773.

Moser, J., Barreiro, A., Bachtold, A., 2007. *Appl. Phys. Lett.* 91, 163513.

Myung, S., Solanki, A., Kim, C., Park, J., Kim, K.S., Lee, K.B., 2011. *Adv. Mater.* 23, 2221-2225.

Novoselov, K.S., Fal'ko, V.I., Colombo, L., Gellert, P.R., Schwab, M.G., Kim, K., 2012. *Nature* 490, 192-200.

Novoselov, K.S., Jiang, D., Schedin, F., Booth, T.J., Khotkevich, V.V., Morozov, S.V., Geim, A.K., 2005. *Proc. Natl. Acad. Sci. U. S. A.* 102, 10451-10453.

Ohno, Y., Maehashi, K., Matsumoto, K., 2010. *J. Am. Chem. Soc.* 132, 18012-18013.

Ohno, Y., Okamoto, S., Maeshashi, K., Matsumoto, K., 2013. *Jpn. J. Appl. Phys.* 52, 10107.

Ohno, Y., Maehashi, K., Yamashiro, Y., Matsumoto, K., 2009. *Nano Lett.* 9, 3318-3322.

Ou, J.F., Wang, J.Q., Liu, S., Mu, B., Ren, J.F., Wang, H.G., Yang S.R., 2010. *Langmuir* 26, 15830-15836.

Palazzo, G., Tullio, D.D., Magliulo, M., Mallardi, A., Intranuovo, F., Mulla, M.Y.,

Favia, P., Vikholm-Lundin, I., Torsi, L., 2015. *Adv. Mater.* 27, 911-916.

Park, J., Nguyen, H.H., Woubit, A., Kim, M., 2014. *Appl. Sci. Convergence Technol.* 23, 61-71.

Park, S., An, J., Potts, J.R., Velamakanni, A., Murali, S., Ruoff, R.S., 2011. *Carbon* 49, 3019-3023.

Parvez, K., Wu, Z.S., Li, R., Liu, X., Graf, R., Feng, X., Müllen, K., 2014. *J. Am. Chem. Soc.* 136, 6083-6091.

Paska, Y., Haick, H., 2012. *ACS Appl. Mater. Interfaces* 4, 2604-2617.

Pei, S., Cheng, H.M., 2012. *Carbon* 50, 3210-3228.

Pei, S., Zhao, J., Du, J., Ren, W., Cheng, H.M., 2010. *Carbon* 48, 4466-4474.

Pei, S., Cheng, H.M., 2012. *Carbon* 50, 3210-3228.

Pembroke, E., Ruan, G.D., Sinitskii, A., Corley, D.A., Yan, Z., Sun Z.Z., Tour, J.M., 2013. *Nano Res.* 6, 138-148.

Palazzo, G., Tullio, D.D., Magliulo, M., Mallardi, A., Intranuovo, F., Mulla, M.Y., Favia, P., Vikholm-Lundin, I., Torsi, L., 2015. *Adv. Mater.* 27, 911-916.

Rappuoli, R., Pizza, M., Douce, G., Dougan, G., 1996. *Adv. Exp. Med. Biol.* 397, 55-60.

Remington, S.J., 2011. *Protein Sci.* 20, 1509-1519.

Schiavo, G., Rossetto, O., Santucci, A., DasGupta, B. R., Montecucco, C., 1992. *J. Biol. Chem.* 267, 23479-23483.

Schniepp, H.C., Li, J.L., McAllister, M.J., Sai, H., Herrera-Alonso, M., Adamson, D.H., Prud'Homme, R.K., Car, R., Saville, D.A., Aksay, I.A., 2006. *J. Phys. Chem. B* 110, 8535-8539.

Seo, J.H., Kang, J.W., Kim, D.H., Jo, S., Ryu, S.Y., Lee, H.W., Kim, C.S., 2013. *ECS Solid State Lett.* 2, M13-M16.

Shan, C., Yang, H., Han, D., Zhang, Q., Ivaska, A., Niu, L., 2010. *Biosens. Bioelectron.* 25, 1070-1074.

Shan, C., Yang, H., Song, J., Han, D., Ivaska, A., Niu, L., 2009. *Anal. Chem.* 81, 2378-2382.

Shang, N.G., Papakonstantinou, P., McMullan, M., Chu, M., Stamboulis, A., Potenza, A., Dhessi, S.S., Marchetto, H., 2008. *Adv. Funct. Mater.* 18, 3506-3514.

Shao, Y.Y., Wang, J., Wu, H., Liu, J., Aksay, I.A., Lin, Y.H., 2010. *Electroanal.* 22, 1027-1036.

Shapiro, R.L., Hatheway, C., Swerdlow, D.L., 1998. *Ann. Intern. Med.* 129, 221-228.

Shehada, N., Bronstrup, G., Funka, K., Christiansen, S., Leja, M., Haick, H., 2012. *Chem. Rev.* 112, 5949-5966.

Shin, H.J., Kim, K.K., Benayad, A., Yoon, S.M., Park, H.K., Jung, I.S., Jin, M.H., Jeong, H.K., Kim, J.M., Choi, J.Y., Lee, Y.H., 2009. *Adv. Funct. Mater.* 19, 1987-1992.

Sobel, J., Tucker, N., Sulka, A., McLaughlin, J., Maslanka, 2004. *S. Emerg. Infect. Dis.* 10, 1606-1611.

Stankovich, S., Dikin, D.A., Piner, R.D., Kohlhaas, K.A., Kleinhammes, A., Jia, Y., Wu, Y., Nguyen, S.T., Ruoff, R.S., 2007. *Carbon* 45, 1558-1565.

Stevens, G.B., Silver, D.A., Zgaga-Griesz, A., Bessler, W.G., Vashist, S.K., Patel, P., Achazi, K., Strotmeier, J., Worbs, S., Dorner, M.B., Dorner, B.G., Pauly, D., Rum-mel, A., Urban, G.A., Krueger, M., 2013. *Analyst* 138, 6154-6162.

Stine, R., Robinson, J.T., Sheehan P.E., Tamanaha, C.R., 2010. *Adv. Mater.* 22, 5297-5300.

Shapiro, R.L., Hatheway, C., Swerdlow, D.L., 1998. *Ann. Intern. Med.* 129, 221-228.

Sudibya, H.G., He, Q., Zhang, H., Chen, P., 2011. *ACS Nano* 5, 1990-1994.

Suk, J.W., Kitt, A., Magnuson, C.W., Hao, Y.F., Ahmed, S., An, J.H., Swan, A.K., Goldberg, B.B., Ruoff, R.S., 2011. *ACS Nano* 5, 6916-6924.

Tang, L.H., Wang, Y., Li, Y.M., Feng, H.B., Lu, J., Li, J.H., 2009. *Adv. Funct. Mater.* 19, 2782-2789.

- Vilian, A.T.E., Chen, S.M., 2014, RSC Adv. 4, 55867-55876.
- Wang, B., Cancilla, J.C., Torrecilla, J.S., Haick, H., Wang, B., 2014. Nano Lett. 14, 933-938.
- Wang, J., 2001. Electroanalysis 13, 983-988.
- Wen, Y.Q., Li, F.Y., Dong, X.C., Zhang, J., Xiong, Q.H., Chen, P., 2013. Adv. Healthcare Mater. 2013, 2, 271-274.
- Wong, J.K.F., Yip, S.P., Lee, T.M.H., 2012. Small, 8, 214-219.
- Wu, L., Wang, J.S., Feng, L.Y., Ren, J.S., Wei, W.L., Qu, X.G., 2012. Adv. Mater. 24, 2447-2452.
- Xia, Z.Y., Pezzini, S., Treossi, E., Giambastiani, G., Corticelli, F., Morandi, V., Zanelli, A., Bellani, V., Palermo, V., 2013. Adv. Funct. Mater. 23, 4684-6493.
- Ye, W.W., Guo, J.B., Chen, S., Yang, M. 2013. J. Mater. Chem. B 1, 6544-6550.
- Yin, Z., He, Q., Huang, X., Zhang, J., Wu, S., Chen, P., Lu, G., Chen, P., Zhang, Q., Yan, Q., Zhang, H., 2012. Nanoscale 4, 293-297.
- Yu, Q.K., Lian, J., Siriponglert, S., Li, H., Chen, Y.P., Pei, S.S., 2008. Appl. Phys. Lett. 93, 113103.
- Yuan, W., Zhou, Y., Li, Y., Li, C., Peng, H., Zhang, J., Liu, Z., Dai, L., Shi, G., 2013. Sci. Rep. 3, 2248.
- Zhan, B., Li, C., Yang, J., Jenkins, G., Huang, W., Dong, X., 2014. Small 10, 4042-4065.
- Zhang, T., Yang, Z., Liu, D., 2011. Nanoscale, 3, 4015-4021.
- Zhang, X.H., Zhang, Y., Liao, Q.L., Song, Y., Ma, S.W., 2013. Small 9, 4045-4050.
- Zhang, Y., Zhao, H., Wu, Z.J., Xue, Y., Zhang, X.F., He, Y.J., Li, X.J., Yuan, Z.B., 2013. Biosens. Bioelectron. 48, 180-187.
- Zeng, S., Chen, L., Wang, Y., Chen J., 2015. J. Phys. D: Appl. Phys. 48, 275402.
- Zhao, F., Slade, R.C.T., Varcoe, J.R., 2009. Chem. Soc. Rev. 38, 1926-1939.

Zhao, L., Jiang, D., Cai, Y., Ji, X., Xie, R., Yang, W., 2012. *Nanoscale* 4, 5071-5076.

Zhao, X.H., Kong, R.M., Zhang, X.B., Meng, H.M., Liu W.N., Tan, W., Shen, G.L., Yu, R.Q., 2011. *Anal. Chem.* 83, 5062-5066.

Zhong, X.B., Reynolds, R., Kidd, J.R., Kidd, K.K., Jenison, R., Marlar, R.A., Ward, D.C., 2003. *Proc. Natl. Acad. Sci. U S A* 100, 11559-11564.

Zhou, M., Zhai, Y., Dong, S., 2009. *Anal. Chem.* 81, 5603-5613.

Zhou, Y.X., E, Y.W., Ren, Z.Y., Fan, H.M., Xu, X.L., Zheng, X.L., Lei, D.Y., Li, W.L., Wang, L., Bai, J.T., 2015. *J. Mater. Chem. C* 3, 2548-2556.